

SORBONNE UNIVERSITÉ  
INSTITUT DE MINÉRALOGIE, DE PHYSIQUE DES MATÉRIAUX ET DE  
COSMOCHIMIE  
UMR 7590 - SORBONNE UNIVERSITÉ/CNRS/MNHN/IRD

---

# Anharmonic lattice theory and applications

---

Memoire de Habilitation à Diriger des Recherches

Lorenzo PAULATTO

Composition du jury:

*Rapporteurs*

Giuseppe CARLEO    Marie-Bernadette LEPETIT    Samy MERABIA

*Examineurs*

Riccardo MESSINA    Mathieu SALANNE    Rodolphe VUILLEUMIER

1er décembre 2022

*To Lisa, Eric and Paola.*

# Contents

<b>1</b>	<b>Introduction</b>	<b>1</b>
1.1	Brief history of (an)harmonic lattice dynamics . . . . .	1
1.2	Beyond the phonons with anharmonic perturbations . . . . .	3
1.3	State of the art and methodological development . . . . .	4
1.4	Past and future of applications . . . . .	6
1.4.1	Bidimensional materials . . . . .	7
1.4.2	Anharmonic phonon spectra . . . . .	7
1.5	Crystal structure simulation at finite temperature . . . . .	11
1.6	Perspectives on multi-carrier transport . . . . .	13
1.7	Structure of the manuscript . . . . .	13
<b>2</b>	<b>Intrinsic lifetime of phonons</b>	<b>15</b>
2.1	Harmonic Lattice Theory . . . . .	15
2.2	Ab initio phonon lifetime . . . . .	16
2.3	Anharmonic decay . . . . .	16
2.4	Application: Graphene and Graphite phonon lifetimes . . . . .	17
2.4.1	Computational details . . . . .	19
2.4.2	Graphene phonon broadening . . . . .	20
2.4.3	Graphite and bilayer graphene . . . . .	24
2.5	Conclusion of graphene and graphite . . . . .	27
2.6	Phonon spectral function . . . . .	27
2.7	Attenuation of Hyper-acoustic waves in GaAs . . . . .	29
<b>3</b>	<b>Thermal conductivity</b>	<b>31</b>
3.1	Treatment of finite samples . . . . .	31
3.1.1	Scattering mechanisms in finite crystals . . . . .	31
3.1.2	Thermal transport in the single-mode approximation . . . . .	32
3.1.3	Thermal transport in thin film crystals . . . . .	33
3.2	Applications . . . . .	33
3.2.1	Graphene and graphite . . . . .	33
3.2.2	Bulk Bi <sub>2</sub> Se <sub>3</sub> . . . . .	35
3.2.3	Bi <sub>2</sub> Se <sub>3</sub> thin films . . . . .	36
<b>4</b>	<b>Beyond Perturbation Theory</b>	<b>39</b>
4.1	TDEP implementation . . . . .	40
4.1.1	Phonon parameters . . . . .	40
4.1.2	Minimization and fitting . . . . .	41
4.1.3	Choice of sampling method . . . . .	42
4.2	Perspectives . . . . .	43
	<b>Appendices</b>	<b>43</b>
<b>A</b>	<b>Dynamical matrices and Force Constants</b>	<b>44</b>
A.1	Force constants . . . . .	44
A.2	Monochromatic perturbation (phonons) . . . . .	44
A.3	Fourier transform . . . . .	45
A.4	Grid of q-points and supercell . . . . .	46

A.5	Fourier interpolation, recentering . . . . .	46
A.6	Computing forces from force constants . . . . .	47
A.7	Translational invariance . . . . .	48
A.8	Acoustic sum rule . . . . .	48
<b>B</b>	<b>Basis of symmetric dynamical matrices</b>	<b>49</b>
B.1	symmetries of a crystal . . . . .	49
B.2	Irreducible wedge of the Brillouin Zone . . . . .	49
B.3	Applying symmetry to dynamical matrices . . . . .	50
B.4	Defining a matrix-matrix scalar product . . . . .	50
B.5	The space of symmetric dynamical matrices . . . . .	51
B.6	Extension to third order matrices . . . . .	51
<b>C</b>	<b>Implementation of <math>2n+1</math> theorem</b>	<b>53</b>
C.1	Third order calculation . . . . .	53
C.1.1	Kohn-Sham equations . . . . .	53
C.1.2	Linear response . . . . .	54
C.1.3	Third order . . . . .	54
C.1.4	Ionic contribution . . . . .	56
C.1.5	Gradient corrected functionals . . . . .	56
C.1.6	Derivatives of the external potential . . . . .	57
C.1.7	Second derivative . . . . .	57
C.1.8	Non-linear core correction . . . . .	58
C.1.9	Variation of wavefunctions . . . . .	58
C.2	Third-order response calculation . . . . .	59
C.2.1	Parallelism and computational cost . . . . .	60
<b>D</b>	<b>Description of computer codes</b>	<b>61</b>
D.1	Electronic structure code . . . . .	61
D.2	Utilities . . . . .	62
D.3	Main codes . . . . .	62
D.3.1	d3_r2q.x . . . . .	62
D.3.2	d3_qha.x . . . . .	63
D.3.3	d3_lw.x . . . . .	63
D.3.4	d3_tk.x . . . . .	64
D.3.5	d3_tdph.x . . . . .	64
D.4	Experimental codes: . . . . .	64

# Chapter 1

## Introduction

### 1.1 Brief history of (an)harmonic lattice dynamics

It is hard to argue that the field of *ab initio* study of solid-state physics starts with seminal works of Kohn, Sham and Hohenberg [1, 2], establishing Density Functional Theory (DFT) in the 1960s. They provided the tools to overcome the exponential barrier intrinsic in quantum systems of correlated particles. However, the possibility of simulating real materials remained limited until the 1980s, when the development of good “universal” approximations for the density functional [3, 4] and the revolution of computer technology allowed the simulation of real materials with no additional approximation or empirical parameters.

In a similar way, the theory of lattice vibration was already textbook matter in the 1950s, with a well established theoretical basis [5–7]. However, it wasn’t until the 1970s that the calculation of the vibrational “Dynamical matrix” from atomic interactions had been attempted [8, 9]. In the 1980s the synergy between theory and computer science allows the *ab initio* calculation of vibrations in solids via density functional perturbation theory (DFPT) [10, 11].

Similarly, the interpretation of thermal conductivity in terms of nanoscopic processes involving heat-carrying “particles” (which were not immediately identified as electrons or phonons) is more than one century old [12], however the interpretation in terms of harmonic vibrations (phonons) and limited by anharmonic interaction was the initial work of Peierls in the 1930s [13], who developed the linearized Boltzmann Transport Equation (BTE):

$$\left. \frac{\partial n_{\mathbf{q}j}}{\partial t} \right|_{\text{scatt}} = c_{\mathbf{q}j} \frac{\partial T}{\partial x} \left( \frac{\partial n_{\mathbf{q}j}}{\partial T} \right). \quad (1.1)$$

The time derivative of the phonon population  $n_{\mathbf{q}j}$  due to scattering, has to be equal to its temperature derivative, multiplied by the temperature gradient  $\partial T/\partial x$  (assumed to be in the direction  $x$ ) and the phonon group velocity  $c_{\mathbf{q}j}$ . The indexes  $\mathbf{q}$  and  $j$  refer to the phonon momentum and its band index respectively.

In order to have predictive power, this theory requires two important elements which were not yet available: the energy/velocity dispersion of the heat carriers, i.e.  $\mathbf{c}_{\mathbf{q}j} = \nabla_{\mathbf{q}} \omega_{\mathbf{q}j}$ , where  $\omega$  is the phonon frequency, and their scattering probability. As we have just seen, phonon dispersions have been routinely available via commercial or open-source softwares since the late 1980s, but the latter could only be computed for low-energy acoustic phonons using painfully complicated analytic models [14–16]. The first order perturbative equation for the scattering probability  $P_i^f$  is not complicated in itself:

$$P_i^f(\mathbf{q}j, \mathbf{q}'j', \mathbf{q}''j'') = \frac{2\pi}{\hbar} \left| \langle i | V^{(3)}(\mathbf{q}j, \mathbf{q}'j', \mathbf{q}''j'') | f \rangle \right|^2 \delta(E_i - E_f). \quad (1.2)$$

Where  $i$  and  $f$  are the initial and final state. What is “hard” to compute is the matrix element of the phonon-phonon interaction,  $V^{(3)}$ , which is proportional to the third derivative of the total energy with respect to three phonons  $\mathbf{q}j$ ,  $\mathbf{q}'j'$  and  $\mathbf{q}''j''$ . Apart from that, there is the condition that the total momentum and energy are conserved, which can be imposed in two different ways depending on the

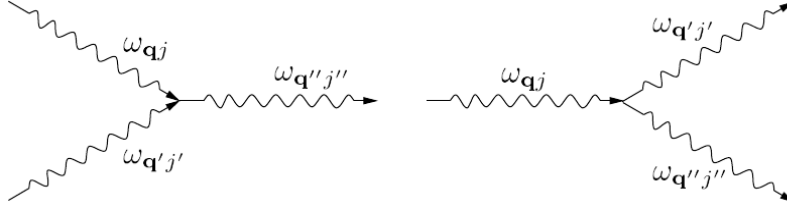


Figure 1.1: The two possible first order anharmonic process of intrinsic phonon scattering: on the left the coalescence of two phonons to one, on the right the scattering of one phonon into two.

process. For the “coalescence” of two phonons into one it is  $\mathbf{q} + \mathbf{q}' - \mathbf{q}'' = \mathbf{G}$ ,  $E_i = \hbar\omega_{\mathbf{q}_j} + \hbar\omega_{\mathbf{q}'_j'}$  and  $E_f = \hbar\omega_{\mathbf{q}''_j''}$ ; for the “scattering” of one phonon into two, it is  $\mathbf{q} - \mathbf{q}' - \mathbf{q}'' = \mathbf{G}$ ,  $E_i = \hbar\omega_{\mathbf{q}_j}$  and  $E_f = \hbar\omega_{\mathbf{q}'_j'} + \hbar\omega_{\mathbf{q}''_j''}$ . Because we are in periodic boundary condition, the wavevectors  $\mathbf{q}$  are actually crystal momentum, which is defined and conserved minus a reciprocal lattice vector  $\mathbf{G}$ .

The two process are shown, more intuitively, in a diagrammatic way in Figure 1.1. More details about this theory, including an expression for the intrinsic phonon lifetime, are in Section 2.3.

The way to compute the matrix element with DFPT was initially opened by Gonze *et al.* [17] who gave a functional formulation of the “ $2n+1$ ” theorem. It states that if the wavefunctions derivatives are known up to order  $n$ , it is possible to compute the derivative of the total energy up to order  $2n + 1$ , at a limited computational cost. This method has been initially implemented only for zone-centered interactions (i.e. when one of the three phonons colliding has vanishing wavevector) [18], this gives access to the calculation of the linewidth (and its inverse, the lifetime) of phonons with wavevector  $\Gamma = (0, 0, 0)$ . It is enough for studying the linewidth of Raman or Infrared spectra, but does not allow the simulation of collective phonon dynamics, such as thermal transport.

In the years 2000s, a few research groups have generalized these results, and were able to calculate the phonon-phonon scattering terms for generic wavevectors, but limited to simple systems, such as cubic insulators and semiconductors [19, 20]. Later on, other groups developed methods based on finite differences derivation which, thanks to the progress in computational power, could tackle more complex problems [21, 22], or hybrid approaches that used “ $2n+1$ ” in conjunction with supercells [23, 24]. I developed, in 2010-2013, a general “ $2n+1$ ” implementation, capable of dealing with insulators and metals, arbitrary geometries, and standard density functional approximations [25].

Even with the phonon-phonon matrix elements known exactly, solving the BTE remains a serious task. The most common approach was, and still is, the Single-Mode Approximation (SMA). Under this approximation, it is assumed that when a phonon undergoes a scattering event, its energy is distributed among all the modes according to the Bose-Einstein occupation. The expression is simple and intuitive:

$$\kappa_{\text{latt},\alpha\beta} = \frac{1}{V} \sum_{\mathbf{q}j} \hbar\omega_{\mathbf{q}j} \frac{\partial n_{\mathbf{q}j}}{\partial T} c_{\mathbf{q}j,\alpha} c_{\mathbf{q}j,\beta} \tau_{\mathbf{q}j} \quad (1.3)$$

Where the lattice thermal conductivity  $\kappa_{\text{latt}}$ , along Cartesian direction  $\alpha$ , under the effect of a temperature gradient along direction  $\beta$  is a sum of the phonon energies  $\hbar\omega_{\mathbf{q}j}$ , their lifetime  $\tau_{\mathbf{q}j}$  and the (analytical) derivative of the equilibrium Bose-Einstein population. Typically given per unit of volume, dividing by the unit cell volume  $V$ .

This approximation is sufficiently accurate for most materials, at room temperature and above, but breaks down at low temperature (10k-100K depending on the material) and, critically, for low-dimensional materials, such as graphene or mono-layer transition-metal dichalcogenides<sup>1</sup>. The reason is that scattering event can be divided in two categories: normal scattering where conservation of momentum is exact, and *umklapp* scattering, where momentum is conserved minus a reciprocal lattice vector, i.e. the so-called “crystal momentum” is conserved, but real momentum is not. Normal scattering does not impede thermal transport, it only causes phonon to “push each other” but always in the direction of the temperature gradient. At sufficiently high temperature it is Umklapp scattering that dominates, for simple geometrical reasons, causing all the phonons to interact in a collective way, consistent with SMA. But at very low

<sup>1</sup>XY<sub>2</sub>, with X=Mo or W and Y=S, Se or Te.

temperature, when only the phonons close to  $\Gamma$  are occupied, this does not hold. This is especially true for light materials, as the linear part of the acoustic phonons extend up to higher energies.

In the late 1990, the group of Sparavigna developed a method to solve the Boltzmann transport equation exactly, using an iterative algorithm, which, despite being expensive and sometimes difficult to converge, could be used to produce accurate results for the low-temperature conductivity of some simple materials [26–28].

I participated in the development of a novel approach, which recasts the BTE as the minimization of a quadratic form [29, 30]. This new method, is still one or two orders of magnitude more expensive than standard SMA, but it converges quickly and reliably, and can be easily extended to include extrinsic effects (isotope scattering, sample boundaries) which are often dominant at very low temperature. This innovative approach also allowed to predict different “regimes” of thermal transport with very different characteristics: (1) ballistic regime, when intrinsic scattering is negligible (2) hydrodynamic regimes, when phonon interact non-dissipatively (3) diffusive regime, when intrinsic dissipative scattering is dominant. This picture has since been further extended into a more general approach to heat-transport, based on heat-carrying quasi-particles (baptised “relaxon”) can have, in the hydrodynamic regime, a longer mean free path (MFP) than phonons, producing the so-called “second sound” phenomenon, i.e. heat carried as a wave [30, 31]. The most recent advancements include a generalized transport equation, which takes into account in an elegant formulation both diffusive transport, typical of crystals, and the incoherent “tunneling” transport mechanism of glasses [32].

## 1.2 Beyond the phonons with anharmonic perturbations

It may seem at this point, that the approach of harmonic lattice vibrations with anharmonic interactions is able to treat any solid material: hot or cold, crystal or glass, weakly or strongly anharmonic, and that the only limitation is the computing time required to simulate larger unit cells. However, there is an entire class of problems where all this picture breaks down. It is the case of temperature stabilized and meta-stable materials, and, in general, the proximity of second order phase transitions. These problem cannot be solved with the standard approach because harmonic phonons present instabilities, i.e. imaginary frequencies at the DFPT level: any small perturbation would push the system toward the phase transition. On the other hand, it is well known that some systems, especially higher symmetry phases, are stabilized by temperature: they are unstable at the DFPT level, because the curvature of the total “static” energy is negative around the high-symmetry configuration, but becomes positive (i.e. stable) if one takes into account the various vibrational contributions: zero point energy of phonon modes, their kinetic energy and entropy. We also know, from experiments, that these systems have well defined phonon bands, which may however present strong anharmonic features such as asymmetries and satellite peaks. I will show in Section 2.6 how these complex spectral function can be simulated.

In order to treat this class of problems, there has been in the years 2010s the emergence of several methods based on a philosophy that could be called “temperature-dependent phonons” (TDP) In Chapter 4.1 I’ll give a more complete review of these techniques [33–45] For this chapter, it suffice to say what they have in common. All these methods compute the force constants as a thermodynamic average, i.e. a sum of the thermodynamic ensemble. This sum is invariably replaced with a sampling, either stochastic or dynamic, of the momentum-position phase space. Each method uses its own unique way to extract temperature-dependent interatomic force constants up to a certain order. At quadratic order, one obtains “renormalized” phonons, which can be stable when zero-temperature DFPT phonons are not. Higher orders can also be estimated, to re-introduce anharmonic effects, typically at a higher computational cost. Linear order can be considered vanishing, if the sampling is done around the equilibrium lattice structure, or included, to estimate temperature-dependent forces and perform structural relaxation. Each method has its own strengths and weaknesses which make it more or less suitable to treat specific corner cases: quantum motion of nuclei, phase transitions, low-symmetry systems. The main advantage, is that from force constants one can recover the familiar quasi-particle picture, and can use all the standard tools based of Peierls BTE theory. On the other hand, they all share a main drawback: they give up the universality of “harmonic” phonons, i.e. these renormalized phonons cannot be considered a simple property of the material. Instead of being just progressively occupied with a temperature-dependent Bose-Einstein distribution, phonons become explicitly temperature-dependent.

I have contributed to the development of two of these methods: the Self-Consistent Stochastic Approxi-

mation [41] and quantum-correlators (QC) with PIMD [37], I have also supervised the implementation of a third method, a novel reciprocal-space implementation of the temperature-dependent effective potential method (TDEP) [44, 46] with an efficient sampling based on Langevin dynamics [47]. These three methods have complementary strengths: rigorous derivation of temperature-dependent internal forces and stress for SSCHA, resilience to quantum noise, even at sub-K temperatures, for QC and simple accounting of different symmetries, i.e. of competing phases, for TDEP. Thus they form a formidable combination that can tackle problems as disparate as hydrogen-rich metal substrates [48] or high-pressure and high-temperature Earth mantle conditions [49, 50].

I also have to acknowledge the recent developments of thermal transport simulation via equilibrium molecular dynamics (EMD) based on the Green-Kubo formula (GK), which completely drop the phonon quasiparticle. As little as 5 year ago, this approach seemed impossible to apply in periodic boundary conditions (PBC), because of the well-known problem of the position operator  $\mathbf{r}$  being ill-defined [51], as it appears in the definition of the energy flux  $\mathbf{J}_\varepsilon(t) = \int \dot{\varepsilon}(\mathbf{r}, t) \mathbf{r} d\mathbf{r}$ . Where  $t$  is time, and  $\dot{\varepsilon}$  the time derivative of the energy density. Defining the energy density is a problem in itself, but what is worst is that any naive definition of the current in PBC depends on the arbitrary choice of the origin of the coordinate system. Two complementary approaches have been published independently, one based on response function, which is suitable to describe all kind of currents: energy, charge or mass [52] in crystals, glasses and even liquids. The other is based on the virial theorem, assumes that mass current is zero to derive a gauge-invariant definition of the flux [53]. The former is more powerful, the latter simpler but equally good for solids. They both employ large supercells to take into account heat transport from carriers which have long mean-free paths, such as the relaxons in 2D materials or phonons at low temperature, they are thus more suitable for application at high temperature, or relatively disordered systems.

There are two common problems to all these advanced methods, based on TDP or EMD-GK: the long correlation time of NVE molecular dynamics, and the failure to reach ergodicity, i.e. to explore all the phase space, which tends to emerge when approaching a phase transition. The first problem arises because subsequent steps of a trajectory are very similar to each other, and thus do not provide much more information, the root cause is that a fine integration of the time axis is required to properly take into account high frequency vibrations (rigid bonds). It is customary to take a time step shorter than the inverse frequency of the highest phonon. The failed ergodicity problem occurs when a system approaches the transition toward a lower-symmetry phase. Its potential energy landscape will form several minima, separated by barriers which are initially lower than the thermal excitation  $k_B T$ . MD trajectories will tend to stick to a minima as crossing the barrier becomes an increasingly rare event, soon out of the reach of any simulation [54]. The result, if symmetry is imposed (an almost universal feature of TDP methods), can be to impede the phase transition by forcing the phonon dynamical matrix to have more symmetry than the systems. It is less evident, but even methods based on stochastic phase-space sampling suffer the same problem, as a very fine sampling is required to find the transition pathway. Even for simple systems, there is an effects on the reliability of simulations, for example, at least three different transition mechanisms have been proposed for the SnSe transition from high-symmetry  $Cmcm$  to low-symmetry  $Pnma$  by groups using different TDP methods [55–57].

### 1.3 State of the art and methodological development

In light of what has been said in the previous section, I will argue that combining TDP methods with the most advanced MD techniques, for example Metadynamics [54] and Langevin dynamics [37] is a necessary step to overcome the limitations of current methods, I am already supervising two students that work in this direction, with two different strategies [46, 50].

The combination of the TDEP method with Langevin dynamics (LD) is the first approach. LD is a smart way to run temperature-controlled dynamics, (NVT from the conserved quantities: Number of particles, Volume, Temperature), where the role of the thermostat is fulfilled by stochastic forces that are applied with a distribution compatible with the required temperature. In parallel, a damping force is applied, which exponentially erases the trajectory history, guaranteeing a very short auto-correlation time between subsequent steps. The actual values can vary, and depend on the parameter choices, but can typically be between 2 and 5 MD steps. Another way to see LD is as a Markov chain process [58], where instead of rejecting or accepting new steps, depending on their energy, like in the Metropolis algorithm, we can reach 100% acceptance by exploiting the knowledge of the gradient of the free-energy landscape, i.e. the

*ab initio* forces acting on the atoms. It is useful to note that even in the normal Metropolis algorithm, where there is no history, there is an auto-correlation time, as the acceptance test probability depends on the energy of the last accepted step.

The main disadvantage of LD is that trajectories can be unphysical, especially if the damping factor is too high and that it does not have a simple conserved quantity to be monitored during the run. But these problems can be overcome with a carefully crafted “integrator”, i.e. an approximation of the Liouvillian operator in the Fokker-Plank equation [59] that determines the motion of the atoms. For our applications, we can simply observe that we are more interested in the sampling than in the actual trajectory, we can accept these trade-offs in exchange for its efficiency and ergodicity, which have widely been proven.

In order to take into account the quantum motion of nuclei, we can use the well-established Path-Integral Molecular Dynamics (PIMD) technique. In this method, many copies of the system under consideration are simulated simultaneously, in addition to the physical internal forces, one introduces fictitious elastic strings that connect the different replicas. The details of the coupling and the selection of the elastic constants depends on the exact flavour of PIMD, of which many exist [47, 60, 61]. In the PIMD jargon, the ensemble of replicas is referred as a “ring”, “polymer” or even “necklace”, while the individual replica is called a “bead”.

Furthermore, we are interested in coupling LD with PIMD, this technique is also established as the Path Integral Langevin Equation (PILE) [47, 62]. Where we want to innovate, is to combine PILE with TDEP to solve its two main drawbacks: the high computational cost required for a sufficient sampling of the phase space using long-correlation time standard NVE MD (conserved quantities: Number of particles, Volume of the unit cell, total Energy) and the inconsistency between using classical dynamic of the nuclei to fit a quasi-particle based model, adding quantum nuclei effects, such as zero-point vibration and Bose-Einstein occupation, only *a posteriori*. In the worst case, where the nuclei dynamics is in fact classical, the use of PIMD technique can accelerate the sampling, by exploring more configurations simultaneously.

As a second step along this direction, we will try to interpret the vibrational properties of disordered non-stoichiometric crystal and minerals, which is a problem of great interest for the geological sciences, but could also have application to the vast field of metal alloys and to the study of phase-change materials, where the same crystal site can be occupied by different species, sometimes leading to amorphous structures [63, 64]. As a benchmark for our approach we can take, for example, disordered SiGe which has already been studied with different methods [23]. The common difficulty of these systems is that, despite being disordered, they are more similar to crystals than to glasses, as they have a well defined lattice geometry and only the occupancy of the lattice sites can vary, more often by two similar chemical species.

Simulating these systems with a supercell in periodic boundary conditions meets two limitations: on one hand, long-range order is introduced which could favour long-range vibrations. On the other hand, taking into account all possible permutations and their disorder entropy is a tedious and error-prone task. A Monte Carlo approach can be used, either in a grand-canonical or, more easily, by exchanging compatible ions keeping the stoichiometric constant. Combining this kind of sampling with a *ab initio* dynamics is a non-trivial and, to the best of our knowledge, novel approach. TDEP can then be applied on the generalized trajectories to extract “average” phonons, which are similar, in spirit to what could be obtained from a virtual crystal approximation, but without the drastic assumption of this simple model [65]. The scattering probability of phonon with disorder can be put back in the picture using either effective models, or establish an external collaboration to employ the more advanced non-equilibrium Green function method (NEGF) method [66].

A development which I am pursuing on a different direction is the extension of the QC method to obtain an expression for 3rd and possibly 4th order force constants. This would allow us to construct a coherent model that predicts not only renormalized phonon frequencies but also their lifetimes, and thus the thermal transport properties. This would allow a perturbative, but exact, prediction of lattice thermal conductivity even in extreme cases such as hydrogen-rich materials down to cryogenic temperatures, with important applications to the quickly developing field of high-pressure superconductivity [67, 68]. The main advantage of the QC method with respect to TDEP is a more rigorous formulation. As I will discuss in Section 4.1, TDEP promises to return the best harmonic phonons for a given system and temperature, but the definition of “best” is debatable. To understand this issue we can compare TDEP and SSCHA: TDEP minimizes the difference between the “harmonic” forces, which are obtained from two-body force

constants and the the *ab initio* forces, sampled by the MD. If the method is extended to third order, the residual force is again fitted with 3-body force constants, which produce cubic terms. Conversely, the SSCHA method uses a variational approach, the best force constants are those that minimize the free energy. It can be shown that under some conditions, the harmonic level of TDEP and SSCHA are equivalent [69]. This however depends on the sampling used, and is not evident when they are extended to include third or fourth order, and will deserve further investigation.

The QC method attacks the problem from a completely different angle. It is an established result in classical statistical mechanics that the instantaneous force fluctuation (i.e. the thermal average of the instantaneous force-force correlation) and the thermodynamic average of the force constants are equal, this approach is exact beyond perturbation theory [70]. In equation terms:

$$\langle F_i F_j \rangle = k_B T \left\langle \frac{\partial^2 \mathcal{E}}{\partial x_i \partial x_j} \right\rangle \quad (1.4)$$

, where on the left-hand side  $F_i$  ( $F_j$ ) is the force acting on atom with index  $i$  ( $j$ ) in the simulation cell, and  $\langle \dots \rangle$  indicates the average over the statistical ensemble. on the right-hand side  $T$  is temperature and  $k_B$  is the Boltzmann constant and the force constant associated with atoms  $i$  and  $j$ , i.e. the partial derivative of the total energy  $\mathcal{E}$  with respect to the displacements  $x_i$  and  $x_j$ . One can derive, with a linearization linearization, a similar expression for force constant from the autocorrelation function of the displacements  $\langle x_i x_j \rangle = k_B T \left( \left\langle \frac{\partial^2 \mathcal{E}}{\partial x_i \partial x_j} \right\rangle \right)^{-1}$ . A third expression, that can be derived for the velocities autocorrelator  $\langle \dot{x}_i \dot{x}_j \rangle$ , corresponds to the well known principal mode analysis method [71]. Further derivation produces a generalized eigenvalue equation that describes the vibrational spectrum even for out-of-equilibrium systems. The quantum case is more cumbersome to derive, but finally reduces to similar expressions, where the averages have to be performed also over the PIMD beads. Furthermore, in the quantum case, the linearization involved in the position autocorrelation expression is not an approximation, as it can be shown to return *exactly* not the phonon frequency, but the oscillator first excitation energy. The two are only equal in the perfectly harmonic case, where the eigenvalues are equally spaced [37].

The strengths of this approach, combining QC with PILE are various. First, it has a rigorous derivation, where no arbitrary choice is made to favour one harmonic renormalization. Second, because of the stochastic component of the Langevin thermostat, it is resilient to noisy forces, which means that it can be combined with non-deterministic Quantum Monte Carlo (QMC) simulations of the electronic degrees of freedom, and in general may suffer less from numerical noise. Last, but not least, the entire chain of operation takes into account the full quantum properties of nuclei motion. These three properties are extremely important when targeting the sub-chemical accuracy, required to model hydrogen-rich systems.

There are however, many open questions. We know that, in the classical case, the force-force expression can be extended to third order, i.e. that also this equality holds:  $\langle F_i F_j F_k \rangle = k_B T \left\langle \frac{\partial^3 \mathcal{E}}{\partial x_i \partial x_j \partial x_k} \right\rangle$ . However, we do not know if this is true for the quantum formulation, and we do not have an expression for the fourth order in neither the classical nor the quantum case. Exploring this points will for sure be a task of the next few years.

Summarizing, these are the main research projects: improve the TDEP by using LD sampling, extend it to tackle disordered “entropic” crystals, and establish in a more formal way its link with the SSCHA method, which would reap the benefit of its variational formulation. Extend the correlators approach to compute higher order of force constants, especially when quantum dynamics are used.

## 1.4 Past and future of applications

Having at disposal a complete theory and a set of numerical tools has opened the path to numerous applications in disparate fields of condensed matter physics, for example: (1) pure research studies of the peculiar properties of ideal low-dimensionality materials, (2) strongly anharmonic thermoelectric materials, (3) simulation of hyper-acoustic sound waves, (4) simulation of vibrational spectra and thermal transport of natural minerals at extreme temperature and pressure conditions of geological interest, and (5) simulation of vibrational spectra of synthetic meta-stable materials to guide structure identification.

### 1.4.1 Bidimensional materials

The theoretical study of bidimensional materials can give answers that are difficult to obtain from experiments: real graphene samples are always either deposited on some substrate, and thus affected by its interaction, or suspended, and affected by some amount of strain. When they are probed, even a modest accumulation of heat can cause local straining and buckling. It is not a surprise that *ab initio* theory has played a fundamental role in the interpretation of data. The first application of my work on the phonon linewidth and lattice thermal conductivity of graphene came a few years after the first measurements of thermal transport in suspended graphene [72, 73], and confirmed that the bidimensional material could have a record-high conductivity, even higher than that of bulk graphite. It also showed that the SMA was probably not a good approximation for this system, as the absolute value was quite underestimated, we thought initially because of the very long lifetime of the quadratic acoustic band [25]. Research beyond this approximation was already in progress, with the development of a new method to solving the BTE with a variational formulation: a matrix of all the possible phonon-phonon interaction probabilities is constructed from first principles, then the variation of the phonon population is linearized around the equilibrium Bose-Einstein distribution and a minimization finds the perturbation that makes the BTE stationary. In intuitive terms: the heat-carrying steady state is reached when the incoming and outgoing scattering of each phonon state are at equilibrium. A numerical solution was still an important challenge, which required expertise in the treatment of extrinsic effects (scattering with isotopic disorder, borders) and numerical optimization.

Three applications followed shortly: first, as a showcase, we could reproduce the thermal conductivity of simple and isotope-pure diamond (100%  $^{12}\text{C}$ ) with great accuracy, down to a few K and taking into account the sample size [29]. The second and third application [30, 74] went back to bidimensional materials, and showed the presence of collective heat-carrying modes, exhibiting mean free paths (MFP) potentially unlinked from those of individual phonons. Furthermore, we showed that an universal property of bidimensional materials is the presence, in a wide temperature range, of an “hydrodynamic” regime, where phonon interacts non-dissipatively, and can carry heat as a wave i.e. the famous “second sound” wave that had previously only been observed in liquid-helium cooled Bi or NaF<sup>2</sup>. On the other hand, in most 3D materials, it is extrinsic scattering, linked to impurities and sample geometry that determines the maximum of low-temperature thermal transport, as schematized in Figure 1.2. Second sound was eventually measured in graphite several years later at 120 K and then 200 K [75, 76], but only over micrometer lengths. Its presence in graphene has still to be confirmed by experiment.

An important advantage of *ab initio* techniques is that they let one gain some insight about the microscopic heat-transport mechanism, a knowledge that one could use to tune the transport properties. Tuning the phonon dispersion is not necessarily a trivial task, but we did propose some idea based on nanostructuring to reduce thermal conductivity of Bismuth, in a later collaboration [77].

The parts of this research where my contribution has been more extensive are reported in Sections 2.3 and 2.4, with technical details of the theory in Appendix C.

### 1.4.2 Anharmonic phonon spectra

It is a recurring need of experimental groups to interpret the vibrational spectra coming from Infrared (IR), Raman, Inelastic X-Ray scattering (IXS) or Neutron scattering (INS) measurements. IR and Raman only probe zone-center modes, i.e. modes of vanishing crystal momentum, while IXS and INS can access modes of arbitrary  $q$ -vector. Not all peaks are IR and Raman active, in simple crystals they can be identified by symmetry, but in more complex materials two active modes can have very different cross sections, resulting in not all of them being visible in the measurements. These cross sections can be computed *ab initio* in the static long wavelength limit from response functions: the response to one zone-center phonon and one electric field is called the “effective charge” of an atom, and it gives access to the IR cross-section; the response to one phonon and two electric fields give access to the Raman tensor [80]. A more complex case, is the simulation of resonant Raman, when the probing laser activates electronic and vibrational excitations, which usually requires an ad-hoc treatment [81]. For IXS and INS scattering, the cross section depends on the projection of the probing wavevector on the phonon polarization, weighted with element-specific form-factors, which depend on the nuclei and deep core electronic structure.

---

<sup>2</sup>the peculiarity of these materials is that their chemical elements have a single stable isotope, and that they can be obtained in large single crystals, allowing the intrinsic scattering effects to be dominant down to very low temperature

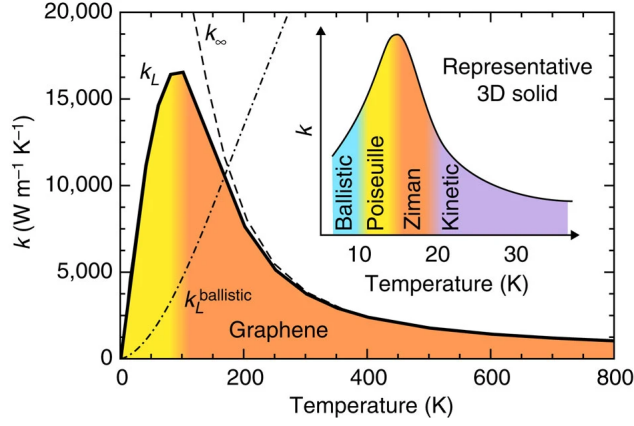


Figure 1.2: Thermal conductivity of a graphene ribbon of width  $L=100 \mu\text{m}$  ( $\kappa_L$ , solid line) together with its ballistic limit (dashed), and of an infinite graphene sheet ( $\kappa_\infty$ , dashed line). Inset: thermal conductivity regimes in a standard 3D solid, where peak conductivity is obtained at cryogenic temperatures and the hydrodynamic conditions, if present, are confined around those temperatures. Regimes are as follow. Ballistic: only scattering with interfaces has a significant role. Poiseuille: the dominant scattering effects are extrinsic (defects, sample borders). Ziman (or Hydrodynamic): intrinsic (phonon-phonon) non-dissipative effects are dominant. Kinetic (or Diffusive): dissipative intrinsic scattering dominates. From Reference 30.

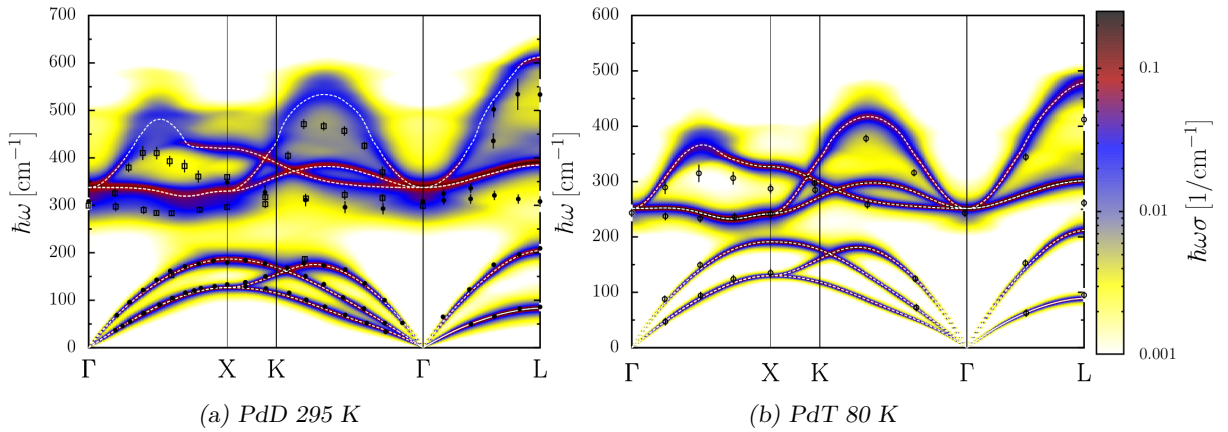


Figure 1.3: Spectral weight of (a) PdD (Palladium Deuteride) at 295 K compared with experimental INS measurements for  $\text{PdD}_{0.63}$  [78] and (b) PdT (Palladium-Tritium) at 80 K as a function of momentum and of energy compared with  $\text{PdT}_{0.7}$  [79]. Figure from Reference 48.

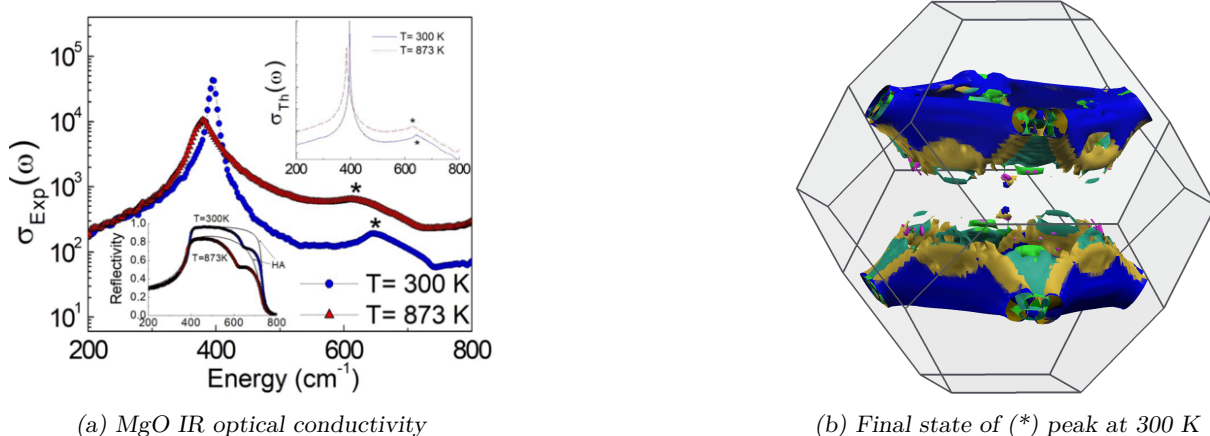


Figure 1.4: (a) Experimental (symbols) and theoretical (lines in the upper inset) optical conductivity of MgO at 300 and 873 K. The bottom inset shows the corresponding measured infrared reflectivity spectra (symbols) together with the theoretical reflectivity foreseen in the harmonic approximation (HA) (black lines). Stars (\*) indicate the position of the secondary peak. (b) Final state decomposition of (\*) peak from Figure a, i.e. the phonons contributing to double-excitation event of the peak, isovalue plot at 10% of the maximum. Colors correspond to different bands (yellow and green are acoustic, blue is optical). Figures from Reference 49.

It is also possible that the experimental probe excites more than one phonon at the same time. For example the laser light used in IR and Raman can excite two phonons with opposing  $\mathbf{q}$ -vector. This gives rise to second-order peaks, which can extend up to twice the Debye frequency, or under the lowest harmonic phonon, and cannot be interpreted from symmetry alone. The cross section of the probe-matter interaction, for an arbitrary momentum and frequency is remarkably independent on the kind of probe; if we ignore the specific form factors, it is proportional to the “spectral weight”  $\sigma(\mathbf{q}j, \Omega)$  [79]:

$$\sigma(\mathbf{q}j, \Omega) = \frac{2\omega(\mathbf{q}j)\Gamma(\mathbf{q}j, \Omega)}{(\Omega^2\omega^2(\mathbf{q}j) - 2\omega(\mathbf{q}j)\Delta(\mathbf{q}j, \Omega))^2 + 4\omega^2(\mathbf{q}j)\Gamma^2(\mathbf{q}j, \Omega)}. \quad (1.5)$$

The spectral weight  $\sigma(\mathbf{q}j, \Omega)$  is developed perturbatively on top of phonon  $\mathbf{q}j$  of unperturbed energy  $\omega(\mathbf{q}j)$ ;  $\Omega$  is the energy of the probe,  $\mathbf{q}$  the momentum of the probe and, because of conservation, of the phonon;  $j$  is the band index that determines its polarization. The functions  $\Delta(\mathbf{q}j, \Omega)$  and  $\Gamma(\mathbf{q}j, \Omega)$  are respectively the real and imaginary parts of its frequency-dependent self-energy. The method I have developed for computing phonon lifetimes gives access, with a trivial extension, to functions  $\Delta$  and  $\Gamma$ , and thus to the simulation of the full anharmonic spectral weight. At the perturbative level the spectra weight retains the characteristics polarization and symmetry of its associated phonon, which makes it easy to combine it with the standard form factor.

Our first application of this method was to simulate the vibrational spectra of Palladium Hydride (PdH), a material considered promising for stocking or filtering hydrogen, and particularly difficult to study because the nuclei of hydrogen move in a shallow potential, where both anharmonicity and quantum effects are important. We combined the calculation of stochastic self-consistent phonons (SSCHA) with the spectral-weight from the perturbative self energy, to reproduce existing INS measurement with great accuracy, including isotope dependency, i.e. the effect of replacing hydrogen with deuterium or tritium, as see in figure 1.3. More details on this application are reported in Section 2.6.

Later on, we realized how simulating the spectral weight could explain secondary peaks in IR spectroscopy measurements of minerals. The first application was MgO, an “end mineral” of Earth mantle, i.e. one of the simple minerals that participate in the complex blend of the mantle. Using synchrotron radiation, it is possible to perform IR spectroscopic measures with very fine energy resolution, which in term showed the presence of a secondary peak whose temperature evolution was different from that of the main peak (MgO has a single IR-active mode). Modelling the volume evolution with a quasi-harmonic model, but taking into account the full anharmonic contribution to the spectra we could not only reproduce the experimental data, but also show precisely the underlying physical mechanism involved in this peak. As we have seen, IR radiation can couple to a doublet of phonons of opposite angular momentum; at the

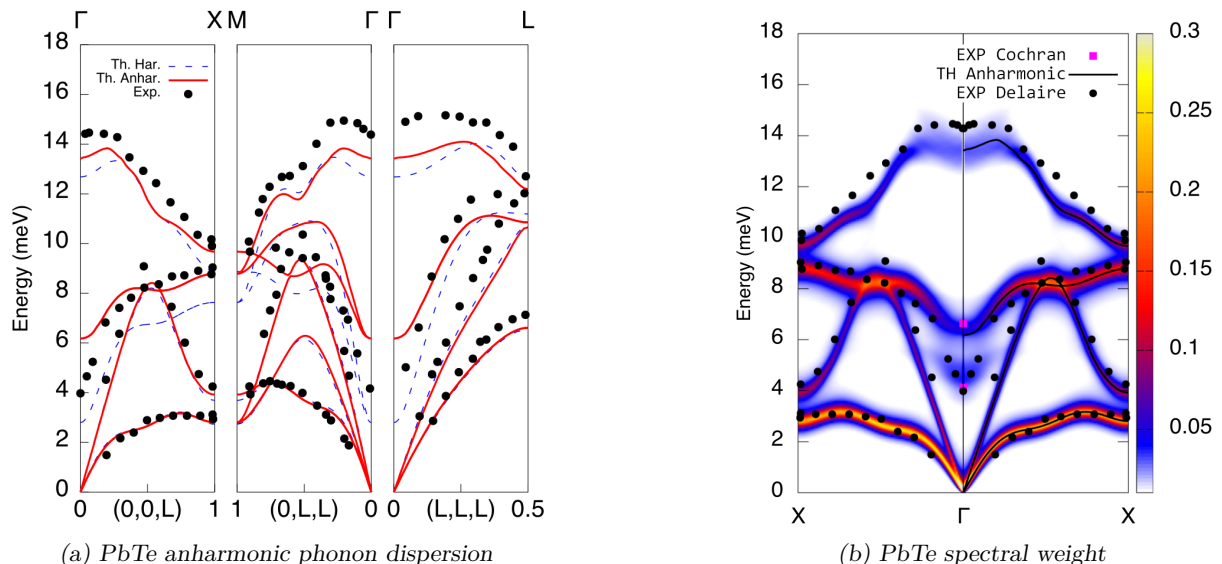


Figure 1.5: Study of the vibrational spectra of PbTe at 300 K. (a) Comparison of harmonic and anharmonic phonon dispersion with INS data. (b) Spectral weight. One can see how the peak measured at  $\Gamma$  around 4 meV is not a single phonon, but a secondary peak caused by two-phonon processes. Experiments are from Cochran *et al.* [84](#) (black dots) and Delaire *et al.* [83](#) (pink squares). Figures from Reference [85](#).

energy of the secondary peak a very large volume of the Brillouin zone is involved in this mechanism, giving rise to a maximum in the spectrum. In Figure [1.4](#) I report the experimental and theoretical spectra, and a 3D plot of the Brillouin zone containing the volume contributing to the excitation of the secondary peak. We used similar techniques in two papers [\[49, 82\]](#) which allowed to establish the accuracy of theory up to 1400 K and down to 21 GPa. The extension to the entire range pressure and temperature range of the Earth mantle, and application to study of planetary mantle dynamics is currently the subject of a PhD study [\[50\]](#).

Another example of secondary peak that we could interpret with our *ab initio* tools is the softening of the first optical mode in lead telluride. PbTe has a very low thermal conductivity which makes it a good candidate material for thermoelectric development. Its cubic phase is stable at low temperature, but it is an “incipient ferroelectric” material, i.e. a material characterized by increasing permittivity on cooling due to the softening of the lowest frequency polar optical phonon. INS experiments [\[83\]](#) reported that it exhibits a phonon satellite peak close to zone center, a clear fingerprint of strong anharmonicity. We studied the evolution of the phonon bands using the SSCHA methods, and the formation of the satellite peak via spectral weight simulations. In Figure [1.5](#) we show the comparison of calculation and experiments. We could show that the formation of the satellite peak correspond to anharmonic softening of the optical band, in conjunction with strong two-phonon scattering, which, as in MgO, can take place toward a wide volume of the Brillouin zone.

On a slightly different direction, I supervised a combined effort of experiment and theory to study the attenuation  $\alpha = 1/2|\mathbf{c}_{\mathbf{q}j}|/\tau_{\mathbf{q}j}$ , i.e. the inverse of the two mean free paths, in semiconductors (Silicon and GaAs) in an intermediate frequency between 100 MHz and 1 THz. This regime is particularly interesting because the short wavelength of these waves is suitable to perform acoustic imaging, while their low energy makes it non-destructive. The applications range from 3D imaging of photolithographic semiconductor chips, to the control of quantum dots via optomechanic coupling. In this regime the vibrations are half-way between the phonons (for which  $\omega_{\mathbf{q}j}\tau_{\mathbf{q}j} \gg 1$ ) and acoustic waves ( $\omega_{\mathbf{q}j}\tau_{\mathbf{q}j} \ll 1$ ) which makes them particularly difficult to treat. We manage however, thanks to Fourier interpolation techniques, to integrate the phonon lifetime with great accuracy, and obtain solid results down to the 10 GHz range, with very good agreement with experiments. I will give more details about this study in Section [2.7](#).

More recently, we have used the spectral function analysis to interpret high energy peaks in the vibrational spectra of minerals containing OH groups (lizardite, brucite, talc). This spectra can be difficult to interpret because the high-energy modes of the OH bond (around  $3700 \text{ cm}^{-1}$ ) can blend with what in

mineralogy is known as “overtones”, i.e. the collective excitation of two phonons as we have seen in MgO and PbTe. A simpler approach tries to determine the position of secondary peaks, only considers the conservation of energy and momentum, without including the anharmonic matrix element; but the selection rules, embedded in the matrix elements, are difficult to infer from symmetry alone, especially for structures that are only close to being symmetric, resulting in a large number of predicted peaks not being observed in experiments. In the static limit, we can combine the spectral weight with the Raman cross section, also from *ab initio*, and discern the relative intensity of the peaks [86].

## 1.5 Crystal structure simulation at finite temperature

The thermal excitation  $k_B T$ , even for a temperature as high as 1000 K, is only roughly to  $10^{-3}$  Rydberg atomic units of energy. This is a tiny fraction of the typical energy involved in electronic excitation of solids. In any good insulator, it cannot induce any excitation across the electronic band gap; in a bad insulator, or even a metal, the change of the electronic population, due to the change in Fermi-Dirac distribution, can have determine optical properties, but has only the tiniest effect on the electronic band structure. It is in fact customary to use, in order to help numerical convergence of DFT calculations, a fictive electronic temperature of the order of 10'000 K or more, without compromising the accuracy of the simulation [87]. On one hand, the electronic structure is too rigid to be influences by temperature directly, but on the other hand, thermal excitation induces vibration of the ions, which in term has an effect on the crystal geometry and the electronic structure. In order to include the temperature *ab initio*, a model to take into account the lattice vibrations is necessary.

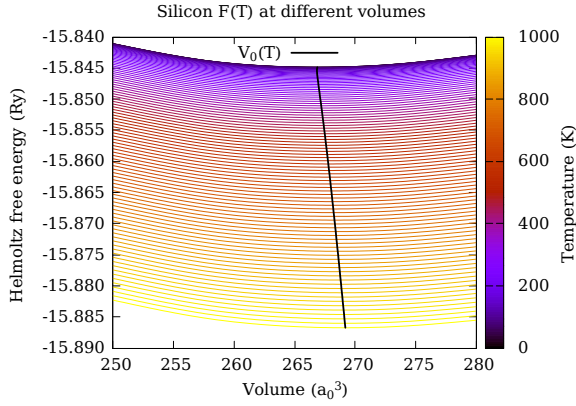
An effect which cannot be taken into account by the pure harmonic theory is thermal expansion. In this approximation, atoms vibrate in a symmetric parabolic potential: increasing the temperature has only the effect of increasing the amplitude of their motion, not their average distance. A first approach to treat thermal expansion is the Quasi-Harmonic Approximation (QHA) [88, 89]. In this theory, one includes temperature dependence introducing the Helmholtz free energy  $F$  given by

$$F(T, \mathbf{u}) = E(\mathbf{u}) + k_B T \sum_j \ln \left( 2 \sinh \left( \frac{\hbar \omega_j(\mathbf{u})}{2k_B T} \right) \right) + pV, \quad (1.6)$$

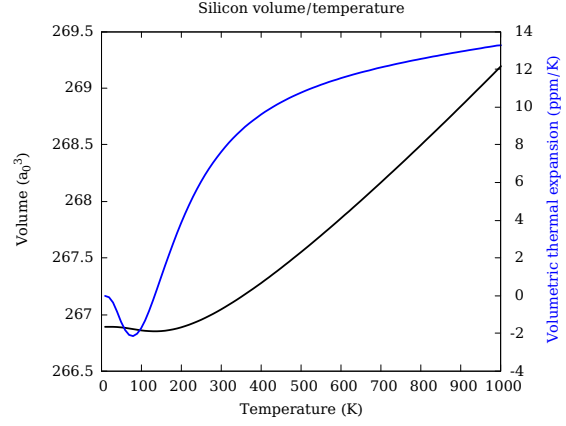
where  $E(\mathbf{u})$  is the system “total” static energy,  $\omega_j(\mathbf{u})$  are the phonon frequencies where the index  $j$  is composite of q-point and band index. They both depend on some structural parameters  $\mathbf{u}$ . By finding the value of  $\mathbf{u}$  that minimizes  $F$  at a given temperature  $T$ , one can obtain the  $T$ -dependence of  $\mathbf{u}$ . The hydrostatic  $pV$  term is the product of the external pressure  $p$  with the unit-cell volume  $V$ . The QHA approximation has been successful in predicting thermal expansion properties of simple bulk crystals and even surfaces. As an example, we can see in Figure 1.6 how it can reproduce the negative thermal expansion of Silicon at low temperature.

I have applied the QHA method in combination with the simulation of anharmonic spectra to interpret the Raman spectra of synthesized monochalcogenides, GeTe, GeSe and SnSe, under high pressure or high temperature conditions. These materials exhibit competing phases: starting from the high-symmetry *fcc* Rocksalt Cubic phase, the lattice can develop a slight distortion in the internal coordinates, then in its angles becoming rhombohedral. Lower symmetry orthorhombic *Cnmm* and *Pnma* phases are also possible, and could be favoured at higher pressure. The relative formation entropy of these phases is very close, more than we can trust DFT, but we can compute the vibrational modes and their Raman activity, and compare their evolution on pressure and temperature with experimental data. Having access to the anharmonic properties allows us to simulate also the peaks width and their temperature evolution. We have keep in mind that the intrinsic peak width is only a lower bound for its experimental value, as disorder scattering and experimental resolution can also contribute to its widening [90, 91]. I show in Figure 1.7 a most significant result, in which the progressive merging of the two Raman-active peaks in GeTe was shown to be an effect of their widening and deviation from the standard Lorentzian shape due to anharmonic interaction.

In another work we could combine the capability of the anharmonic calculation to take into account substitutional disorder, to determine the crystal structure of  $\text{Ge}_2\text{Sb}_2\text{Te}_5$  (GST). This material has an hexagonal stacking, of which two variants had been hypothesized, depending on the position of Ge and Sb atoms, but it not possible to discern between the two with direct crystallographic measures. A third hypothesis, is that the two species can occupy either site, causing the structure to become disordered.



(a) Helmholtz free energy  $F(T, V)$



(b) Volume  $V(T)$ , thermal expansion  $dV(T)/dT$

Figure 1.6: An example of ab initio QHA applied to Silicon: (a) Helmholtz free energy as a function of lattice parameter for several temperature values and, in black, the line joining the minimum of each curve. (b) In black, the relaxed volume as a function of temperature; in blue, the volumetric thermal expansion in parts per million.

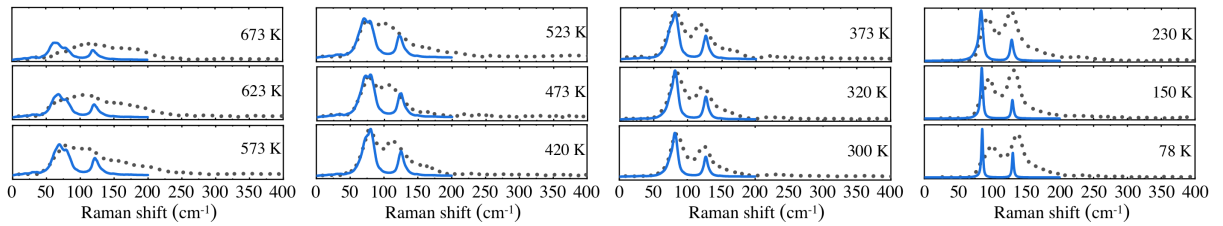


Figure 1.7: Temperature dependence of experimental GeTe Raman spectra (dotted line, measured count rate) and a comparison with calculation including anharmonicity (solid line, normalized to experimental count rate). Adapted from Reference 90.

By *ab initio*] anharmonic lattice simulations of GST with those of GeTe and Sb<sub>2</sub>Te<sub>3</sub>, we could argue that its very low thermal conductivity is only consistent with the disordered lattice hypothesis [63].

QHA analysis becomes prohibitive when the crystal structure has more degrees of freedom, a multi-dimensional space has to be explored with a plethora of DFPT calculation, and a global minimum found. What is routinely done, even by us in many cases, is to only take into account the vibrational effect in the volume optimization, while all the other degrees of freedom are relaxed statically. Furthermore, if the DFPT phonons become unstable, it may not be possible to compute the Helmholtz energy in such a simple way. We have seen in Section 1.3 as some TDP methods can provide an estimate of temperature-dependent forces and stress. However, the computational cost is high, as long sampling phases are required for each evaluation of the forces. This is exacerbated by the “noisy” nature of these methods, which does not cope well with standard minimization algorithms used to optimize the crystal structure.

Variable-cell molecular dynamics techniques, that allow to identify an average structure at finite temperature has been available since the 1990s [92], however it is seldom used because of it is finicky in practice. Extending this idea to fictitious dynamics (LD, metadynamics) may overcome these difficulties and promote it as a standard tool, bypassing the phonon calculation entirely. An alternative approach would be to combine advanced structural search algorithms [93] with TDP to take into account the vibrational contribution but increasing the efficiency of the search. These are promising lines of investigation in the medium to long term, possibly in combination with machine learning technique to accelerate the *ab initio* calculation, or the structural optimization by using methods, such as genetic algorithms, that do not rely exclusively on the internal forces.

## 1.6 Perspectives on multi-carrier transport

An outstanding challenge for the next decades is going to be the development of materials for energy conversion and harvesting, in particular thermoelectrics and photoelectrics. My interest is mostly on the former, where the use of *ab initio* methods can give a formidable contribution. Especially in combination with modern “high throughput” simulation methods [94], we can at minimal cost detect good candidate materials, based on a choice of optimization parameters. However, to this day, it is not possible to discriminate by thermoelectric efficiency, i.e. the often used “figure of merit”  $ZT = S^2\rho - 1\kappa^{-1}T$ . The physical quantities on which it depends are Seebeck coefficient ( $S$ ), electrical resistivity ( $\rho$ ), and thermal conductivity ( $\kappa$ ), they can all be computed *ab initio* but by different groups, using specific approximations and techniques, often under the hypothesis that the others factors are not important.

DFPT allows today to compute electron-phonon [95] and phonon-phonon scattering rates from first principles; and to describe phonon transport via the BTE and electronic transport using the Wigner Transport Equation [96]. There are some attempts to take into account the scattering time due to electrons in lattice drive thermal transport [97], but with the interaction only in one direction. On the other hand, for thermoelectric applications, the contributions of electrons and phonons is of similar magnitude, they can interact strongly with each other and they can both be “hot”, i.e. out of equilibrium effects and transient effect have to be take into account. Finally, in order to optimize the thermoelectric properties, one has to act on the extrinsic effects: interfaces and nanostructuring, which cannot be modeled accurately on the same scale of a DFT simulation. Some effect can be taken into account via Non-Equilibrium Green Functions (NEGF, for example as in Reference 98), other would require multi-scale modeling.

Solving this problem is not the task of a single person, for this reason I am participating in an effort of joined expertise on hot carriers, NEGF, transport by electron and phonon and their interaction and on solving coupled transport equations, with the perspective to produce a consistent theory, but also a set of computational tools sufficiently reliable to be used in high-throughput simulations [99, 100].

## 1.7 Structure of the manuscript

The aim of this work is to present in a coherent way my work on the theory of *ab initio* anharmonic lattice dynamics. In other words, the simulation of ionic vibration in crystal, from the harmonic level (phonons) including anharmonic interaction and the phenomena that they describe: phonon lifetimes, attenuation, featured vibrational spectra and thermal conductivity. This work represent the most important published results complemented by comprehensive discussion, which can take the entire corpus into account.

In Chapter 2.1, I will restate very briefly the theory of the harmonic crystal, to set the notation and highlight a few important specificities which will be relevant later on. In Chapter 2 I will quickly discuss on the perturbation theory to compute the intrinsic phonon lifetime, i.e. the lifetime that derives from phonon-phonon scattering. I will also present results about graphene and graphite, attenuation of sound waves in semiconductors and the complex spectra function of high anharmonic materials, with and application to hydrogen-rich Palladium. In Chapter 3, I will review the theory of thermal transport with a particular attention to extrinsic effects: finite size of samples and presence of defects. The theory will be accompanied by some results on graphene and graphite, bulk  $\text{Bi}_2\text{Se}_3$  with defects and  $\text{Bi}_2\text{Se}_3$  nano-slabs.

In Chapter 4, I will detail the challenges met in the study of strongly anharmonic material, where the development of a perturbative model on top of “standard” harmonic phonons is not possible. I will also report in more detail about a possible approach, the temperature dependent potential, which I have been developing more recently, and show some unpublished result on the sampling of thermal vibration phase space using different kind of deterministic (Newtonian) and stochastic (Langevin) molecular dynamics. In Section 4.2 I will confront the open main challenges of the field and list some perspective of future research.

The last four chapters are presented as appendices. They are written in a more informal but also detailed way, which allows me to go much deeper into technical topics which are rarely discussed in the published literature, with the aim of serving as reference for future students taking on these projects. They are recommended for the more interested reader, but are not essential for understanding the rest of the work. In Appendix A, I will detail the operations of Fourier transform and interpolation that relate real space (force constant) and reciprocal space (phonon) representation of crystal vibrations. In Appendix B I’ll discuss the enforcement and use of crystal symmetry in defining phonon modes and optimizing the search for temperature-dependent phonon energies. In Appendix C, I will detail the implementation of “ $2n+1$ ” theorem in the Quantum ESPRESSO code, to obtain efficiently and fully *ab initio* the matrix elements of the phonon-phonon coupling. Finally, in Appendix D, I give a brief description of the computer codes which have been developed and used for all the results reported above.

As this work includes excerpts and results from previous publication, the writing style will vary. The entirety of the text has been written by the author, during the course of collaboration with many people from different research groups, which are cited at the beginning of the relevant sections.

## Chapter 2

# Intrinsic lifetime of phonons

### 2.1 Harmonic Lattice Theory

At the Born-Oppenheimer approximation level, we assume that the ions (atomic nuclei and “rigid” deep core electrons) move so much slower than the valence electrons that the latter can be considered to always be at equilibrium during dynamics. The wavefunctions of the electronic and ionic part of the problem can be solved independently. This is not the same as considering the ions to be classical charged particles, as it does not preclude the quantum treatment of ions. More precisely the assumption is that one can define a multi-dimensional “energy landscape” which depends parametrically on the position of the ions.

Let us consider the total energy of a crystal  $\mathcal{E}(v_i)$ , where  $v_i$  are some external parameter, i.e. in this case the displacement of the atoms from their equilibrium position. The energy can be expanded in a multidimensional Taylor series around the point  $\mathbf{v} = 0$ :

$$\mathcal{E}(\{v_{\mathbf{R},s,\alpha}\}) = \mathcal{E}^0 + \sum_i \left. \frac{\partial \mathcal{E}}{\partial v_i} \right|_{v_i=0} v_i + \frac{1}{2} \sum_{i,j} \left. \frac{\partial^2 \mathcal{E}}{\partial v_i \partial v_j} \right|_{v_i=0, v_j=0} v_i v_j + \dots \quad (2.1)$$

Where  $\mathcal{E}^0 = \mathcal{E}(0)$ , the indices  $i$  and  $j$  are composite that take into account the unit-cell, defined by its vector  $\mathbf{R}$ , a cartesian direction  $\alpha = x, y$  or  $z$  and potentially the index  $s$  of the atom inside the lattice. The first derivative is the opposite of the force  $f_i = -\frac{\partial \mathcal{E}}{\partial v_i}$  acting on the atoms, it is vanishing when the system is relaxed. If the system is a periodic crystal, the usual reciprocal-space techniques can be used, transforming the approach from atomic displacements to phonons, i.e. periodic perturbations with a precise wavevector.

We define the periodic displacements  $u$  in the following way:

$$u_{\mathbf{q},s,\alpha} = \frac{1}{N} \sum_{\mathbf{R}} e^{-i2\pi\mathbf{q}\cdot\mathbf{R}} v_{\mathbf{R},s,\alpha}, \quad (2.2)$$

where the sum is performed on the lattice vectors  $\{\mathbf{R}\}$  and  $N$  is the number of cells considered in the summation. We define the dynamical matrix as derivative with respect to these displacements:

$$D \begin{pmatrix} \mathbf{q} \\ s \ s' \\ \alpha \ \alpha' \end{pmatrix} = \frac{1}{N} \frac{\partial^2 \mathcal{E}^{\text{tot}}}{\partial u_{-\mathbf{q},s,\alpha} \partial u_{\mathbf{q},s',\alpha'}}, \quad (2.3)$$

the pulsation  $\omega_{\mathbf{q},j}$  of a phonon with wavevector  $\mathbf{q}$  and branch index  $j$  is obtained by solving

$$\sum_{s',\alpha'} \frac{1}{\sqrt{m_s m_{s'}}} D_2 \begin{pmatrix} \mathbf{q} \\ s \ s' \\ \alpha \ \alpha' \end{pmatrix} z_{s',\alpha'}^{\mathbf{q},j} = \omega_{\mathbf{q},j}^2 z_{s,\alpha}^{\mathbf{q},j}, \quad (2.4)$$

where  $\mathbf{z}$  are the orthogonal phonon eigenmodes, or polarization vectors, and  $m_s$  is the mass of atom type  $s$ . In real space one can define the “force constants”  $F$  that describe the two-body interaction between atoms:

$$F \begin{pmatrix} \mathbf{R} \ \mathbf{R}' \\ s \ s' \\ \alpha \ \alpha' \end{pmatrix} = \frac{\partial^2 E}{\partial \mathbf{r}_{i,\mathbf{R}}^\alpha \partial \mathbf{r}_{i',\mathbf{R}'}^\beta}. \quad (2.5)$$

Using the definition of  $u$ , and considering that the position of atom  $i$  in cell  $\mathbf{R}$  is just  $\mathbf{R} + \tau_{i,\mathbf{R}} + \mathbf{v}_{i,\mathbf{R}}$ , where  $\tau$  is the basis of the crystal cell, we can see that force constants and dynamical matrices are related by a Fourier transform :

$$D \begin{pmatrix} & \mathbf{q} \\ s & s' \\ \alpha & \alpha' \end{pmatrix} = \sum_{\mathbf{R}} e^{i2\pi\mathbf{q}\cdot\mathbf{R}} F \begin{pmatrix} \mathbf{R} & \mathbf{0} \\ s & s' \\ \alpha & \alpha' \end{pmatrix}. \quad (2.6)$$

Where by using translational invariance, we got rid of one of the sums. A large fraction of the computational work is to manipulate these quantities and to interpolate them. More details about transforms, symmetrization and interpolation are available in Appendix A and B

We point out that the expansion of eq. 2.1 is not unique in several ways. As  $\mathcal{E}(v_i)$  is a smooth analytical function, it can be approximated with a Taylor polynomial around any point  $\mathbf{v}$ , because we are only interested in mechanically stable materials, we may want to limit ourselves to the points where  $\mathbf{f} = 0$ , yet we could still find local minima or saddle points where to perform the expansion. Furthermore, we observe that the Taylor method is not the only way to approximate a function with a polynomial, e.g. instead of building a polynomial that shares its derivatives with our function, we could use one that crosses the function in a given number of point, or, as we will see in Section 4.1 the polynomial that “better” approximates our function in a given range, i.e. the range of thermal rattling of the atoms.

Different methods to construct the polynomial will have different second-order terms, and as a consequence, different phonon frequencies. In a perfect harmonic limit, there is no ambiguity, the problem emerges when introducing anharmonicity: if we treat higher order as perturbations on top of the harmonic terms, we will have a unique result only in the perturbative limit. On the other hand, the second order, i.e. the harmonic phonons, and the magnitude of each order of the corrections will differ. Because perturbation theory becomes very quickly prohibitively expensive, we prefer an approximation that gives the “best” harmonic solution with the smallest possible anharmonic corrections. Again, different approaches are possible we will review them in Chapter 4.

## 2.2 Ab initio phonon lifetime

As we have seen in Section. 1.1 that the intrinsic phonon scattering probability can be computed perturbatively from the third order of the Hamiltonian polynomial expansion, and that this third order can be computed in DFPT via the “2n+1” theorem; the first implementations of the “2n+1” approach were limited to the scattering of one zero-momentum phonon towards two phonons with opposite arbitrary momenta  $(\mathbf{0}, -\mathbf{q}, \mathbf{q})$ . Refs. 101 and 102 implemented this approach for insulating and semiconducting materials. Later Ref. 103 extended the approach to metals and zero-gap materials. Following our implementation of Ref. 25, the generic  $(\mathbf{q}_1, \mathbf{q}_2, \mathbf{q}_3)$  anharmonic coefficients can be computed using Quantum ESPRESSO [104, 105], using the `d3q.x` code.

Once the third derivative is available, a first application is to compute the phonon lifetime in a perturbative way: the harmonic phonons are used as the unperturbed and the third order term of the Hamiltonian is the perturbation. This expansion has been studied in detail in many papers, we followed the development of Ref. 106. A point to note is that the first perturbative order include both three-phonon and four-phonon scattering contribution to the phonon self-energy. However, the four-phonon terms is real, i.e. only contributes a shift of the phonon frequencies. The three-phonon term is complex, and contributes both a linewidth (its imaginary part) and a lineshift (its real part). As long as the phonon frequency is large compared with its shift, it is not inaccurate to consider only the three-phonon terms in the linewidth.

*This chapter reports some of the most significant result from references 25, 48 and 107.*

## 2.3 Anharmonic decay

Following the development of Reference 106 we define the three-phonon scattering coefficient as

$$V_{\mathbf{q}j,\mathbf{q}'j',\mathbf{q}''j''}^{(3)} = \frac{1}{N} \frac{\partial^3 \mathcal{E}^{\text{tot}}}{\partial X_{\mathbf{q},j} \partial X_{\mathbf{q}',j'} \partial X_{\mathbf{q}'',j''}}, \quad (2.7)$$

where

$$\frac{\partial}{\partial X_{\mathbf{q},j}} = \sum_{s,\alpha} \sqrt{\frac{\hbar}{2m_s \omega_{\mathbf{q},j}}} z_{s,\alpha}^{\mathbf{q},j} \frac{\partial}{\partial u_{\mathbf{q},s,\alpha}}. \quad (2.8)$$

$V^{(3)}$  is an energy and does not depend on  $N$ , while  $X_{\mathbf{q},j}$  is adimensional. Because of the translational symmetry of the crystal the coefficients  $V^{(3)}$  from Eq. 2.7 are  $\neq 0$  only when  $\mathbf{q} + \mathbf{q}' + \mathbf{q}'' = \mathbf{G}$ , where  $\mathbf{G}$  is a reciprocal lattice vector.

With these definitions, the lifetime due to anharmonic phonon-phonon interaction,  $\tau_{\mathbf{q}j}$ , and the corresponding broadening  $\gamma_{\mathbf{q}j}$  (full width at half maximum) of the phonon ( $\mathbf{q}j$ ) are [108]:

$$\frac{1}{\tau_{\mathbf{q}j}(T)} = 2\gamma_{\mathbf{q}j}(T) = \frac{\pi}{\hbar^2 N_q} \sum_{\mathbf{q}',j',j''} \left| V_{\mathbf{q}j,\mathbf{q}'j',\mathbf{q}''j''}^{(3)} \right|^2 \times \left[ (1 + n_{\mathbf{q}'j'} + n_{\mathbf{q}''j''}) \delta(\omega_{\mathbf{q}j} - \omega_{\mathbf{q}'j'} - \omega_{\mathbf{q}''j''}) + 2(n_{\mathbf{q}'j'} - n_{\mathbf{q}''j''}) \delta(\omega_{\mathbf{q}j} + \omega_{\mathbf{q}'j'} - \omega_{\mathbf{q}''j''}) \right]. \quad (2.9)$$

Where  $T$  is the temperature,  $n_{\mathbf{q}j}$  is the Bose-Einstein statistics occupation of the phonon ( $\mathbf{q}j$ ) and  $\delta(x)$  is the Dirac distribution. The sum is performed on a sufficiently fine grid of  $N_q$   $\mathbf{q}$ -points in the Brillouin zone (BZ) and  $\mathbf{q}'' = -\mathbf{q} - \mathbf{q}'$ .  $\tau_{\mathbf{q}j}$  and  $\gamma_{\mathbf{q}j}$  depend on  $T$  only through the phonon occupations  $n$ .

The r.h.s. of Eq. 2.9 is usually interpreted as the sum of scattering processes in which a phonon with wavevector  $\mathbf{q}$  decays into two phonons  $-\mathbf{q}'$ ,  $-\mathbf{q}''$ , (third line of Eq. 2.9) or in which the phonon  $\mathbf{q}$  coalesces with  $-\mathbf{q}'$  and emits  $-\mathbf{q}''$  (fourth line of Eq. 2.9). The energy conservation of the processes are guaranteed by the Dirac delta. One can also distinguish between Normal and Umklapp processes: By choosing  $\mathbf{q}$  and  $-\mathbf{q}'$  such that they belong to the first BZ, the scattering is Normal when also  $\mathbf{q}'' = -\mathbf{q} - \mathbf{q}'$  belongs to the first BZ; on the contrary, when  $\mathbf{q}''$  does not belong to the first BZ, the scattering is Umklapp.

By knowing the anharmonic scattering coefficients, Eq. 2.7, one can also determine the lattice thermal conductivity within the framework of the Boltzmann transport equation (BTE) for phonons [109]. In general, an exact solution of the BTE is a very difficult task and a commonly used approximation to the problem is the, so called, single mode relaxation time approximation [23, 110–113]. Within the SMA, the lattice thermal conductivity tensor is

$$\kappa_L^{\alpha,\beta} = \frac{\hbar^2}{N_q \Omega K_B T^2} \sum_{\mathbf{q}j} c_{\mathbf{q}j}^\alpha c_{\mathbf{q}j}^\beta \omega_{\mathbf{q}j}^2 n_{\mathbf{q}j} (n_{\mathbf{q}j} + 1) \tau_{\mathbf{q}j}. \quad (2.10)$$

Here,  $\Omega$  is the volume of the unit cell,  $K_B$  is the Boltzmann constant and  $c_{\mathbf{q}j}^\alpha$  is the phonon group velocity of the mode ( $\mathbf{q}j$ ) along the Cartesian direction  $\alpha$ :  $c_{\mathbf{q}j}^\alpha = d\omega_{\mathbf{q}j}/(dq_\alpha)$ . The SMA conductivity from Eq. 2.10 can be obtained in a straightforward way once the anharmonic lifetimes  $\tau_{\mathbf{q}j}$  have been computed from Eq. 2.9.  $\kappa_L^{\alpha,\beta}$  is a  $3 \times 3$  tensor which takes into account the possible anisotropies and transversal conductance. However, in high-symmetry crystals, as graphene and graphite, the off-diagonal elements are zero. Moreover, in both graphene and graphite the two in-plane  $xx$  and  $yy$  components are identical. The out-of-plane  $zz$  component is not well defined in the bidimensional graphene systems, but it is meaningful in graphite.

The validity limits of the SMA are discussed in literature [23, 110–113]. Here, we just remind that, for a generic material, the SMA is expected to be valid (that is, to provide the correct solution to the BTE) at room conditions and to break down only at very small temperatures (see, *e.g.* 114, 115). As a matter of fact, however, a direct verification of the SMA (that is, a direct comparison with the conductivity obtained by solving exactly the BTE) has been attempted only in a few cases [114, 115] and an absolutely general statement cannot be done.

## 2.4 Application: Graphene and Graphite phonon lifetimes

Calculations of the phonon properties are done within density functional perturbation theory [116] as implemented in 105. The third order coefficients defined in Eq. 2.7 are computed using a code which has been developed for the present work. This code has been written on the top of a previous less general implementation available within the Quantum-ESPRESSO package: The D3 code, which was implemented

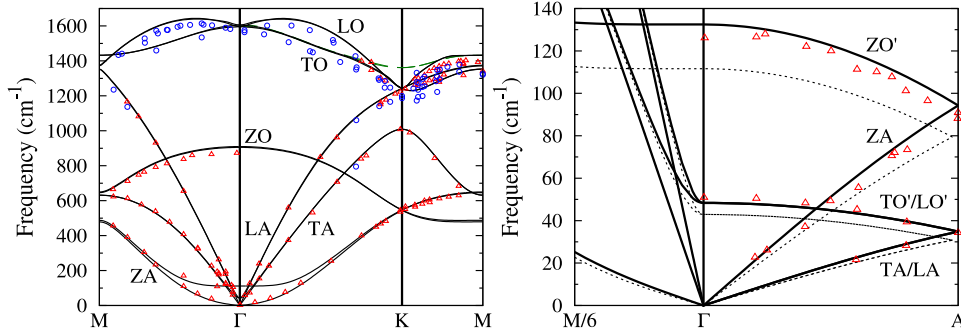


Figure 2.1: Graphite phonon dispersion. Symbols are measurements from [117, 118]. Lines are calculations. In the right panel, the TO optical branches are plotted two times. The solid (black) lines include GW corrections of the electron-phonon interaction. On the contrary the dashed (green) lines are done using standard DFT and they are shown only for comparison. Left panel: Solid lines are done by using  $c/a = 2.664$ ; dashed lines are done with  $c/a = 2.727$  and they are shown only for comparison. In both panels, the solid lines correspond to the calculations used throughout the paper.

in [103]. The present code allows the calculations of  $V_{\mathbf{q},\mathbf{q}',\mathbf{q}''}^{(3)}$  for any reciprocal space vector triplet such that  $\mathbf{q} + \mathbf{q}' + \mathbf{q}'' = \mathbf{G}$ , while the previous implementation was restricted to the case  $V_{\mathbf{0},-\mathbf{q},\mathbf{q}}^{(3)}$ . The method is described in Appendix C.1.

We use local-density approximation and the carbon atom is described by a hard norm-conserving pseudopotential which includes four electrons in valence. Plane waves kinetic energy cutoff is 90 Ry. For all the systems, the in-plane lattice parameter is  $a = 2.44 \text{ \AA}$ , which is the theoretical equilibrium value for graphite. For graphite, we use  $c/a = 2.664$ . This value, which is only slightly different from the experimental value  $c/a = 2.727$ , is chosen phenomenologically so as to accurately reproduce the low frequency phonon dispersion along the  $\Gamma - A$  direction. For graphene, the periodic replicas of the planes are spaced along the  $z$  direction with  $7 \text{ \AA}$  of vacuum. The two layers of the graphene bilayer are spaced with the inter-planar distance of bulk graphite; periodic images are then spaced with  $7 \text{ \AA}$  of vacuum.

The computational details are described in Appendix 2.4.1. Here we just remind that the electronic integration needs to be done using a small smearing value (and a consequent fine-grained  $\mathbf{k}$ -point grid) because of the presence of a Kohn anomaly for the highest optical branch near  $\mathbf{K}$  [119] (usually called TO). The phonon frequencies  $\omega_{\mathbf{q}j}$  and the third-order coefficients  $V^{(3)}$ , which are used in Eqs. 2.9 and 2.10, are calculated in a slightly different way. On one hand, phonon energies are corrected using an ad-hoc procedure (based on DFT+GW renormalization of the electron-phonon interaction as in Ref. [120], see also Appendix 2.4.1). This correction affects only the TO branch, it does not touch the other branches, and it provides better agreement with measurements, Fig. 2.1. On the other hand, the third-order coefficients are computed within standard (less precise) DFT. The use of these two different procedures for the  $\omega_{\mathbf{q}j}$  and  $V^{(3)}$  calculations is not consistent. However, this should not affect the results in a major way. Indeed, the phonon broadening results from a sum on different processes which are selected by energy conservation implemented by the two Dirac  $\delta$  in Eq. 2.9. The intensity of the processes is then proportional to the square of the  $V^{(3)}$  coefficients. Because of this, the accuracy of the computed  $\omega_{\mathbf{q}j}$  and that of the  $V^{(3)}$  coefficients affect the result in a very different way. An error in the phonon dispersion can affect the lifetime in a not predictable way and, thus, a special care should be taken into finding the best possible description of the phonon dispersion. The same care is not strictly necessary for the third order calculations.

Fig. 2.1 compares measured with calculated phonon dispersions for graphite. Notice that plain DFT calculations do not provide a satisfactory description of the highest optical TO branch near  $\mathbf{K}$ , while DFT+GW ones do much better. The higher panel of Fig. 2.1 shows in detail the low frequency dispersion. This region is characterized by the splitting of the acoustic phonon branches of the two graphene planes in the graphite unit cell. These branches are particularly sensitive on the actual value of  $c/a$ . In particular, in that region, by changing the lattice parameters from  $c/a = 2.664$  (which is the value used throughout the paper) to  $c/a = 2.727$  the phonon branches change by almost 14%.

Actual DFT calculations are done on a relatively coarse grid of  $\mathbf{q}$  wavevectors, described in Section 2.4.1.

The dynamical matrices and the third order coefficients, that are necessary to compute the broadening and the thermal conductivity (Eqs. 2.9 and 2.10) are then obtained for a finer grid with the Fourier interpolation technique described in Appendix A.5. Eqs. 2.9 and 2.10 are evaluated by performing the sum over a discrete grid of  $\mathbf{q}$  points and by substituting the  $\delta(x)$  with a Gaussian function characterized by an artificial smearing  $\chi$ . This approximation is valid as long as  $\chi$  is smaller than the thermodynamic fluctuation, which is of order  $K_B T$ . The grids and the  $\chi$  values are specified in Section 2.4.1. Here we just remark that the results shown in Sects. 2.4.2 and 2.4.3 are obtained using a particularly fine-grained sampling. This is only necessary to produce the very sharp features which are present in the broadening of the higher optical bands or to produce the correct behavior of the broadening of the acoustic branches in the vicinity of  $\Gamma$ . Indeed, a much coarser grid is sufficient for most applications, as those of Sec. 3.2.1.

## 2.4.1 Computational details

### Electronic integration

The electronic integration of the density functional theory calculations is done using a first-order Methfessel-Paxton smearing[121] of 0.02 Ry which converges for a grid of  $32 \times 32 \times 1$  electronic  $\mathbf{k}$ -points in simple and bilayer graphene and for a grid of  $32 \times 32 \times 8$   $\mathbf{k}$ -points for graphite.

### Linear response calculations

DFT dynamical matrices are corrected using a procedure based on DFT+GW renormalization of the electron-phonon interaction as in 120. Indeed, DFT reproduces very well the measured dispersions of graphite for all the phonon branches but for the TO one, in the vicinity of the high symmetry point  $\mathbf{K}$ . This failure of DFT, which is very specific to the graphene and graphite systems, has been analyzed in Ref. 120. To improve the accuracy of the TO phonon branch, we have applied an electron-phonon self-interaction as described in Ref. 120. The detailed procedure is described in Sec. IIB of 122 (third paragraph). We have used the parameter  $r^{GW} = 1.65$ , which is appropriate to the present LDA calculations and which can be derived from Table I of 120. Using this approach we determined the dynamical matrices of graphene on a super-sampled  $48 \times 48 \times 1$   $\mathbf{q}$ -point grid. The matrices for the graphite and for the bilayer are then obtained by using as in-plane force constants those of graphene and as out-of-plane force constants those coming from independent DFPT calculations on the two systems.

The third order coefficients are obtained in the standard way, that is without including this self-interaction correction of reference [120]. For graphene, the third-order coefficients are calculated on a  $8 \times 8 \times 1$   $\mathbf{q}$ -point grid, meaning that we have calculated every triplet  $(\mathbf{q}, \mathbf{q}', \mathbf{q}'')$  of points, such that  $\mathbf{q}$  and  $\mathbf{q}'$  belong to the grid and that the condition  $\mathbf{q} + \mathbf{q}' + \mathbf{q}'' = 0$  is satisfied. In practice, if one choses  $\mathbf{q}$  and  $\mathbf{q}'$  so that they belong to the grid,  $\mathbf{q}'' = -\mathbf{q} - \mathbf{q}'$  may not belong to the grid.  $\mathbf{q}''$  is however still connected to a point in grid by a reciprocal lattice vector translation. The double-sum over the  $8 \times 8 \times 1$  grid includes 4096 points, but after taking symmetry in account, it can be reduced to a total of 88 non-self-consistent third-order response calculations. For bulk graphite, third-order coefficients are calculated on a  $8 \times 8 \times 2$  grid, which consists in 297 irreducible  $\mathbf{q}$  triplets. When computing the linewidth, we have tested convergence starting from the  $8 \times 8 \times 2$  grid coefficients, finding that the use of the those from the  $4 \times 4 \times 2$  subset grid (33 inequivalent triplets) does not worsen accuracy. For bilayer graphene, the third-order coefficients are calculated on a  $4 \times 4 \times 1$   $\mathbf{q}$ -point grid (12 irreducible triplets).

### Linewidth calculations

Eqs. 2.9 and 2.10 are evaluated by performing the sum over a discrete uniform grid of  $\mathbf{q}$  points randomly shifted from the origin. The  $\delta(x)$  distribution is substituted with the gaussian function  $\tilde{\delta}(x) = e^{-(x/\chi)^2} / (\chi\sqrt{\pi})$ , where  $\chi$  is an artificial smearing, independent from  $\mathbf{q}$ . The results of Sects. 2.4.2 and 2.4.3 are obtained by using: For graphene, a  $1800 \times 1800 \times 1$  grid and  $\chi = 1 \text{ cm}^{-1}$ ; for graphite, a  $600 \times 600 \times 15$  grid and  $\chi = 5 \text{ cm}^{-1}$ ; for the bilayer, a  $1200 \times 1200 \times 1$  grid and  $\chi = 2 \text{ cm}^{-1}$ . The results of Sec. 3.2.1 are obtained by using: For graphene, a  $128 \times 128 \times 1$  grid and  $\chi = 10 \text{ cm}^{-1}$ ; for graphite and bilayer, a  $64 \times 64 \times 4$  grid and  $\chi = 10 \text{ cm}^{-1}$ . For each system, the same grid is used to determine the linewidth from Eq. 2.9 and the thermal conductivity from Eq. 2.10. The convergence, has been tested using smaller values of smearing and finer grids at selected values of temperature.

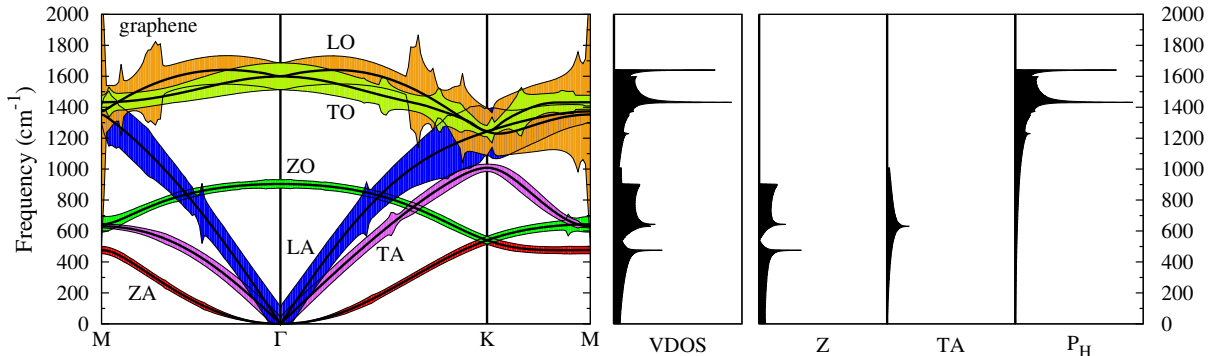


Figure 2.2: Calculated graphene phonon dispersion. Each phonon branch is represented with a variable-width filled band: the graphical width is equal to the respective anharmonic broadening at 300 K, expressed in  $\text{cm}^{-1}$  and magnified by a factor 100. The vibrational density of states (VDOS) is also shown, together with its decomposition over groups of disentangled branches labeled as Z (corresponding to the ZA and ZO branches), TA and  $P_H$  (corresponding to LA, TO, and LO).

## 2.4.2 Graphene phonon broadening

Fig. 2.2 shows the calculated graphene phonon dispersion, the respective anharmonic broadening and the vibrational density of states (VDOS). The branches are labeled in the usual way [123]. There are three acoustic branches (ZA, TA, LA) and three optical ones (ZO, TO, LO). ZA and ZO correspond to an atomic motion perpendicular to the graphene plane ( $z$  direction), all the other branches are polarized parallel to the plane. In the vicinity of  $\Gamma$ , TA and TO are quasi transverse, while LA and LO are quasi longitudinal. In the following, these labels will be used to classify the branches all along the high symmetry lines (as in Fig. 2.2), although this distinction is not meaningful for an arbitrary wavevector in the Brillouin zone (BZ). Because of symmetry, the modes perpendicular polarized (ZA and ZO) are separated from the others all over the BZ. Moreover, the TA branch is always well separated from the other parallel polarized branches (labeled as  $P_H$ ). In Fig. 2.2, we can, thus, separate the VDOS in three distinct components labeled as Z, TA, and  $P_H$ . The two dimensional character of the phonon dispersion is associated with some specific features. The ZA branch is quadratic near  $\Gamma$  and, thus, in the limit  $\omega \rightarrow 0$  the VDOS does not go to zero (Fig. 2.2). The presence of a local maximum in the phonon dispersion (as the one at  $1008 \text{ cm}^{-1}$  for the TA branch near  $\mathbf{K}$  or the one at  $904 \text{ cm}^{-1}$  for the ZO one near  $\Gamma$ ) is associated with a step in the VDOS. The presence of a saddle shaped dispersion (as those at  $477$ ,  $631$ ,  $643$ , and  $1432 \text{ cm}^{-1}$  at  $\mathbf{M}$ ) is associated with a sharp peak in the VDOS.

Fig. 2.3 reports in more detail the calculated anharmonic phonon broadening, along high symmetry lines, and its decomposition into the different possible decay channels. For symmetry reasons, the  $z$ -polarized branches, can only decay toward one Z and one non-Z phonons. The other bands can only decay towards two phonons which are either both or neither  $z$ -polarized. The two most striking features in Figs. 2.2, 2.3 are the small  $q$  behavior of the acoustic branches and the highly non uniform behavior of the broadening.

First, we remind that in a three dimensional isotropic crystal, all the three acoustic branches are linearly dispersive and one expects to observe for  $q \rightarrow 0$  a vanishing broadening. On the contrary, at finite temperature, both TA and LA branches of the two dimensional graphene have a non-zero broadening in the  $q \rightarrow 0$  limit. This behavior is due to the decay into two phonons both in the ZA branch, Fig. 2.3. This decay is Normal (see the definition in Sec. 2.3). Actually, one can easily demonstrate that, in general, when a linearly dispersive phonon decays into two quadratically dispersive phonons, the broadening is non vanishing in the  $q \rightarrow 0$  limit because of energy and momentum conservation (see Ref. 24 for a more detailed discussion). Moreover, the quadratically dispersive ZA branch has a broadening which is itself quadratic in  $q$  around  $\Gamma$ . The ZA broadening is due to a Normal decay into one ZA phonon and on linearly dispersive, TA or LA, phonon. Again, one can demonstrate that, in general, when a quadratically dispersive phonon decays into one quadratically and one linearly dispersive phonon, the broadening vanishes quadratically in the  $q \rightarrow 0$  limit. We remark that, here, the anharmonic broadening has been computed by summing over an extremely fine reciprocal-space grid (see Appendix 2.4.1). This is necessary in order to reproduce correctly the anomalous behavior of the LA and TA broadening for small  $q$ . Far from  $\Gamma$ , the details of the broadening can be correctly reproduced by using a much coarser

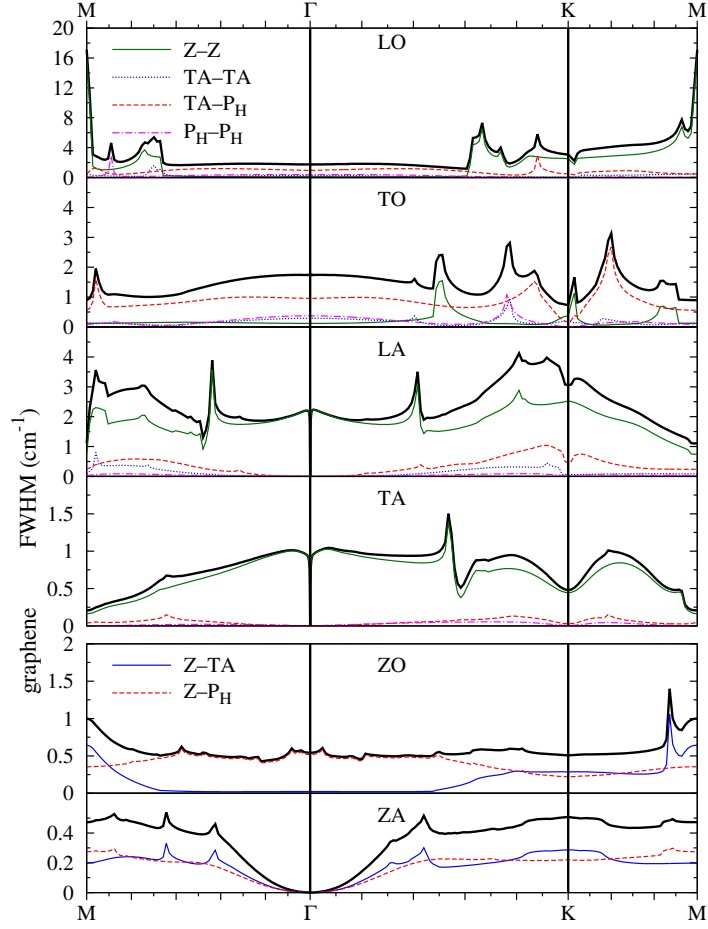


Figure 2.3: Graphene anharmonic phonon broadening (FWHM) at 300 K, for each phonon branch (labeled as in Fig. 2.2), along high symmetry lines. The total broadening (solid thick line) is decomposed depending on the character of the final states which are labeled as Z, TA, and  $P_H$  (see the text): *e.g.* TA- $P_H$  corresponds to a decay involving one TA and one  $P_H$  phonon.

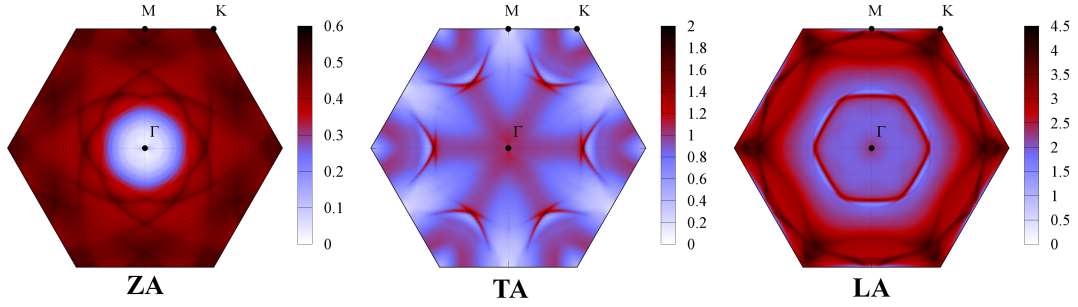


Figure 2.4: Graphene anharmonic phonon broadening (FWHM) in  $\text{cm}^{-1}$  at 300 K, for the three acoustic branches, over the Brillouin zone.

grid.

The existence of a finite broadening at small  $q$  for the TA and LA acoustic branches is problematic. Indeed, the concept itself of phonon is meaningful only when  $\omega/\gamma > 1$ , being  $\gamma$  the broadening (*i.e.* the inverse of the phonon lifetime). From the present calculations, the condition  $\omega/\gamma > 1$  is satisfied for both the TA and LA branches for  $q > \bar{q}$ , with  $\bar{q} = 0.5 \times 10^{-4} 2\pi/a_0$ , being  $a_0$  the in-plane lattice spacing. Thus, for  $q < \bar{q}$ , the TA or LA frequency can become smaller than the broadening. In this region the present treatment is, obviously, not valid (see the discussion in 24) and a proper treatment of the phenomenon is beyond the present scope. In practice, however,  $q < \bar{q}$  represents a tiny portion of the Brillouin zone (the corresponding region in Figs. 2.2, 2.3 has width of the order of the thickness of the vertical line passing through  $\Gamma$ ). As a consequence, we can assume that those properties which are obtained as a sum all over the Brillouin zone (such as the thermal conductivity of Eq. 2.10) are not affected by a major error.

Concerning the global appearance of Figs. 2.2, 2.3, the many sharp peaks in the broadening can be ascribed to different mechanisms. Those in the highest part of the spectrum are, generally, associated with peaks in the VDOS: When one or both of the final states (*i.e.* of the states that meet energy and momentum conservation requirements in Eq. 2.9) produce a peak in the VDOS, there the broadening typically exhibits a peak. For example, the large scattering probability, predicted for the  $\mathbf{M}$  point on the LO branch ( $1373 \text{ cm}^{-1}$ ), correspond to a decay toward a ZO phonon close to  $\Gamma$  ( $904 \text{ cm}^{-1}$ ) and a ZA phonon close to  $\mathbf{M}$  ( $477 \text{ cm}^{-1}$ ). As the VDOS, Fig. 2.2, has maximum in both region, this transition is particularly favored. On the other hand, for  $\mathbf{q} \gtrsim 0.66\mathbf{M}$  (along the  $\Gamma\mathbf{M}$  direction) or for  $\mathbf{q} \gtrsim 0.62\mathbf{K}$  (along  $\Gamma\mathbf{K}$ ), the LO broadening displays a sudden increase. This is because, for these wavevectors, the LO energy has become small enough to activate the decay channel towards the ZO branch (At  $\mathbf{q} \sim 0.66\mathbf{M}$  and  $\mathbf{q} \sim 0.62\mathbf{K}$  the LO phonon decays into a ZO with the same wavevector and a ZO with  $\mathbf{q} \sim \Gamma$ ).

We remark that the presence of sharp peaks which are essentially determined by energy and momentum conservation in the decay process implies that even a small change in the phonon dispersion which is used in the calculation could provide significant differences on the calculated broadening. This should be considered while comparing with the present calculations.

Concerning the three acoustic branches, the broadening near  $\Gamma$  is almost entirely due to Normal scattering. The peaks which are observed at  $\mathbf{q} \gtrsim 0.44 \mathbf{M}$  and  $\mathbf{q} \gtrsim 0.41 \mathbf{K}$  for the LA branch, and at  $\mathbf{q} \gtrsim 0.65 \mathbf{M}$  and  $\mathbf{q} \gtrsim 0.54 \mathbf{K}$  for the TA one, are associated with the activation of Umklapp scattering towards the ZA phonons. To have a more comprehensive view, Fig. 2.4 reports the broadening in the entire Brillouin zone. The TA and LA branches exhibit a feature-rich behavior in a wide region, far from  $\Gamma$ , which roughly starts at about halfway to the first BZ edge. In this region, the anharmonic decay presents a component of Umklapp processes, which is absent in the vicinity of  $\Gamma$ , where the scattering is almost entirely Normal. On the other hand, the ZA broadening is relatively feature-less and isotropic; it is quadratic in  $\mathbf{q}$  in the center of the first BZ then it saturates and become relatively constants.

#### 2.4.2.1 Phonon mean free path

An alternative way to represent the effect of the phonon broadening is to plot the single-phonon mean free path (MFP):

$$\lambda_{\mathbf{q}j} = \tau_{\mathbf{q}j} |\mathbf{c}_{\mathbf{q}j}|, \quad (2.11)$$

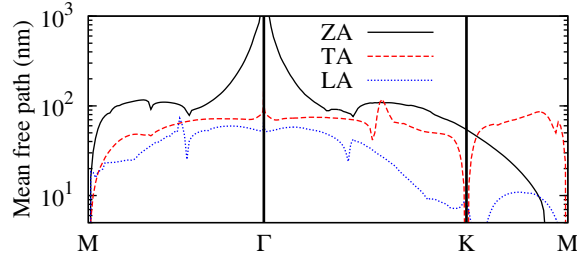


Figure 2.5: Phonon mean free path (MFP) for the three acoustic branches in graphene at 300 K. A peculiar characteristic is the diverging MFP for the acoustic band at Gamma

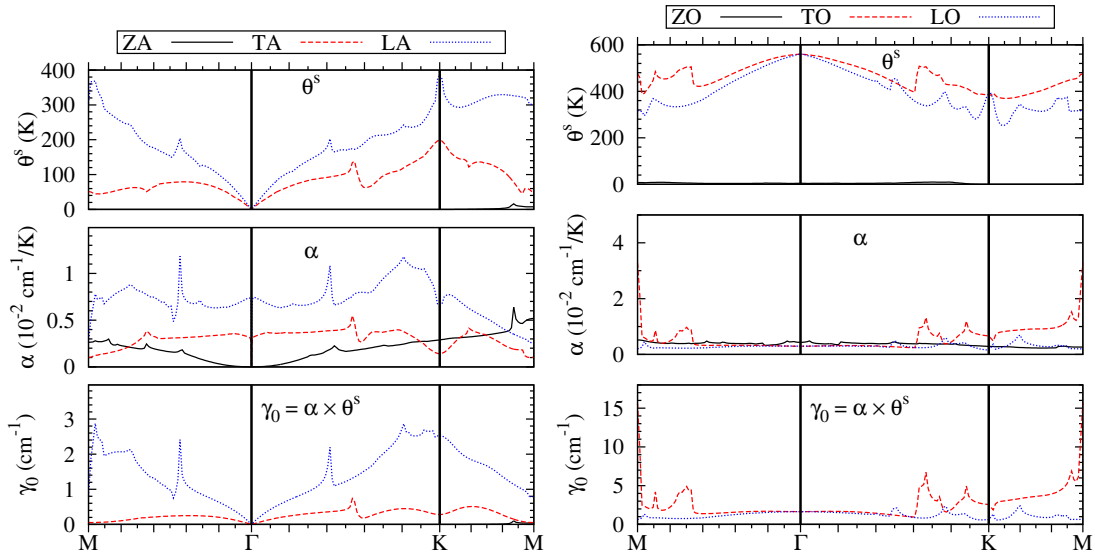


Figure 2.6:  $\theta^S$  and  $\alpha$  parameters (defined in the text) for the graphene acoustic (left) and optical (right) branches. For a given phonon mode, the temperature dependence of the anharmonic broadening can be approximated by  $\gamma(T) \simeq \alpha \theta^S \coth(\theta^S/T)$ , where  $\theta^S$  and  $\alpha$  are the parameters corresponding to that phonon.  $\theta^S$  is a characteristic temperature and  $\alpha$  is the high temperature slope of  $\gamma(T)$ .  $\gamma_0$  is the  $T = 0$  K broadening.

where  $\mathbf{c}_{\mathbf{q}j}$  is the phonon group velocity and  $\tau_{\mathbf{q}j}$  is the phonon lifetime, from Equation 2.9. In figure 2.5 we have plotted the MFP at 300 K for the three acoustic branches. The MFP for the TO and LO bands is of order 100 nm or smaller. We have verified that it does not get substantially higher at lower temperatures, except in the vicinity of  $\Gamma$  where it diverges at 0 K. On the other hand, at room temperature, the MFP of the ZA bands is one order of magnitude larger, i.e. of order  $1 \mu\text{m}$ , in the center region of the Brillouin zone. Also, it increases linearly when temperature decreases. Obviously, especially at small temperatures, when the intrinsic anharmonic MFP is too big other effects (typically the scattering with the borders of the sample) become determinant and determine the value of the MFP. We remark that the MFP of acoustical phonons is only one order of magnitude smaller than typical dimensions of high-quality graphene samples. It is, also, definitely larger than the transverse dimension of graphene nano-ribbons. This result suggests that ballistic phonon-driven conductance could be relevant in this kind of systems.

#### 2.4.2.2 Temperature dependence

The intrinsic anharmonic broadening of a specific phonon ( $\mathbf{q}j$ ) has, in general, a typical dependence of the temperature  $T$ : It is almost constant below a certain characteristic temperature  $\theta^S$ , then it rapidly becomes linear in  $T$ . Such a behavior is reproduced by Eq. 2.9. A quadratic dependence on  $T$  can be observed only at relatively high  $T$  and it is due to terms of order higher than those included in Eq. 2.9 [124].

From Eq. 2.9, one can check that

$$\lim_{T \rightarrow \infty} \gamma_{\mathbf{q}j}(T) = \alpha_{\mathbf{q}j}T + \mathcal{O}(1/T), \quad (2.12)$$

where

$$\begin{aligned} \alpha_{\mathbf{q}j} = & \frac{\pi K_B}{\hbar^3 N_q} \sum_{\mathbf{q}', j', j''} \left| V_{\mathbf{q}j, \mathbf{q}'j', \mathbf{q}''j''}^{(3)} \right|^2 \times \\ & \left[ \left( \frac{1}{\omega_{\mathbf{q}'j'}} + \frac{1}{\omega_{\mathbf{q}''j''}} \right) \delta(\omega_{\mathbf{q}j} - \omega_{\mathbf{q}'j'} - \omega_{\mathbf{q}''j''}) + \right. \\ & \left. 2 \left( \frac{1}{\omega_{\mathbf{q}'j'}} - \frac{1}{\omega_{\mathbf{q}''j''}} \right) \delta(\omega_{\mathbf{q}j} + \omega_{\mathbf{q}'j'} - \omega_{\mathbf{q}''j''}) \right] \end{aligned} \quad (2.13)$$

does not depend on  $T$ . One can thus be tempted to approximate the overall dependence on  $T$  of the broadening  $\gamma$  by

$$\gamma_{\mathbf{q}j}(T) \simeq \tilde{\gamma}_{\mathbf{q}j}(T) = \alpha_{\mathbf{q}j} \theta_{\mathbf{q}j}^S \coth \left( \frac{\theta_{\mathbf{q}j}^S}{T} \right), \quad (2.14)$$

where  $\coth$  is the hyperbolic cotangent,  $\theta_{\mathbf{q}j}^S = \gamma_{\mathbf{q}j}(0)/\alpha_{\mathbf{q}j}$ , and  $\gamma_{\mathbf{q}j}(0)$  is the  $T = 0$  broadening from Eq. 2.9. Indeed,  $\tilde{\gamma}$  from Eq. 2.14 is almost constant for  $T \ll \theta^S$  and tends to  $\gamma(0)$  for  $T \rightarrow 0$ . Moreover,  $\tilde{\gamma}(T) = \alpha T + \mathcal{O}(1/T)$  for  $T \gg \theta^S$ . To check the validity of this approximation (Eq. 2.14), we systematically computed the graphene broadening for different phonons in the temperature range between 0 and 1500 K, using Eq. 2.9. These results are reasonably well reproduced by Eq. 2.14 with an error less than 5%.

As a consequence, for a given phonon mode ( $\mathbf{q}j$ ), the knowledge of the two corresponding parameters  $\theta^S$  and  $\alpha$  is enough to determine the overall temperature behavior of the broadening, by using Eq. 2.14. The two parameters can be extracted from Fig. 2.6, for the graphene acoustic branches, along high symmetry lines.

Finally, the broadening of the LA and TA branches can be fitted with an isotropic function of  $q = |\mathbf{q}|$  and of  $T$  of the form:

$$\gamma(q, T) = qB \coth \left( \frac{qA}{T} \right). \quad (2.15)$$

By defining  $b_0 = \frac{2\pi}{a_0}$ , where  $a_0$  is the cell parameter, we have: for the LA band,  $B_{LA} = 4.58 \text{ cm}^{-1}/b_0$  and  $A_{LA} = 694 \text{ K}/b_0$ ; for the TA band,  $B_{TA} = 0.805 \text{ cm}^{-1}/b_0$  and  $A_{TA} = 241 \text{ K}/b_0$ . These fitted parameters reproduce the computed linewidth with an error of generally less than 10% for  $q < 0.40 b_0$ , the highest accuracy for higher temperature and lower  $|\mathbf{q}|$ . For the ZA band  $\theta^s$ , resulting in this simple fitting function:

$$\gamma(q, T) = Bq^2T. \quad (2.16)$$

Taking  $B_{ZA} = 25.9 \times 10^{-3} \text{ cm}^{-1}/b_0^2$  we reproduce the value of linewidth to 10% accuracy in the range  $q < 0.25 b_0$ , except for systematically underestimating it in the very small  $\mathbf{q}$  region where it is negligible ( $\gamma < 10^{-5} \text{ cm}^{-1}$ ).

### 2.4.3 Graphite and bilayer graphene

We now discuss the anharmonic broadening in graphite and graphene bilayer. Each of the six phonon branches of the graphene monolayer splits into two branches for both graphite and graphene bilayer. The three acoustic branches of graphene (ZA, TA, LA) split into three acoustic (ZA, TA, LA) and three quasi-acoustic branches (ZO', TO', LO'). The quasi-acoustic branches are almost degenerate with the respective acoustic one, except in the vicinity of the  $\Gamma$ -A line. The remaining six optical branches are pair-wise quasi-degenerate in the entire Brillouin zone, and they will be referred in pairs simply as ZO, TO and LO or, in some cases as ZO<sup>1</sup>, ZO<sup>2</sup>, etc. This notation does not hold along the  $\Gamma - A$  line in graphite, as the bands degeneracy changes. It is however still possible to name the branches by continuity below 600  $\text{cm}^{-1}$ .

Fig. 2.7 shows a general view of the calculated phonon dispersion and broadening in bulk graphite and graphene bilayer. Fig. 2.8a and Fig. 2.8b, compare the broadening of the acoustic and quasi-acoustic branches of, respectively, graphite and bilayer graphene with those of the single layer graphene. Fig. 2.9,

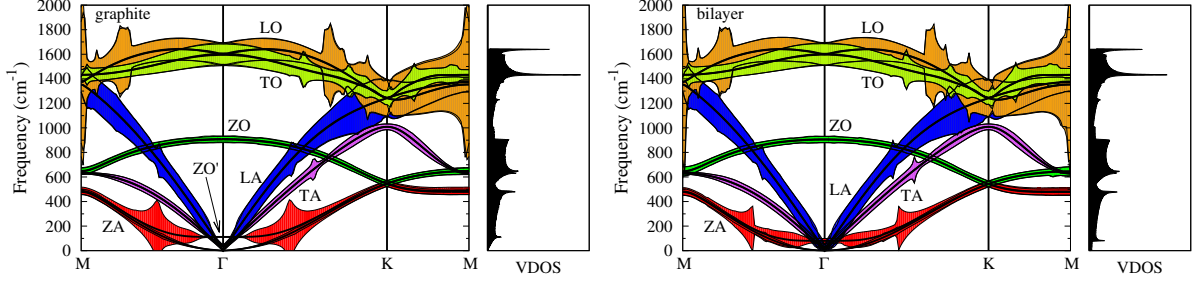


Figure 2.7: Graphite and graphene bilayer: calculated phonon dispersion widened by the anharmonic broadening ( $\text{FWHM} \times 100$ ) at 300 K. The Optical bands are LO, TO and ZO, the acoustic bands LA, TA and ZA. The quasi-acoustic bands are almost degenerate with the acoustic bands, but they cross Gamma with a small non-vanishing energy ( $\approx 110 \text{ cm}^{-1}$  for ZO').

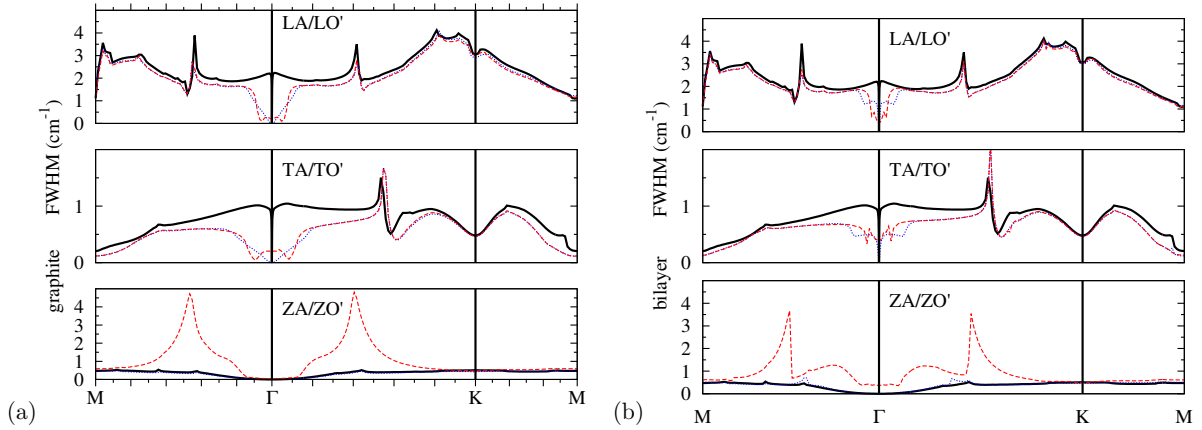


Figure 2.8: Anharmonic phonon broadening (FWHM) at 300 K. Graphene acoustic branches (solid line) are compared with the corresponding graphite (left panels) and bi-layer (right panels) acoustical (dotted) and quasi-acoustical (dashed) ones. It is interesting to observe how the LA and LO', the TA and TO' have very similar lifetimes, while the quasi-acoustic ZO' band has a much shorter lifetime because of its decay probability toward ZA.

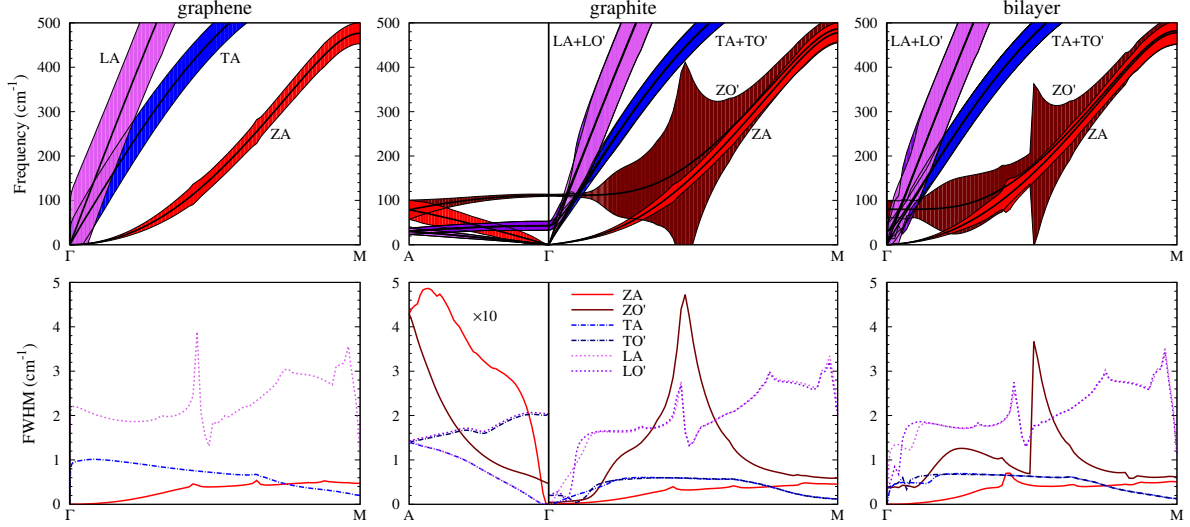


Figure 2.9: Phonon dispersion and anharmonic broadening of the acoustic and quasi-acoustic branches of graphene, graphite, and graphene bilayer. The upper panels show the lower part of the phonon dispersion as in Figs. 2.2 and 2.7. The lower panels show the FWHM at 300 K. The values in the A- $\Gamma$  section for graphite are magnified by a factor 10.

shows in more detail the low frequency region. In the high energy part of the spectrum, graphite and graphene monolayer and bilayer are almost undistinguishable, Fig. 2.7, meaning that the physics is ruled by the two dimensional character of the phonon dispersion also in graphite. Some of the graphene sharp features are a slightly broader in graphite due to the out-of-plane phonon dispersion acting like an effective smearing. The most striking differences between three-dimensional bulk graphite and two-dimensional graphene monolayer and bilayer are associated with the acoustic and quasi-acoustic branches.

First, we remind that, in graphene, the vibrational density of states (VDOS in Fig. 2.2) has a finite constant value for energies approaching zero. This is because the ZA branch has a quadratic dispersion (not linear as usual) and the VDOS is calculated in a two dimensional Brillouin zone. On the contrary, in graphite, the VDOS goes to zero almost linearly for energies going to zero, Fig. 2.7. This happens in spite of the fact that in graphite, when the out-of-plane component  $q_z = 0$ , the ZA branch is not very different from the graphene one. In particular, on the scale of Fig. 2.7, the graphite ZA branch (for  $q_z = 0$ ) appears quadratic as the graphene one from Fig. 2.2. Indeed, for graphite, the VDOS is calculated in a three dimensional BZ and the  $q_z = 0$  phonons have an infinitesimal weight. Also, notice in the graphite VDOS, the presence of a peak at  $132 \text{ cm}^{-1}$  corresponding to the ZO' frequency at  $\Gamma$ . This peak and this phonon do not have a correspondence in graphene. Finally, from Fig. 2.7, the bilayer VDOS has a finite constant value for zero energy (as for the monolayer) and it also shows the ZO' peak at  $94 \text{ cm}^{-1}$  (as in graphite).

Let us consider the broadening of the LA and TA branches in Fig. 2.8a. As already said, in graphene, these broadening do not vanish for  $q \rightarrow 0$  and, for small  $q$ , they are relatively constant over a wide range of  $q$  values (*e.g.* for the LA mode we are considering the region with  $\mathbf{q} < 0.4\mathbf{M}$  and  $\mathbf{q} < 0.4\mathbf{K}$  in Fig. 2.8a). This, “plateau” is due to Normal scattering towards the ZA phonons and its characteristics stem from the fact that the ZA dispersion is quadratic and that the integration (the sum in Eq. 2.9) is done on a two dimensional Brillouin zone. On the contrary, for three dimensional graphite, the broadening of both LA and TA modes vanishes for  $q \rightarrow 0$ . It is remarkable, however, that the graphite broadening still presents a Normal scattering plateau, similar to the one of graphene, for sufficiently large  $q$ . This is particularly evident for the LA mode for  $\mathbf{q} > 0.2\mathbf{M}$  and  $\mathbf{q} > 0.2\mathbf{K}$  in Fig. 2.8a. The LA and TA broadening in bilayer graphene, Fig. 2.8b, are rather more similar to the graphite one than to the graphene ones, indicating that, for a higher number of layers, the broadening should rapidly converge to the bulk graphite one. Note that, graphene bilayer presents non-vanishing broadening of the TA and LA bands at  $\Gamma$ , its magnitude being about half for bilayer than for graphene.

Finally, let us consider the  $z$  polarized branches. The ZA broadening in graphite is similar to the graphene one. On the other hand, the ZO' broadening of graphite is much larger than the ZA one, in spite of the

fact that the  $ZO'$  and  $ZA$  branches are strictly related. Particularly striking is the sudden increase in the  $ZO'$  broadening for certain values of  $q$  in the vicinity of  $\Gamma$  (*e.g* for  $\mathbf{q} = 0.47\mathbf{M}$  along the  $\Gamma\mathbf{M}$  direction). This peak of the broadening is due to the decay of a  $ZO'$  phonon, having a finite wavevector  $\mathbf{q}$  into a  $ZA$  phonon near  $\mathbf{q}$  and a  $LO'$  (or  $TO'$ ) phonon near  $\Gamma$ . This kind of decay is possible only when the energy difference between the  $ZO'$  and the  $ZA$  is equal or smaller than the energy of the  $LO'$  and  $TO'$  at  $\Gamma$  (the  $LO'$  and  $TO'$  are degenerate at  $\Gamma$ ), see Fig. 2.9. This condition is verified only for  $\mathbf{q}$  sufficiently far from  $\Gamma$ . Thus, by increasing  $q$ , the sudden availability of this new decay channel produces the peak in the broadening. Finally, for the bilayer, the  $ZO'$  broadening presents a structure which is not fundamentally different from the one in graphite.

## 2.5 Conclusion of graphene and graphite

Interesting, the broadening of the high-energy optical branches is highly non-uniform and presents a series of sudden steps and spikes of various origin. At finite temperature, the two linearly dispersive acoustic branches  $TA$  and  $LA$  have non-zero broadening for  $q \rightarrow 0$  (this was already noticed in 24). This anomalous behavior is due to Normal scattering towards two  $ZA$  phonons (which are quadratically dispersive), for small  $q$ . The activation of the Umklapp scattering for sufficiently large  $q$  is associated with a sudden increase of the broadening at nearly half the Wigner Size cell. Also, we provide a set of expressions which can be used to fit the anharmonic scattering time and broadening for the acoustic phonon branches, which are the most relevant in thermal transport.

The broadening of graphite and bi-layer is, overall, very similar to the graphene one. The most remarkable feature is the broadening of the quasi acoustical  $ZO'$  branch, which is much larger and very different from the one of the strictly related  $ZA$  acoustic branch. On the other hand, the broadening of the  $TA$  and  $LA$  branches of graphite, displays a certain number of similarities with that of graphene mono and bi-layer, in spite of the different dimensionality of the systems.

We will compute in Section 3.2.1 the thermal conductivity of graphite and graphene and compare it with experimental data.

## 2.6 Phonon spectral function

So far we have assumed that  $\Gamma$  only depends on  $\mathbf{q}$  and on the phonon band, and that it is independent of the energy. This may however be false when the phonon linewidth becomes comparable with the energy separation of non-degenerate modes. However, this is not a deal breaker for our technique,  $\Pi_\mu^{\mathcal{H}B}(\mathbf{q}, \omega)$  self-energy we can simulate the phonon spectra function at an arbitrary  $\mathbf{q}$ -point, and without any assumption, according to the following expression [79]:

$$\sigma(\mathbf{q}, \omega) = \sum_{\mu} \frac{-2\hbar\Omega_{\mu}(\mathbf{q})\Im\Pi_{\mu}^{\mathcal{H}B}(\mathbf{q}, \omega)}{[\hbar^2\omega^2 - \hbar^2\Omega_{\mu}^2(\mathbf{q}) - 2\hbar\Omega_{\mu}(\mathbf{q})\Re\Pi_{\mu}^{\mathcal{H}B}(\mathbf{q}, \omega)]^2 + 4\hbar^2\omega_{\mu}^2(\mathbf{q})[\Im\Pi_{\mu}^{\mathcal{H}B}(\mathbf{q}, \omega)]^2}. \quad (2.17)$$

Substituting in Eq. (2.17)  $\Im\Pi_{\mu}^{\mathcal{H}B}(\mathbf{q}, \omega) \sim -\Gamma_{\mu}^{\text{ph-ph}}(\mathbf{q})$  and  $\Re\Pi_{\mu}^{\mathcal{H}B}(\mathbf{q}, \omega) \sim \Delta_{\mu}(\mathbf{q})$  the spectral function  $\sigma(\mathbf{q}, \omega)$  reduces to a combination of Lorentzian functions. This substitution is justified as long as the real part of the self-energy remains constant in the energy range defined by the phonon linewidth. Indeed, in most cases the measured INS spectra show Lorentzian line-shapes [79], as the experimental phonon frequency is determined by the position of the peak and the linewidth of the Lorentzian gives the experimental phonon linewidth.

We have applied this technique to Palladium Hydride in Ref. 48, here we reproduce some of the main results. In Fig. 2.10 and 2.11 we plot the spectral function  $\sigma(\mathbf{q}, \omega)$  for PdH, PdD and PdT at 80 and 295 K, keeping the full dependence on  $\omega$  of the self-energy. As it can be observed, while the acoustic phonon peaks in  $\sigma(\mathbf{q}, \omega)$  fulfill with the simple Lorentzian picture, the highest energy modes already at 80 K show shoulders in their peaks not expected *a priori*. The situation becomes more dramatic at high temperature, as  $\sigma(\mathbf{q}, \omega)$  shows very wide resonances with a non-Lorentzian peak at most  $\mathbf{q}$  points for the optical modes, sometimes even with satellite peaks. The reason for this is that the self-energy is not constant in the range defined by the big linewidth of the optical modes. Having satellite peaks can be very misleading for experimentalists, since they can be interpreted as structural phase transitions. However, as in the case of Palladium hydrides, secondary peaks emerge due to strong anharmonicity. A similar effect has been recently reported in PbTe [125, 126].

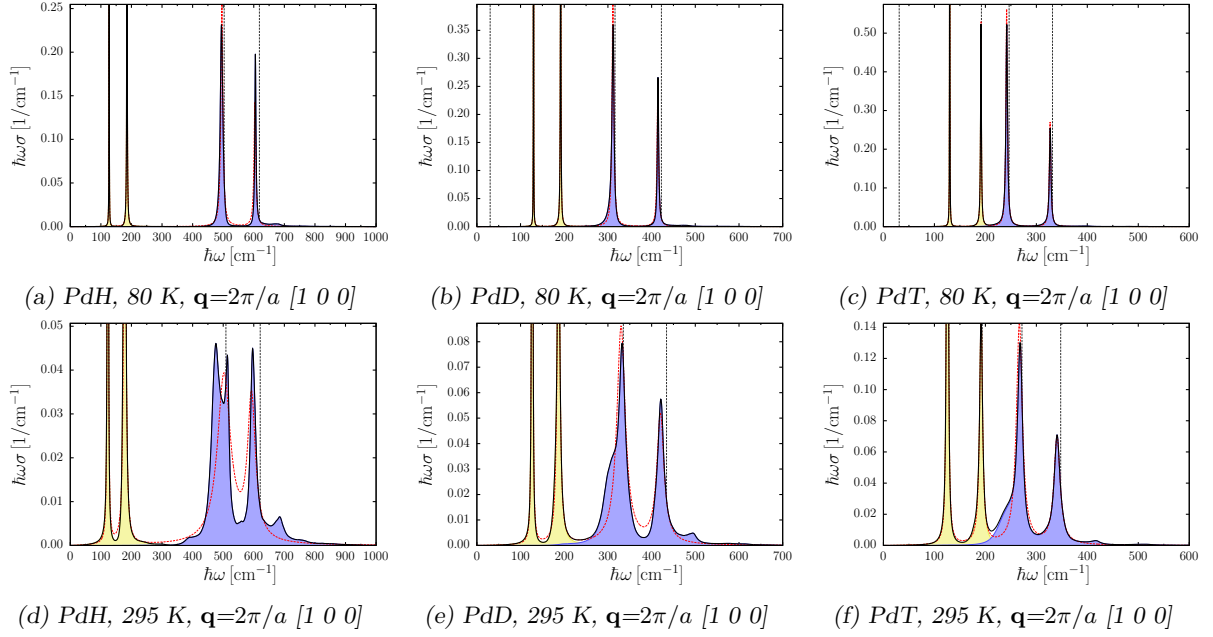


Figure 2.10: Spectra weight  $\hbar\omega\sigma(\mathbf{q},\omega)$  of Palladium hydrides at 80 and 295 K at the X point. The red dashed lines represent the curve obtained keeping the full dependence on  $\omega$  of the self-energy in Eq. (2.17), while the red dashed line is the Lorentzian line-shape obtained substituting in Eq. (2.17)  $\Im\text{m}\Pi_{\mu}^{\mathcal{H}B}(\mathbf{q},\omega) \sim -\Gamma_{\mu}^{\text{ph-ph}}(\mathbf{q})$  and  $\Re\text{e}\Pi_{\mu}^{\mathcal{H}B}(\mathbf{q},\omega) \sim \Delta_{\mu}(\mathbf{q})$ . The vertical black dashed lines denote the position of the SSCHA phonon frequencies.

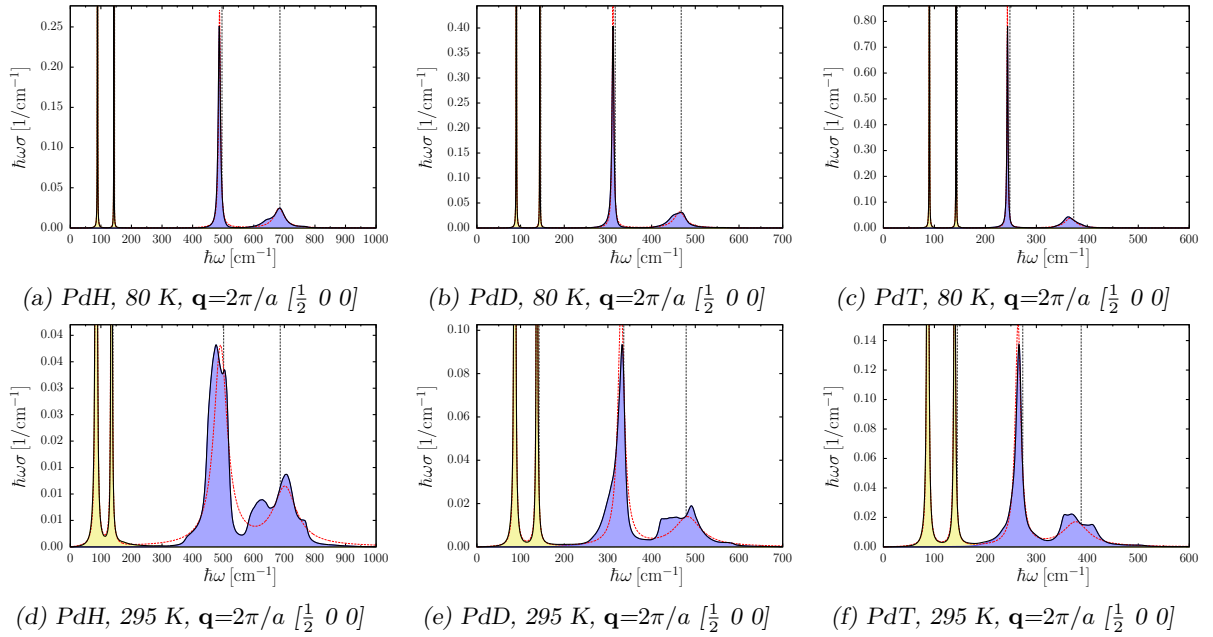


Figure 2.11: The same spectra as Figure 2.10 but for point  $\mathbf{q} = 2\pi/a[1/2, 0, 0]$ , where the strongest anharmonicity was observed.

More in detail, in Figures 2.10 and 2.11 we plot  $\hbar\omega\sigma(\mathbf{q},\omega)$  for the **X** point and  $\mathbf{q} = 2\pi/a[0.5, 0, 0]$ , respectively. We decided to plot  $\sigma(\mathbf{q},\omega)$  multiplied by  $\hbar\omega$  because the integral of this quantity over the entire energy domain gives the number of modes[127]. The curve obtained substituting in Eq. (2.17)  $\Im\Pi_{\mu}^{\mathcal{H}B}(\mathbf{q},\omega) \sim -\Gamma_{\mu}^{\text{ph-ph}}(\mathbf{q})$  and  $\Re\Pi_{\mu}^{\mathcal{H}B}(\mathbf{q},\omega) \sim \Delta_{\mu}(\mathbf{q})$  is also shown. It is clear from the figures that the latter approximation yields good spectral peaks for the Pd-character acoustic modes, but not for the H-character optical modes, specially at high temperature. For instance, at the X point at 295 K for PdH we observe that the peak associated to the lowest-energy optical mode is split into two distinct peaks and the highest-energy optical mode shows a satellite peak at high energy. The departure from the Lorentzian line-shape is less acute for the heavier isotopes. At  $\mathbf{q} = [0.5, 0, 0]2\pi/a$  on the contrary, the highest-energy optical peak appears with a complex line-shape with a double-peak structure for all the isotopes both at low and high temperature. We made the hypothesis that this complex line-shape is caused by the presence of two competing decay mechanisms; for example in the PdD case at the point  $bfq = [1/2 \ 0 \ 0]2\pi/a$  we have a strong peak around  $490 \text{ cm}^{-1}$  which is interestingly situated higher than the energy of the unperturbed SSCHA phonon eigenvalue ( $479.1 \text{ cm}^{-1}$ ). Another peak is situated present at a slightly lower energy, around  $450 \text{ cm}^{-1}$ . We decomposed the contribution to  $\Gamma(\mathbf{q},\omega)$  at this point and the energy of the two peaks, over the BZ. We found that the higher peak is caused by the activation of a decay channel toward two phonons on the lower optical band: one at X, the other at the Gamma point. This decay mechanism is forbidden at the energy of the lower peak, where the favourite decay mechanism is toward one optical and one acoustical phonon.

## 2.7 Attenuation of Hyper-acoustic waves in GaAs

In this section we present some result from Ref. 107: the application of *ab initio* methods to the calculation of hyperacoustic wave attenuation in large GaAs crystals. The comparison of calculation with experiments has allowed us to settle in a convincing way a debate about the origin of a “plateau” observed in the acoustic bands as a function of the phonon frequency. We showed that it is caused by the switch from a Herring to a Landau-Rumer regime. In simplified terms, from the sound wave scattering with a higher energy phonon to decays toward two lower energy phonons. On the contrary, the hypothesis of it being caused by the Akhiezer regime, *i.e.* collective scattering of the acoustic waves due to lattice elasticity, is disproved [128–131].

The attenuation of ultra-sound waves is related to the acoustic field amplitude by the following relation:

$$A_z(T) = A_0 e^{-\alpha(T)z}, \quad (2.18)$$

where  $A_z$  is the measured amplitude,  $A_0$  is the amplitude of the generated pulse,  $z$  is the distance from the pulse source and  $\alpha$  is the attenuation. The attenuation is inversely proportional to the phonon lifetime and its group velocity *i.e.*, to the derivative of the phonon frequency with respect to the wavevector,<sup>1</sup>  $\mathbf{v}_{\mathbf{q},j} = \nabla_{\mathbf{q}}\omega_{\mathbf{q},j}$ . The attenuation reads:

$$\alpha_{\mathbf{q},j} = \frac{1}{2|\mathbf{v}_{\mathbf{q},j}| \tau_{\mathbf{q},j}}. \quad (2.19)$$

We focus on the case for which we are able to directly compare experimental results and calculations: the longitudinal phonon branch along the [100] direction. As shown in figure 2.12a, the agreement is remarkable. Not only does the calculation correctly reproduce the qualitative behavior of  $\alpha(\omega)$ , and the presence of the plateau between 600 GHz and 1 THz, but also the experimental and calculated absolute values of the attenuation are very close. We stress that no renormalization has been applied to the data: the values of the attenuation directly come from the *ab initio* calculations.

In figure 2.12b, we examine the behavior of  $\alpha$  at the fixed frequency value of 713 GHz, as a function of the temperature, and compare it with the experimental data. The low-temperature region is magnified in the inset of figure 2. The agreement between the *ab initio* calculations and the experimental data (starting from 20 K) is strikingly good even at very low temperature. We report as supplementary materials the comparison for eight different frequencies, with similar conclusions.

<sup>1</sup>This derivative has to be done with some care, to avoid problems when phonon branches cross or are degenerate. Details can be found in section IV of Ref. 132.

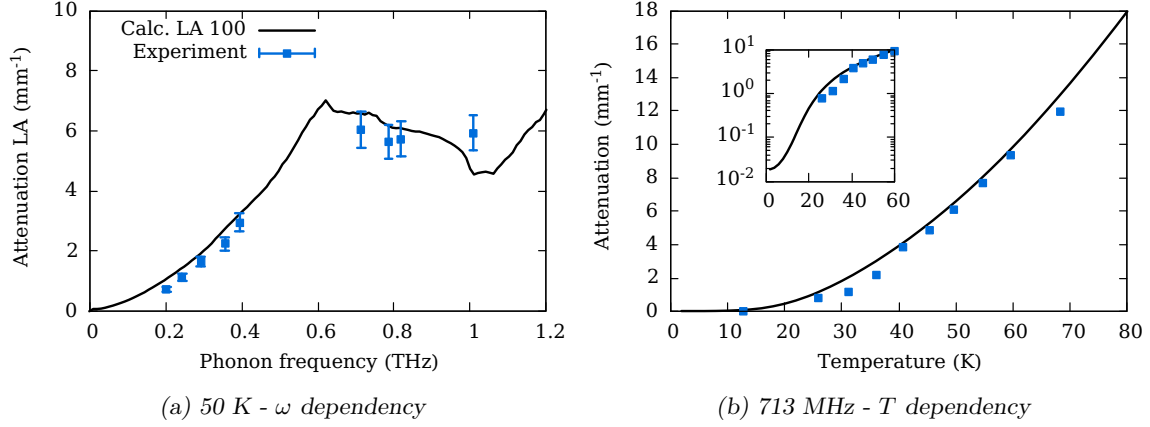


Figure 2.12: Phonon attenuation in GaAs: comparison of calculations with experiments (a) At fixed temperature (50 K) as a function of phonon frequency along the [100] direction. (b) At fixed energy ( $\omega = 713$  GHz) as a function of temperature. The inset shows data on a logarithmic scale for  $\alpha$  to magnify the low-temperature behavior. Similar pictures for all of the points measured in Ref. 131 are provided as supplementary materials of Ref. 107

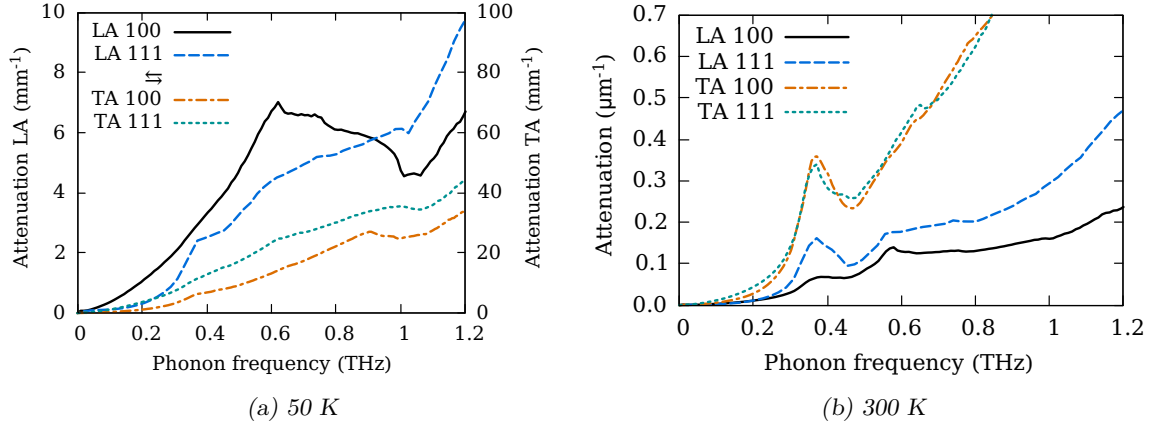


Figure 2.13: GaAs. Attenuation of longitudinal and transverse phonons along the [100] and [111] directions at 50 K (left panel) and 300 K (right panel). Note the change of scale between the two temperatures (panels), as well as the different axis for the TA mode (on the right) in the left panel.

At this point it is important to note that the experimental data correspond only to the relative change of attenuation with temperature defined by:

$$\alpha(T) - \alpha(10 \text{ K}) = -\frac{1}{z} \ln\left(\frac{A_z(T)}{A_z(10 \text{ K})}\right), \quad (2.20)$$

where  $A_z$  is defined in Equation 2.18, while the *ab initio* data is the absolute value of the attenuation given by Equation 2.19.

Thus, the experimental points would eventually go exactly to zero, at zero temperature, while the theoretical data, which take into account spontaneous decay processes, have therefore a finite limit at 0 K. The extremely good agreement above approximately 30 K implies that, indeed, the experimental points can also be considered as absolute values of the sound attenuation. The behavior of the *ab initio* data displayed in figure 2.12b is typical of what could be expected from the temperature dependence of the inverse lifetime: a slow growth starting from a finite value at low temperature, which eventually becomes linear, in this case above 90 K (not shown).

# Chapter 3

## Thermal conductivity

In this chapter we will review the theory of thermal transport in the Single Mode Approximation (SMA) with a particular attention to the so-called “extrinsic” scattering sources, i.e. sources other than the “intrinsic” phonon-phonon scattering, which we have seen in chapter 2. The code developed by the author (see appendix D) also includes more advanced techniques than SMA: the exact solution of the Boltzmann transport equation and the inclusion of off-diagonal terms required for the generalized theory of thermal conductivity in crystals and glasses as developed for reference 32. However for the scope of this work we will focus on the treatment of boundary and disorder effects.

*Results in this chapter are adapted from Ref. 133 and Ref. 25. More details about the ab initio calculations are available in the original research papers.*

### 3.1 Treatment of finite samples

#### 3.1.1 Scattering mechanisms in finite crystals

The behaviour of lattice-driven thermal conductivity as a function of temperature has a typical shape which is mostly independent of the material : at high temperature it decreases as  $1/T$ , at lower temperature it has a maximum, then going towards zero temperature it decreases sharply to a finite value. The behavior of the lattice thermal conductivity at high temperature is determined by the anharmonic phonon-phonon interactions [134] with a contribution from defects. In the low temperature regime, named after Casimir who studied it in the 1930’s [135], thermal conductivity is not a bulk property but it depends on the sample finite size [135].

Theoretical studies of the Casimir regime pre-date the possibility to study thermal conductivity by numerically integrating the phonon anharmonic properties [6, 135, 136]. The standard approach consists in modeling the sample boundaries as black bodies that absorb a fraction of the colliding phonons, reflect the rest, and emit phonons to maintain thermal equilibrium. These works use geometric calculations, valid in the linear regime where only the acoustic phonons are taken into account, to predict the low-temperature thermal conductivity, usually with a single free parameter: the surface reflectivity. Invariably they assume a simple geometry for the crystal, such as a long cylinder or a long square parallelepiped with a temperature gradient between its opposite faces; in a shorter cylinder with polished faces the model requires the inclusion of multiple internal reflections [136].

With the arrival of more powerful numerical techniques, it has become more effective to model the surface at the phonon level, as a scattering probability. The probability of scattering from the boundaries can be combined with the probability of scattering due to phonon-phonon interaction in accordance with Matthiessen’s rule [16]. This approach has been used in more recent literature [15] while keeping the assumptions of the long cylindrical geometry, not appropriate for application to thin films, where a temperature gradient can be applied orthogonally to the film lateral extension.

In Fig. 3.1 we have schematically depicted the possible scattering events responsible for limiting lattice-driven energy flow, we will briefly review them but for detailed discussion we redirect the reader to Ref. 132. Mechanisms (1) and (2) are the intrinsic scattering processes: (1) is the “normal” (N) scattering,

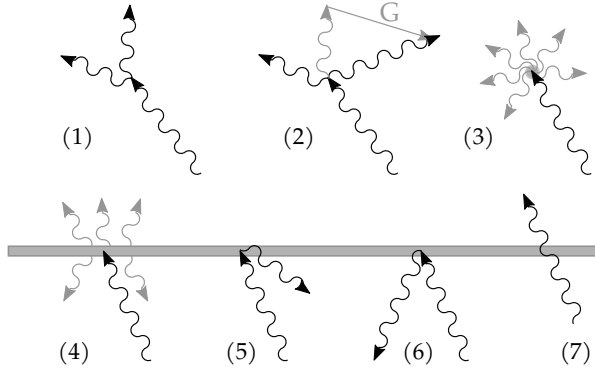


Figure 3.1: Possible scattering mechanisms in a slab-shaped crystal. 1) Normal momentum-conserving scattering (does not limit thermal transport). 2) Umklapp scattering. Absorption by: 3) point defects or isotopic disorder, or 4) rough “black” surface, with black-body emission to maintain thermal equilibrium. 5) Reflection by a rough “white” surface. 6) Reflection by a smooth surface. 7) Transmission through an intercalated surface.

it conserves momentum and does not limit thermal conductivity. N scattering is only important at very low temperature (a few K). (2) The *umklapp* (U) processes, that conserves crystal momentum modulus the addition of a reciprocal lattice vector, are the main limiting factor at high temperature and the prevalent intrinsic scattering mechanism. When studying thermal conductivity in the single-mode relaxation-time approximation (SMA), it is assumed that U scattering is dominant and that the scattered phonons are thermalized, i.e. that on average they are scattered toward the equilibrium thermal distribution. This approximation is very robust and works to within a few percent in a large range of temperatures and materials [74].

Diagram number (3) depicts the Rayleigh scattering with a point defect, which could be a vacancy [14], a substitutional defect or isotopic disorder [16]. Finally, events (4), (5) (6) and (7) are possible interactions between a phonon and the sample boundary: (4) is adsorption and re-emission by the surface; (5) is inelastic reflection by a “white” surface. We remark that, as it has been shown in Ref. 136, events (4) and (5) are equivalent from a thermal-transport point of view, we will just use (4) from here on. Further on, (6) is elastic reflection, where the momentum component parallel to the surface is conserved but the orthogonal component is inverted. Reflections can limit thermal conductivity in the direction orthogonal to the surface. Finally, in (7) a phonon can cross the boundary without scattering, this is of course not possible if the sample is suspended in vacuum, but can be the case if the sample is composed by multiple mis-matched segments, or if it contains stacking defects.

In order to describe the interface, we introduce three dimensionless parameters: the absorption fraction  $f_a$ , the reflection fraction  $f_r$  and the transmission  $f_t$ , these are the probabilities that a phonon will undergo process (4), (6) or (7) respectively when it collides with the boundary. The condition  $f_a + f_r + f_t = 1$  holds. In general these parameters may depend on phonon energy and its incidence angle, they can be computed using molecular dynamics techniques [137]. A special limit case is a very rough surface for which  $f_a = 1$ .

### 3.1.2 Thermal transport in the single-mode approximation

In the single mode approximation (SMA) the thermal conductivity matrix is:

$$\kappa_{\alpha\beta} = \frac{\hbar^2}{N_0\Omega k_B T^2} \sum_j v_{\alpha,j} v_{\beta,j} \omega_j^2 n_j (n_j + 1) \tau_j \quad (3.1)$$

Where  $j$  is a composite index running over the phonon wavevectors  $\mathbf{q}$  in reciprocal space and the phonon bands  $\nu$ ;  $N_0$  are the number of  $\mathbf{q}$ -points used to sample the Brillouin zone,  $\Omega$  is the unit-cell volume,  $k_B$  is the Boltzmann constant and  $T$  is temperature. Inside the sum, the composite index  $j$  stands for the band index  $\nu$  and the wavevector  $\mathbf{q}$ ; then  $\omega_j = \omega_\nu(\mathbf{q})$  is the phonon frequency,  $v_j = \nabla_{\mathbf{q}}\omega_\nu(\mathbf{q})$  is the phonon group velocity;  $\alpha$  and  $\beta$  are cartesian directions ( $x, y, z$ )  $n_j = n(\omega_\nu(\mathbf{q}))$  is the Bose-Einstein distribution and  $\tau_j$  is the phonon relaxation time, or inverse full-width half-maximum [25].

### 3.1.3 Thermal transport in thin film crystals

In order to progress further we have to take into account the real geometry of our sample. In this chapter we will consider two cases: (i) a thin film of thickness  $L$  along direction  $z$  and virtually infinite in the other two directions with two very rough opposing surfaces; (ii) bulk material intercalated with partial planes of one element, or stacking defects, which is a common kind of crystal defect [138, 139], at an average distance  $L$ .

In case (i) we consider a phonon emitted from a surface that moves toward the opposite surface with a  $z$  component of its group velocity  $v_z$ . After a time  $L/v_z$ , the phonon will reach the other surface and be absorbed with probability  $f_a$ , giving the first phonon scattering rate  $\gamma_a^{(1)}$  and the relaxation time  $(\tau_a^{(0)})^{-1} = f_a \frac{v_z}{L}$ . If it is not absorbed (probability  $f_r = 1 - f_a$ ), the phonon will be reflected back toward the initial surface with identical speed and it will undergo a second absorption/reflection process. The probability of a third reflection is  $f_r^2$ , for the  $n$ th reflection is  $f_r^{(n-1)}$ . After summing the geometric series, the total effective lifetime is:

$$(\tau_a)^{-1} = 2\gamma_a = f_a \frac{v_z}{L} \sum_{i=1, n} f_r^{i-1} = \frac{v_z}{L} \left( \frac{f_a}{1 - f_r} \right). \quad (3.2)$$

For boundary scattering,  $f_a = 1 - f_r$  conveniently cancels out giving  $\tau_a = \frac{L}{v_z}$ , but we prefer to leave eq. 3.2 in a general form to consider more general cases. Furthermore, if a phonon is reflected, its velocity component that is orthogonal to the surface will be inverted. We can account for this possibility in eq. 3.1 renormalizing  $v_z$  in the following way: a fraction  $f_r$  of the phonons will change the sign of  $v_z$ , a fraction of them will hit the opposite boundary, be reflected a second time and change sign again, and so on. The material is traversed in a “flying” time  $\tau_f = L/v_z$ . During this time phonons are scattered at a rate  $P_x = \tau/\tau_f$ , resetting the process. With  $\tau$  being its total (intrinsic and extrinsic) relaxation time. This can be expressed as:

$$\tilde{v}_z = \sum_{i=0, \infty} \left( -\frac{\tau_f}{\tau} f_r \right)^i v_z = v_z \left( 1 + \frac{\tau}{\tau_f} f_r \right)^{-1}. \quad (3.3)$$

Again, we do not replace  $\tau_f$  with  $1 - \tau_a$  because we want to keep this equation as general as possible.

In case (ii), a bulk material intercalated with planes, the reasoning is very similar, with the caveat that  $1 - f_a = f_r + f_t$ , although for an atom-thin intercalated layer we can safely assume that  $f_r$  is almost zero.

The final formula for  $\kappa$  becomes:

$$\kappa_{\alpha\beta} = \frac{\hbar^2}{N_0 \Omega k_B T^2} \sum_j \tilde{v}_{\alpha,j} \tilde{v}_{\beta,j} \omega_j^2 n_j (n_j + 1) \tau_j^{tot} \quad (3.4)$$

With  $\tilde{v}$  from eq. 3.3, and  $\tau$  comprises all the scattering terms, summed with the Matthiessen’s rule:

$$\tau^{tot} = \left( \tau_{ph-ph}^{-1} + \tau_a^{-1} + \dots \right)^{-1} \quad (3.5)$$

where additional scattering terms like point-defect scattering, can be added.

## 3.2 Applications

We report in the next sections a few examples of published applications. These examples highlight some specific difficulties of treating pathological materials: the non-linear acoustic band present in Graphene and the high amount of doping and semi-ordered defects in  $\text{Bi}_2\text{Se}_3$ .

### 3.2.1 Graphene and graphite

The intrinsic anharmonic thermal conductivity  $\kappa_L$  has been computed within the single mode time relaxation approximation using Eq. 2.10. For the two dimensional materials (graphene monolayer and

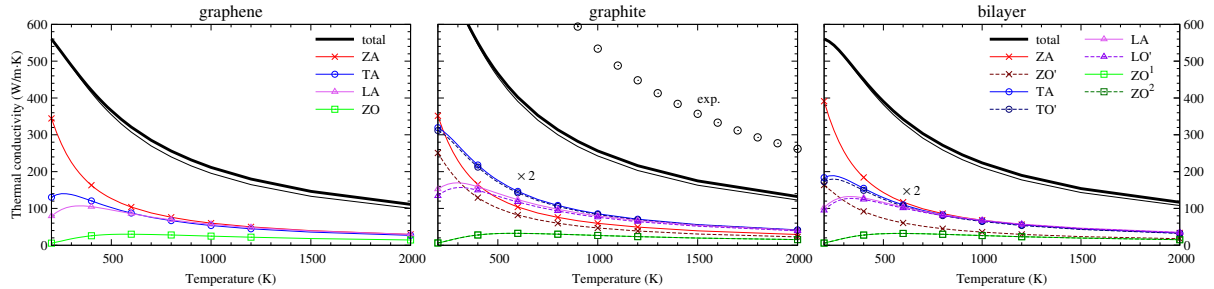


Figure 3.2: In-plane thermal conductivity obtained within SMA (thick solid line) and its decomposition into the contributions due to different phonon branches. The figure shows only the contributions from a subset of the most relevant phonon branches. The sum of these partial contributions is the thin solid line near to the total conductivity. In order to compare more easily the curves, the single branch contributions of graphite and bilayer are scaled by a factor 2. Dots are experimental data from 140.

bilayer) we have used the convention that the volume  $\Omega$  in Eq. 2.10 is the surface planar unit cell multiplied by the inter-layer distance of graphite, 3.32 Å. Fig. 3.2 reports the thermal conductivity and its decomposition into different branch contributions. In the temperature range considered, the conductivity is almost entirely due to the acoustic and the quasi-acoustic branches. Calculations of Fig. 3.2 are done for  $T > 200$  K. Below that temperature, converged results can be obtained only by using a much finer q-points grid than those presently used.

Let us, first, consider graphene. From Fig. 3.2, the ZA contribution increases by decreasing the temperature (actually, it diverges for  $T \rightarrow 0$ ), while the LA and TA contributions are non monotonic and reach a maximum near 300 K. The difference in the two behaviors can be understood by considering that, for small  $T$ , the phonons mostly occupied have small  $q$ , and that, for  $q \rightarrow 0$ , the anharmonic broadening (the inverse of the  $\tau$  appearing on the r.h.s of Eq. 2.10) of the ZA mode goes to zero at any  $T$ . This is not the case for the broadening of the TA and LA branches, Fig. 2.3. Now, let us compare in Fig. 3.2 graphene with graphite. The ZA contribution in graphene corresponds, in graphite, to the two separate contributions ZA and ZO'. These two are quite different already at room temperature. Below room temperature, the ZA increases and diverges for  $T \rightarrow 0$  (as for the ZA in graphene), while the ZO' does not. The TA contribution in graphene corresponds, in graphite, to the TA and TO' ones. Above 200 K, the TA and TO' contributions are almost indistinguishable, in spite of the fact that only the TA branch is actually acoustical. Important differences between TA and TO' contributions appear only below 50 K (not shown). The same considerations hold for the LA LO' couple. By comparing in Fig. 3.2 graphite with the bilayer, above 200 K, the overall behavior of the two systems is relatively similar, in spite of the different dimensionality. Indeed, in the same temperature range, the total conductivity of two dimensional graphene mono- and bi-layer and that of three dimensional graphite are relatively very similar, Fig. 3.3, with a difference between graphene and graphite of less than 10%.

Fig. 3.2 also reports the measured in-plane thermal conductivity. This is done only for bulk graphite, because of the abundance of experimental data. At present, experimental measurements on graphene are lacking and contradictory. From Fig. 3.2, the calculated graphite conductivity (which is obtained within the SMA) grossly underestimates the measured one, by about a factor two. It is unlikely that this disagreement is due to density functional theory. Indeed, DFT reproduces very well the measured graphite phonon dispersions, Fig. 2.1, suggesting that the most important quantities used in Eq. 2.10 are correct. On the other hand, as already explained at the end of Sec. 2.3, the thermal conductivity calculated according to Eq. 2.10 derives from the single mode relaxation time approximation and not from an exact solution of the transport equation. Indeed, according to Refs. 141, 142, the SMA cannot be used to properly describe the in-plane thermal conductivity in graphitic materials and the exact solution of their Boltzmann transport equation is required. However, the results of Refs. 141, 142 are obtained by using a semiempirical interatomic potential and a direct comparison with the present results is not meaningful. Further investigation on this point is required.

We now consider the thermal conductivity along the  $z$  axis, perpendicular to the graphene planes. Fig. 3.3 shows calculations and compares them with measurements. The quasi totality of the conduction is due to the acoustic and quasi-acoustic phonons polarized along  $z$  and, as expected, the conduction is much smaller than the in-plane one. The transport in-plane and the one along  $z$  are quite different. The

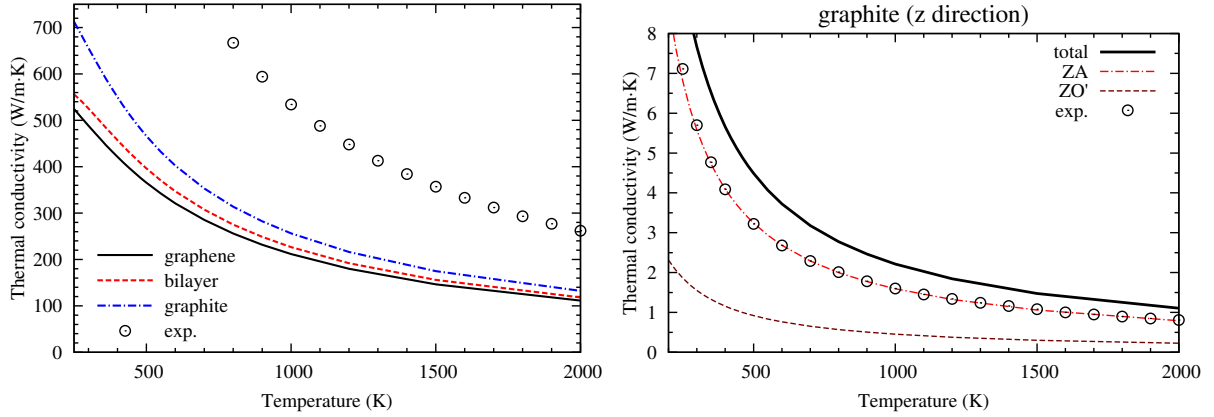


Figure 3.3: (Left) In-plane thermal conductivity calculated within the SMA for for graphene single and bilayer and bulk graphite. (Right) Thermal conductivity of graphite along the direction orthogonal to the planes, and its decomposition into the contributions given by different phonon branches. Measurements (exp.) are from 140 and should be compared with the line labeled as “total”.

phonons relevant for the  $z$  conduction are much more localized and have much smaller velocity. Indeed, only phonons with a non-zero dispersion along the  $z$ -axis can conduct since they have a non-zero velocity and, thus, can give a contribution to the sum in Eq. 2.10. These phonons belong a small region around the  $\Gamma$ - $A$  line. We also remark that the  $z$  conduction is extremely sensitive to the value of the  $c/a$  lattice parameter. Indeed, a small change in  $c/a$  results in a systematic increase or decrease of the frequencies of all the phonons relevant for the transport along  $z$ , see Fig. 2.1. Moreover, a systematic rescale of phonon frequencies by a certain factor  $\lambda$  results in a rescale of the conduction by a factor which can be much bigger than the initial  $\lambda$  (see Eq. 2.10). The agreement with measurements from Fig. 3.3 is, thus, satisfactory and we judge it compatible with the assumption that the SMA correctly describes the thermal transport along the  $z$  axis.

### 3.2.2 Bulk $\text{Bi}_2\text{Se}_3$

An important application of *ab initio* thermal conductivity is thermoelectricity. In particular, having an insight at the nanoscale on the interaction between phonons and finite sample dimensions can guide the development of more nano-structured materials with a higher thermoelectric efficiency. In this section, we present a study of thermal conductivity in  $\text{Bi}_2\text{Se}_3$ , where the use of *ab initio* simulation allowed us to characterize the prevalent type of crystal defect found in the bulk structure, and to predict, to some extent, the reduction of thermal conductivity observed in nano-slabs of 20-100 nm thickness.

More detail about these calculations are available in Ref. 133.

We have initially studied the phonon-driven thermal conductivity in the bulk phase as experimental data is available with good precision in a wide range of temperature. In particular we have taken as reference the data of Navratil and coworkers [143], where they estimate the fraction of lattice-driven and electron-driven transport.

In Fig. 3.4 we plot the experimental data of the in-plane thermal conductivity  $\kappa_{\parallel}$  measured in Ref. 143, side by side with calculations from 2 K up to 400 K, in the RTA (we checked that the exact inversion of the Boltzmann transport equation yield practically identical values). As it can be seen, the room temperature behaviour of the lattice contribution to  $\kappa_{\parallel}$  is in perfect agreement with our calculation of the intrinsic thermal conductivity. This agreement is possible thanks to the inclusion of lattice defects in the model, as explained in the rest of this section.

Below 20 K,  $\kappa_{\parallel}$  is limited by extrinsic scattering processes such as the scattering with sample borders, with the isotopes or/and with lattice defects. As Navratil *et al.* used a large mono-crystal, and isotopical effects are negligibles in  $\text{Bi}_2\text{Se}_3$ ,<sup>1</sup> only lattice defects can explain the low temperature behaviour.

According to literature [139], two kind of defects are common in  $\text{Bi}_2\text{Se}_3$  crystals: point-defect vacancies

<sup>1</sup>The relative mass variance of Selenium isotopes is only 0.046%, while Bismuth has only one stable isotope

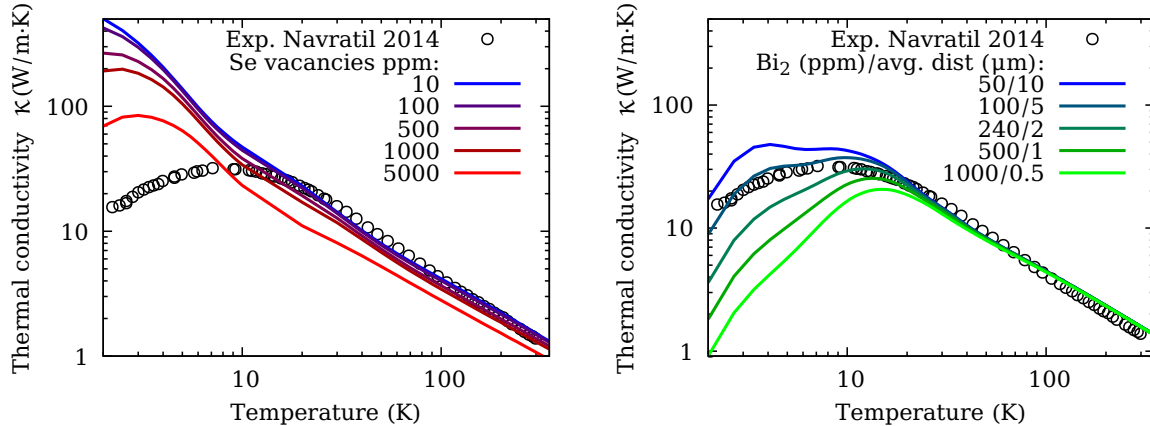


Figure 3.4: In-plane (i.e. orthogonal to  $c$  axis)  $\kappa$  measured by Navratil [143] (rounds) compared to simulations including the effect of Se vacancies (left) and  $\text{Bi}_2$  layers intercalations (right) defects on  $\kappa$ , excess  $\text{Bi}_2$  is expressed as average inter-plane distance and as ppm. The behavior at very low temperature (i.e. below 2 K) is not shown as it could suffer from the finite  $k$ -point mesh used in the calculations, due to the difficulty of converging the conductivity in the zero temperature limit

of Se, and  $\text{Bi}_2$  partial-layer intercalation. Each Selenium vacancy contributes around two charges to the total doping, which means that at a doping concentration of around  $10^{18} - 10^{19} \text{ e/cm}^3$  the fraction of missing Se atoms is of order 100 – 1000 ppm. We have simulated this defect concentration using a Rayleigh point-scattering model, assigning to each vacancy an effective mass as in Ref. 14. We found that this kind of defect scattering is too weak to explain the low-temperature drop in thermal conductivity. Even taking an unrealistically high point-defect concentration, such as 50 000 ppm (5%), the correct curve shape at low temperature is not reproduced. Finally, we remark that using a more accurate, i.e. *ab initio*, estimate of the defect cross-section would be equivalent to a change in defect concentration, but would not change the shape of the curve.

On the other hand, if we assume the presence of  $\text{Bi}_2$  partial layers, we can include it in the simulation using Sparavigna-Casimir scattering theory, i.e. using an effective model that includes a scattering time which is proportional to the ratio between the phonon mean free path and the sample size. We tuned the average inter-defect distance to fit the temperature of maximum  $\kappa$ , around 10 K. The theoretical position of the maximum is a better fitting parameter than its absolute value, as the latter is very difficult to converge at low temperature in simulations. Notwithstanding that, the calculation reproduces the absolute value quite well, which strengthens the validity of our assumption. In Fig 3.5, the best agreement is found when the average distance between  $\text{Bi}_2$  planes is fixed at  $5 \mu\text{m}$ . Comparing this value to the size of the unit cell along  $c$  gives a concentration of excess Bismuth of around 100 ppm, and considering that each additional Bi atom provides three charges, this is compatible with the measured doping concentration.

We note that the effect of Selenium vacancies and Bismuth partial layer intercalation is qualitatively different: a increasing concentration of Selenium vacancies causes a global reduction of  $\kappa$ , on the other hand increasing the frequency of Bismuth partial layer intercalation moves the maximum of  $\kappa$  toward higher temperatures, without changing its high-T value. If we combine the two types of defects, we observe that Selenium vacancies have virtually no effect until their concentration is greater than 100ppm, after which scattering from vacancies lead to a considerable reduction in  $\kappa$  at higher T. As a consequence, the best match remains a concentration of around 100 ppm Bismuth partial layer intercalation with 100 ppm or less Selenium vacancy. This is compatible with the high n-type concentration ( $\simeq 10^{19} \text{ cm}^{-3}$ ) of the bulk material measured.

### 3.2.3 $\text{Bi}_2\text{Se}_3$ thin films

Thermoreflectance measurements provide the total out-of-plane ( $\kappa_{\perp}$ ) thermal conductivity which is the sum of the electronic and lattice contributions. The lattice contribution has been estimated after measuring the in-plane electronic conductivity in thin films and estimating the out-of-plane electronic con-

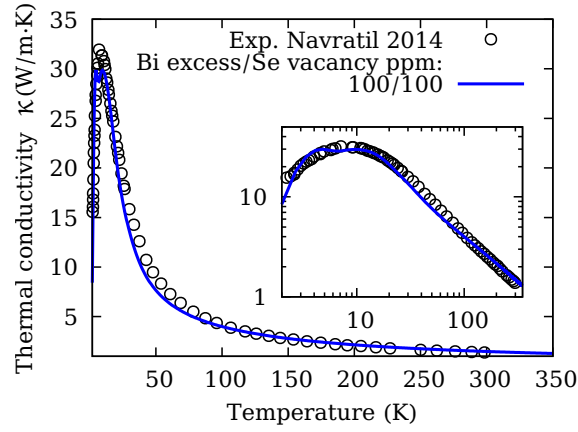


Figure 3.5: Best description of the thermal conductivity with Ref. 143 is obtained assuming around 100 ppm of  $\text{Bi}_2$  partial layers and 100 ppm of Selenium vacancies.

Thickness (nm)	Thermal conductivity:	
	Total (measured) (W/m·K)	Lattice (estimated) (W/m·K)
18	0.39	0.19
30	0.52	0.32
53	0.53	0.33
105	0.56	0.36
191	0.68	0.48

Table 3.1: Out-of-plane thermal conductivity of  $\text{Bi}_2\text{Se}_3$ , the experimental error bar can be evaluated to 20%.

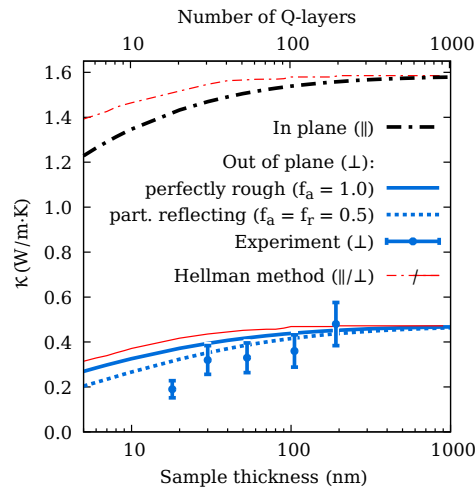


Figure 3.6: Thermal conductivity in thin films of  $\text{Bi}_2\text{Se}_3$  as a function of sample thickness  $L$  at 300 K. Experimental data: lattice thermal conductivity, to be compared with  $\kappa$  out-of-plane axis (dashed line). Blue thick line use our theory of Casimir scattering, while red lines use the method of cutting-off phonons of Ref. 144.

ductivity from the measured conductance anisotropy of bulk  $\text{Bi}_2\text{Se}_3$ , as studied in detail in 133.

Transport measurements performed attest that our thin films are  $n$  doped and present a metallic behavior with a carrier's concentration bracketed by  $1 - 2 \times 10^{19} \text{ cm}^{-3}$ ,  $\mu \sim 300 - 400 \text{ cm}^2/\text{V}\cdot\text{s}$  and  $\rho_{\parallel} \sim 1 - 1.15 \text{ m}\Omega\cdot\text{cm}$  at room temperature.

Thus a coarse evaluation of the electronic contribution to the in-plane conductivity  $k_{el,\parallel}$  can be given using the Wiedmann-Franz law  $k_{el,\parallel} = LT/\rho_{\parallel}$  with  $L$  the Lorentz number, ranging between 2 and  $2.2 \times 10^{-8} \text{ V}^2\text{K}^{-2}$ . Consequently  $k_{el,\parallel}$  is bracketed between  $0.4 - 0.7 \text{ W/m}\cdot\text{K}$ .

In table 3.1 we report the measured values for the total and lattice thermal conductivity, obtained by subtraction the estimated electronic contribution. In Fig. 3.6, we compare the measured lattice thermal conductivity with the simulations. The agreement is within the experimental errorbar. Including internal reflection effects (dashed line in the figure) does improve the agreement but is not sufficient to explain completely the discrepancy for the smallest slab. This may indicate that a simple Casimir model is not sufficient for such a thin sample, a more detailed description of the interaction of phonon with the surface, including  $\mathbf{q}$  and  $\omega$  dependence could improve the agreement. Finally, the laser penetration depth in the sample (around 10 nm) could play a role for the thinnest slabs, although there is no simple way to include it in the simulation.

We have also tested the approach of Ref. 144 (red lines of Fig. 3.6), which consists in cutting off completely the contribution of phonons that have mean free path  $\tau v$  larger than the sample dimension. The behaviour is relatively similar, but the predicted value of  $\kappa$  is considerably larger for the smaller samples.

## Chapter 4

# Beyond Perturbation Theory

The first motivation for developing beyond-harmonic methods for the description of phonons are crystal phases which are stabilized by temperature. These materials, have a higher symmetry phase, which can gain a bit of energy by breaking symmetry at low temperature. When the phonons free energy is sufficient to overcome the small energy gain the high symmetry phase can stabilize, although the curvature of the static electronic energy remains negative.

It is not possible to approach these systems with perturbation theory on top of the harmonic hamiltonian, as the trial ground-state is not stable. Non perturbative methods have been developed since the 1950s, initially by Born and Hooton [145, 146] and other groups all the way until the 2010s [42, 147, 148]. Initially based on semi-empirical potentials they are nowadays used in conjunction with DFT or, more recently, with classical force fields fitted on DFT, i.e. via machine learning.

These methods differ on how the potential energy surface (PES) is sampled and how the vibrational properties (harmonic force constants, frequencies or vibrational spectrum) are extracted from the calculations. Ab-initio molecular dynamics (MD) methods is a versatile, if not very efficient method, sample the fully anharmonic PES. From sufficiently long MD trajectories the phonons can be extracted using normal-mode analysis (NMA) [33, 149] or velocity autocorrelation function (VACF) method [34]. The efficiency of VACF can be improved projecting the atomic velocities on harmonic phonons modes from DFT in a commensurate unit cell [35]. Standard MD methods do not take into account quantum nuclear effect, which can be problematic for hydrogen atoms, and especially for hydrogen-based metallic materials which have been found to be record breaking superconductors. This limitation can be overcome using Path-Integral Molecular Dynamics, although at a larger computational cost, and suitable “quantum” position-position or force-force correlators [37, 38].

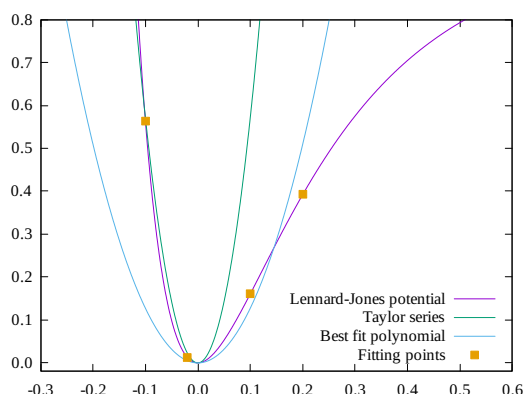


Figure 4.1: The Lennard-Jones potential approximated with its Taylor expansion around the minimum, or fitted with a second order polynomial over a large range of points. Which approximation is “better” depends on the range of application.

On the other hand, are the methods which sample the PES stochastically, which requires an approximated PES model to start the sampling. Some early examples are the self-consistent phonon (SCP) method and the Self-Consistent Ab-Initio Lattice Dynamics (SCAILD) by Souvatzis et al. [150], which assume the distribution of atomic displacement due to thermal rattling to be gaussian, i.e. harmonic. Roekeghem extended SCAILD to QSCAILD, which uses a quantum mean square thermal displacement matrix [39, 40].

Sticking with the harmonic sampling, but using a theoretical framework based on the ion displacements density matrix is the Stochastic Self-Consistent Harmonic Approximation (SSCHA) [41] which involves minimizing the phonon free energy capturing both nuclear quantum and anharmonic effects. Other SCP-based methods include SCPH proposed by Tadano et al. [42], where anharmonic frequencies are computed from the pole of the Green's function and higher order effective force constants from "compressive sensing" [151].

Temperature-dependent Effective Potential (TDEP) is a method of computing force constants (FCs) from *ab initio* MD forces that are "optimal" for a given temperature. This method was first proposed by Esfarjani and Stokes [43], where the FCs are extracted from *ab initio* MD force-displacement data. Hellman and coworkers [44, 45] apply a similar procedure, but starting instead with zero-temperature harmonic FCs and solve a least-square fit to obtain the FCs that minimize the difference between the "real" *ab initio* forces and the "harmonic" 2-body force computed from FCs. This convention minimizes the residual "anharmonic" force at the temperature imposed during the MD simulation. We have implemented a reciprocal-space version of this method, as detailed in Section 4.1

Details of these methods are in the original articles of the authors and also in recent reviews by Esfarjani et al. [152], and Hong et al. [153].

## 4.1 TDEP implementation

Our TDEP implementation reuses as much as possible the computational tools developed to compute the phonon linewidth and thermal conductivity. For this reason, and at variance with other available TDEP packages, it works mostly in reciprocal space, manipulating dynamical matrices, instead of using real-space force constants. The process is divided in three steps: (i) identify a minimum number of "phonon parameters" that are sufficient to describe the phonons for a given crystal over a grid of a given size; (ii) compute the "harmonic forces" from the 2-body force constants, (iii) Optimize the parameters to minimize the difference between the harmonic and fully *ab initio* forces.

### 4.1.1 Phonon parameters

In the following list, we give a simple schematic description of the algorithm to decompose the complete phonon dispersion in a very small number of independent minimal phonon parameter (MPP). This algorithm is similar to the one used in the SSCHA method [41]. It is a crucial part of the TDEP algorithm that each parameter to minimize spans a subspace which is orthogonal to all the others. Otherwise, the minimization algorithm, which considers the parameters to be independent, will not converge and overestimate its own precision. The procedure is presented in more detail in appendix B.5.

1. Symmetry analysis of the crystal:
  - find the symmetry of the lattice and crystal
  - construct a grid of  $N_{\mathbf{q}} = n_1 \times n_2 \times n_3$   $\mathbf{q}$ -points
  - find the  $N_w$  points that form an irreducible wedge of the Brillouin zone,  $N_w \leq N_{\mathbf{q}}$
2. Symmetry analysis for every  $\mathbf{q}$ -point in the wedge:
  - find the small group of symmetry of the point
  - construct a basis of  $N_p(\mathbf{q})$  symmetric orthonormal dynamical matrices  $B_i(\mathbf{q}), i = 1, N_p(\mathbf{q})$
  - iterate obtain a total of  $N_p = \sum_{i=1, N_w} N_P(\mathbf{q}_i)$  dynamical matrices that form a basis for all the points in the wedge and, via symmetry, of the entire grid.

With this basis we can decompose any dynamical matrix  $D(\mathbf{q}_j)$  which has the correct symmetry for any point in  $\mathbf{q}_j$  the wedge as

$$D(qq_j) = \sum_{i=1, N_p(qq_j)} \langle B_i(qq_j) | D(qq_j) \rangle B_i(qq_j) \quad (4.1)$$

Using symmetry, we can easily reconstruct the full dispersion from the irreducible wedge. The  $N_p$  parameters  $d_{i,j} = \langle B_i(qq_j) | D(qq_j) \rangle$  are the MPP, i.e. the minimum number of parameters required to represent any phonon dispersion respecting a given crystal symmetry on a certain grid. Equivalently, as shown in Section A.3, the MPP are sufficient to determine all the FCs up to given size of supercell, dual to the grid.

We will not go in detail on these points, the interested readers can find an very detailed description of the procedure in Appendix A and B. Table 4.1 shows the number of parameters required for different systems of increasing size (atoms per cell and supercell size) and decreasing symmetry.

### 4.1.2 Minimization and fitting

The natural choice is to minimize the difference between the real *ab initio* forces  $F^A$  and the harmonic forces  $F^H$  computed from the force constants. The  $\chi^2$  to minimize can be defined as a sum over all the coordinates, atoms in the supercell and the many configurations sampled.

$$\chi^2 = \frac{1}{N_s} \sum_{\alpha, I, i=1, N_s} |F_{\alpha, I}^A(R_i) - F_{\alpha, I}^H(R_i)|^2 \quad (4.2)$$

Where  $\alpha = x, y, z$  is a Cartesian coordinate,  $I$  is the number of the atom in the supercell and  $i$  the number of the step. When the sampling has a long correlation time, i.e. when using standard MD, it is necessary to only include only a fraction of the steps (i.e. one every  $M$ ) in the sum, otherwise the correlation will cause the algorithm to underestimate its own accuracy accuracy, i.e. to stop too soon during the minimization.

For generality, we could include a weight in the sum, keeping in mind that the sampling is optimal when all the weights are equal, but leaving the possibility open to operate a global re-weight in order, for example, to change the effective temperature of the sampling.

In practice, we have initially used the classic LMDIF method [154]. When LMDIF operates on the array  $\Delta \mathbf{F} = (\Delta F_{x,1,1}, \dots, \Delta F_{z, N_a, N_s})$  with  $\Delta F_{\alpha, I, i} = |F_{\alpha, I}^A(R_i) - F_{\alpha, I}^H(R_i)|$  it can use all the  $3 \times N_a \times N_s \times N_p$  derivatives together, this is much more powerful than having access to only  $\chi^2$  and its derivative with respect to the  $N_p$  parameters.

The Fortran77 library is efficient when used to minimize simultaneously  $M$  functions, in our case  $M = 3 \times N_{at} \times N_{steps}$  (number of atoms in the supercell, times number of dynamics steps) of  $N$  parameters, in our case  $N = N_{ph}$  (number of irreducibles phonons parameters, see Section 4.1.1). Even using a numerical estimate of the Laplacian, it is extremely efficient, converging in less than 10 iterations. However, it does not scale well for large problems. In larger systems, we can have upward of 1000 parameters, to be minimized over millions of data points. For this reason, we have moved to a parallel implementation (based on scalapack) developed ad hoc [155].

Table 4.1: Size dependence of phonon parameters for a 5,000 MD snapshots. Space group (SG), supercell size, number of atoms in supercell ( $N_{at}$ ), minimal phonon parameters ( $N_{ph}$ ), number of fitting points ( $M = N_{steps} \times 3 \times N_{at}$ ), and TDEP CPU time.

System	SG	Supercell	$N_{at}$	$N_{ph}$	$F_{AI}$	$N$ (s)
Al	<i>Fm3m 225</i>	$2 \times 2 \times 2$	8	4	$2.00 \times 10^5$	3
CsI	<i>Pm3m 221</i>	$2 \times 2 \times 2$	16	13	$1.20 \times 10^5$	9
Zr	<i>Im3m 229</i>	$4 \times 4 \times 4$	64	17	$9.60 \times 10^5$	3
SrTiO3	<i>Pm3m 221</i>	$2 \times 2 \times 2$	40	49	$6.00 \times 10^5$	42
MgO	<i>Fm3m 225</i>	$4 \times 4 \times 4$	128	51	$1.92 \times 10^6$	98
MgSiO3	<i>Pbnm 62</i>	$2 \times 1 \times 2$	80	994	$1.20 \times 10^6$	28152

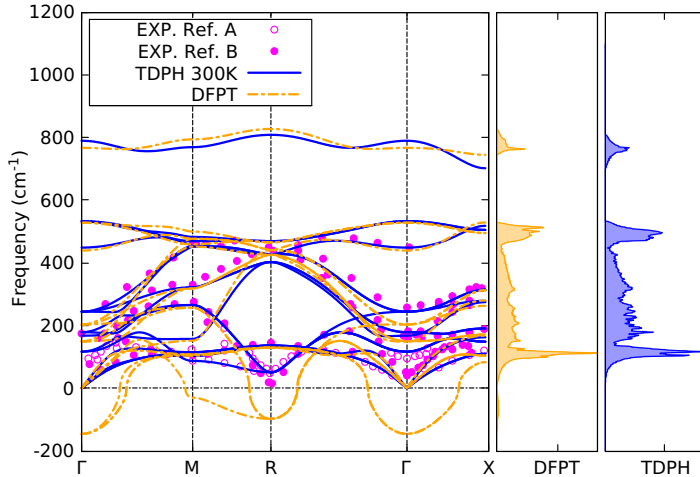


Figure 4.2: Comparison of “harmonic” phonons from DFPT and “anharmonic” phonon at 300K obtained via TDEP over and LD sampling in SrTiO<sub>3</sub>. The static DFT structure is unstable, but becomes stable at finite temperature. Ref. A and B are 158 and 159.

### 4.1.3 Choice of sampling method

A weakness of the TDEP method is that sampling the PES with NVE<sup>1</sup> *ab initio* molecular dynamics is very inefficient: because each step is derived from the previous ones following a deterministic equation of motion, subsequent steps are strongly correlated. Depending on the condition (temperature, symmetry, range of frequencies) tens or even hundreds of intermediate steps have to be skipped in order to have an un-correlated sample.

To avoid this problem, we have used the approach of Langevin dynamics (LD), which contrary to its name is more a Markov chain process than real dynamics. In LD, at each step the effective force acting on the atoms is composed of three terms: the *ab initio* force  $f_{ai}$  (including the Born-Oppenheimer force and Ion-Ion terms), a damping term  $-\gamma\mathbf{v}$  and a stochastic force with a given distribution  $\boldsymbol{\eta}_i$ .

$$\dot{\mathbf{p}}_i(t) = - \underbrace{\gamma\mathbf{p}_i(t)}_{\text{damping}} + \underbrace{\mathbf{f}_i(\mathbf{q}(t))}_{\text{ab initio}} + \underbrace{\sqrt{2m_i k_B T}\boldsymbol{\eta}_i(t)}_{\text{stochastic}} \quad (4.3)$$

The damping term ensures that correlation is exponentially decaying, while the stochastic force keeps the temperature constant. This procedure can be much more efficient than a classic Metropolis algorithm of try-test-discard because it exploits the distribution gradient (i.e. the force). We refer to literature for further justification [37, 47, 62, 156].

If integrated in a smart way [47] the equation of motion does not depend strongly on the value of  $\gamma$  and the correlation time can be as shorter than 5 time steps. Comparing the efficiency of the LD methods with standard NVE dynamics and hybrid approach which combines standard dynamics with and advanced stochastic thermostat (MD-SVR) [157] is the current work of a PhD student under my supervision [46].

As a textbook example, we show in Fig. 4.2 the difference between the “zero temperature” phonons in SrTiO<sub>3</sub>, obtained from a simple DFPT phonon calculation and the “finite temperature” phonons, from the same structure, but obtained with the TDEP procedure fit over a LD simulation performed at 300 K. The mechanical instability of the crystal is removed by temperature, and the phonon bands match very closely experimental results from literature.

<sup>1</sup>Constant number of particles, Volume and total energy

## 4.2 Perspectives

We have seen between Chapter 2.1 and 4 the subsequent developments of theory from harmonic crystal, to include perturbative anharmonicity, and to treatment of finite temperature via the simulation of the full lattice dynamics. These developments of the theory have allowed us to correctly reproduce the characteristics of phonon dispersions, from simple widening of the phonon lines in layered carbon materials (graphene, graphite), to interpreting the detail of sound waves attenuation in GaAs, to the peculiar behaviour of hydrogen ions dissolved in a Palladium matrix, and their strongly anharmonic vibrational spectra, including asymmetric and satellite peaks. We have also seen how the inclusion of anharmonic effects allow us to predict thermal transport properties, in simple materials and, with some additional assumptions, in complicated systems including disorder and finite size effects.

There are however, a heap of problems that are still unsolved, that are only solved under simplified assumption that do not allow a full *ab initio* treatment of the system, or that are solved on a per-case basis with a large amount of system-specific work. These constraints, do not allow high-throughput simulations nor application by less specialized scientist and engineers. Here is a tentative list, with some commentary:

- The complex interplay of phonon and electrons, i.e. thermal conductivity including full electron-phonon effects. The presence of independent electron and phonon population and, the vastly different energy scale involved in the excitation of these two particles. On a even more difficult level, we can have out-of-equilibrium phonon and electron populations, with possibly different temperatures.
- The treatment of phase transition. When approaching a transition, perturbative methods fail, because of the instability of harmonic phonons, and MD-based methods become prohibitively expensive and unreliable, as strong bias in the distribution of the atomic displacements makes ergodicity difficult to attain. The enforcement of some symmetry can help in exploring the phase space, but is a very human-guided process, and such prone to bias and errors. The combination of unbiased phase-space exploration techniques (such as metadynamics [160]) with TDEP or time-correlators [37] methods may be a future approach. The use of machine-learning methods to increase the sampling time with a reasonable computation cost may also
- High-entropy alloys or simply non stoichiometric crystals are another class of important problems that are difficult to treat with current techniques. On one side, “reciprocal-space” techniques, are suitable for large perfect crystals, possibly with the insertion of some disorder via semi-empirical or non-equilibrium Green-function techniques [161]; on the other hand, even the most advanced “real-space” approaches [52, 162] require very large and expensive supercells when an important fraction of heat carriers have long mean-free paths.

The study of these topics will certainly be central for the next decade. For what the author is concerned, the first point is the topic of new collaborations [99] with the aim to develop a more sophisticated solver of that Boltzmann transport equation, capable of taking into account out-of-equilibrium populations. The most direct application of the development is the study of thermo-electric materials, where the interplay between phonon and electrons is crucial to differentiate between a bad conductor and a good thermoelectric.

The second point, is also part of current developments, i.e. in Ref. 37, combining quantum correlators (a more rigorous approach than TDEP) with advanced techniques for dynamical sampling. Possible applications range from the study of hydrogen based materials, requiring a quantum treatment of nuclear motions, in combination with advanced density functional theory techniques, and the characterisation of metastable structures.

Finally, the third point will be the subject of future research, in order to push forward the research on thermal properties under deep Earth mantle conditions [49], which include extreme temperature and pressure and disordered minerals (es.  $\text{Fe}_x\text{Mg}_{1-x}\text{O}$ ) including applications to the study of geological properties of other planets.

# Appendix A

## Dynamical matrices and Force Constants

Small displacement of the atoms in a crystal can be approached in two ways: (1) as a combination of atoms moving individually, and independently from all the other or (2) as a combination of monochromatic perturbation. In a monochromatic perturbation all the atoms move in unison, with a certain periodicity which is described by the perturbation wavevector  $\mathbf{q}$ . The two kind of perturbation are linked to each other by Fourier transform. Before seeing this relation, we need some definitions.

Let's describe the crystal as a collection of unit cells, each unit cell is identified by the a direct-lattice grid vector  $\mathbf{R}_J = N_J^1 \mathbf{a}_1 + N_J^2 \mathbf{a}_2 + N_J^3 \mathbf{a}_3$  with  $\mathbf{a}_{1,2,3}$  being the lattice basis vectors, and  $N_J^{1,2,3}$  relative integers:  $\dots, -2, -1, 0, 1, 2, \dots$ . We can see  $N_J^{1,2,3}$  both as the coordinates of  $\mathbf{R}_J$  in crystalline (aka fractionary) coordinates and as the index of cell  $\mathbf{R}_J$ , i.e. the cell that has  $\mathbf{R}_J$  as its corner. For this reason, we will drop the  $J$  label from here on, and use just  $R$  to refer both to the lattice vector and its cell.

Inside each unit cell one has a certain number  $N_a$  of atoms, which are, at the equilibrium, at position  $\boldsymbol{\tau}_i$  ( $i = 1, \dots, N_a$ ) relative to the corner  $\mathbf{R}$  of their cell. At finite temperature (or because of zero-point motion) the atoms will move around this equilibrium, at a give moment their displacements from equilibrium are  $\mathbf{u}_{i,j}$ . The position of atom  $i$  in cell  $\mathbf{R}$  is then going to be

$$\mathbf{r}_{i,\mathbf{R}} = \mathbf{R} + \boldsymbol{\tau}_i + \mathbf{v}_{i,\mathbf{R}} \quad (\text{A.1})$$

### A.1 Force constants

Let's see case (1) first. The derivative of the total energy with respect to the position of two atoms is called force constant:

$$FC(\alpha, i, \mathbf{R}; \beta, i', \mathbf{R}') = \frac{\partial^2 E}{\partial \mathbf{r}_{i,\mathbf{R}}^\alpha \partial \mathbf{r}_{i',\mathbf{R}'}^\beta} \quad (\text{A.2})$$

Where  $\alpha$  and  $\beta$  indicate a Cartesian direction ( $x, y, z$ ). It can be easily shown, that it is equivalent to take the derivatives w.r.t the displacements  $\mathbf{v}_{i,\mathbf{R}}$ . Furthermore, as our crystal is periodic, the derivative can only depends on the distance between  $\mathbf{R}$  and  $\mathbf{R}'$ , and not their absolute value. We can then take, without loss of generality,  $\mathbf{R}' = 0$  (as it is done in the Quantum ESPRESSO code)

### A.2 Monochromatic perturbation (phonons)

Now we see case (2). We have a monochromatic perturbation when all the atoms move with a well defined wavevector:

$$\mathbf{u}(\mathbf{q})_{\mu,j} = \text{Re}(e_\mu e^{2\pi \mathbf{q} \cdot \mathbf{r}}) \quad (\text{A.3})$$

The reciprocal of the wavevector is the wavelength  $\lambda = 1/|q|$ . The vector  $\mathbf{e}_\mu$  is the polarization of the perturbation, which defines in which direction and to which extent each atom moves<sup>1</sup>. Any choice is valid and gives rise to a different perturbation. It is usually represented as a vector of  $3N_a$  elements. Its elements correspond to the Cartesian components of each atom (atom 1 x, atom 1 y, ... atom N z), and it is usually assumed normalized. In order to consider all possible perturbations, one has to take  $3N_a$  polarizations that form a basis of the  $3N_a$ -dimensional space. The simplest choice is to just take the Cartesian basis  $(1, 0, 0, \dots, 0)$ ,  $(0, 1, 0, \dots, 0)$ , ...,  $(0, 0, 0, \dots, 1)$ , but a more natural basis emerges when dynamical matrices are introduced. It is customary to refer to the components of  $\mathbf{e}$  with a single index like  $\nu$  when we take it to be any vector, on the other hand when using a Cartesian basis we can just take it to be a couple  $\nu = (\alpha, i)$  with  $\alpha = x, y, z$  and  $i$  the index of an atom in the unit cell.

Any arbitrary set of displacements  $\mathbf{v}_{i,j}$  can be projected on an harmonic perturbation:

$$\mathbf{v}(\mathbf{q})_\mu = \sum_j \mathbf{u}(\mathbf{q})_{\mu,j} \mathbf{v}_{\mu,j} \quad (\text{A.4})$$

$$\mathbf{v}(\mathbf{q})_\mu = \sum_j e_\mu e^{2\pi\mathbf{q}\cdot\mathbf{R}} \mathbf{v}_{\mu,j} \quad (\text{A.5})$$

Which looks a lot like a Fourier transform, except for the additional complication of the polarization  $\mathbf{e}$ , which we can safely hide/ignore most of the time. An alternative convention uses as an argument for the exponential  $2\pi\mathbf{q}\cdot\mathbf{r}$ , i.e. with a phase  $e^{2\pi\mathbf{q}\cdot\mathbf{r}}$ . This choice is equivalent, as the phase difference can be put in  $\mathbf{e}$ , but not equal. It is often used by real-space code, one has to pay attention when importing data. For simplicity, we will use the Cartesian basis, in this case, when taking the component along direction *alpha* for atom *i* of  $\mathbf{v}$  the polarization  $\mathbf{e}_\mu$ , becomes just  $\delta_{\alpha,i}$ .

$$\mathbf{v}_{\alpha,i}(\mathbf{q}) = \sum_j e^{2\pi\mathbf{q}\cdot\mathbf{R}} v_{i,j}^\alpha \quad (\text{A.6})$$

This is the form that is used 99% of the times, when we can forget  $\mathbf{e}$ .

In order to construct the harmonic Hamiltonian, we are interested in the second derivative of the total (ion-ion + ion-electron + electron-electron) energy w.r.t. the displacement of two atoms. An alternative approach, the one used in plane-waves based DFPT, is to compute the derivative w.r.t. to harmonic perturbations. It is easy to show that the derivative can only be non-zero when the two perturbations have opposite wavevectors  $\mathbf{q}_1 = -\mathbf{q}_2$ . Also note that  $\mathbf{v}(-\mathbf{q})$  is the complex conjugate of  $\mathbf{v}(\mathbf{q})$ . We still have to consider all possible  $3N_a \times 3N_a$  combination of polarizations, in the same way as for the FC we have to derive w.r.t. all the atoms in the cell and Cartesian directions. The derivative is the dynamical matrix, is usually computed in the Cartesian basis

$$D_{\mathbf{q}}(\mu; \nu) = \frac{\partial E}{\partial \mathbf{v}_\mu(\mathbf{q}) \partial \mathbf{v}^*(\mathbf{q})_\nu} \quad (\text{A.7})$$

### A.3 Fourier transform

I'll omit how to actually compute the derivative with respect to  $\mathbf{u}(\mathbf{q})$  in DFPT, as it would take far too long. What is important to keep in mind is that because  $\mathbf{u}(\mathbf{q})$  is a periodic perturbation, we can use the standard techniques (i.e. Bloch theorem), to do the calculation in a unit cell. On the other hand, to compute the force constants in real space (by finite differences aka frozen phonon), we need in principle the entire infinite systems, and, in practice, a system at least as large as the distance between the two atoms being moved.

The relation that links FC and phonons, can be derived directly from eq. A.6. The formula is as following:

$$D_{\mathbf{q}}(\alpha, i; \beta, j) = \sum_{\mathbf{R}, \mathbf{R}'} e^{2\pi(\mathbf{q}\cdot\mathbf{R} - \mathbf{q}\cdot\mathbf{R}')} F(\alpha, i, \mathbf{R}; \beta, i', \mathbf{R}') \quad (\text{A.8})$$

$$D_{\mathbf{q}}(\alpha, i; \beta, j) = \sum_{\mathbf{R}} e^{2\pi(\mathbf{q}\cdot\mathbf{R})} F(\alpha, i, \mathbf{R}; \beta, i', \mathbf{0}) \quad (\text{A.9})$$

---

<sup>1</sup>Note that it is completely independent from the wavevector  $\mathbf{q}$ . It is entirely possible for  $\mathbf{q}$  and  $\mathbf{e}$  to be orthogonal, these are "transverse phonons", if  $\mathbf{q}$  and  $\mathbf{e}$  are parallel, the phonon is "longitudinal".

By using translational invariance, we got rid of one of the two sums. The inverse is just:

$$F(\alpha, i, \mathbf{R}; \beta, i', \mathbf{0}) = 1/\Omega \int d^3 \mathbf{q} e^{-2\pi i \mathbf{q} \cdot \mathbf{R}} D_{\mathbf{q}}(\alpha, i; \beta, j) \quad (\text{A.10})$$

Where  $\Omega$  is the volume of the unit cell. We see this formula more commonly, in its discretized form:

$$F(\alpha, i, \mathbf{R}; \beta, i', \mathbf{0}) = 1/n_q \sum_{\mathbf{q}} e^{-2\pi i \mathbf{q} \cdot \mathbf{R}} D_{\mathbf{q}}(\alpha, i; \beta, j) \quad (\text{A.11})$$

Where  $n_q$  is the number  $\mathbf{q}$ -points in the discrete grid.

## A.4 Grid of q-points and supercell

Now we go in the other direction: we can compute the force constants on a finite grid of q-points, and see what we can tell about the force constants. Let's suppose that the grid is  $n \times n \times n$ , it has  $n_q = n^3$  points in total, and the same number of points in every direction, this is of course not always the case but the generalization is trivial and it streamlines the discussion. Let's take a special  $\mathbf{R} = N\mathbf{a}_1$ , we want to compute  $F(\mathbf{R})$  using eq. A.11. It is easy to show that if we add  $n$  to  $N$  we only get a phase factor  $e^{-2\pi i \mathbf{q} \cdot n\mathbf{a}_1} = 1$ . It is 1 because  $\mathbf{q}$  is commensurate with  $n$  by construction. I.e. the FCs are periodic with the periodicity of the supercell  $n \times n \times n$ . We only need the FCs for couple of atoms inside this supercell, all the terms outside are periodic.

## A.5 Fourier interpolation, recentering

If we could integrate over the q-points with an infinitesimal mesh, as in eq. A.10, we would obtain all the force constant up to infinite distance. On the other hand, as we have seen in the previous section, FCs that are obtained from a  $n \times n \times n$  grid of q-points are periodic over a  $n \times n \times n$  supercell. However, we can still expect that force constants from atoms that are far away are smaller than those for atoms which are close to each other. In particular, if we take a very large grid, we will eventually find that all the “distant” terms become negligible. The idea of Fourier interpolation, is to take the FCs that we have and assume that the more distant terms are zero. This allows us to go back to reciprocal space at any q-point as if we had an infinitesimal grid q-space.

The caveat is that the definition of “distant” has to take into account two facts: (1) Thank to periodic boundary conditions, the opposite sides of the supercell are close to each other. (2) In practice, an atom may not be inside the unit cell to which it pertains, or closer to its  $R$  than to any other lattice vector. I.e. we cannot use the cell-cell distance  $(\mathbf{R} - \mathbf{R}')$  only the atom-atom distance  $(\mathbf{r} - \mathbf{r}')$  is reliable, and we must take care to always use the minimum distance between all periodic copies of atoms.

In order to see this more clearly, we have to write it down in algorithmic terms. First of all, let's define the super-lattice whose unit cell is the super-cell defined by the vectors  $\mathbf{A}_1 = n\mathbf{a}_1$ ,  $\mathbf{A}_2 = n\mathbf{a}_2$  and  $\mathbf{A}_3 = n\mathbf{a}_3$ . We will use the letter  $\mathbf{T}$  to refer to a vector of this super-lattice:  $\mathbf{T} = T_1\mathbf{A}_1 + T_2\mathbf{A}_2 + T_3\mathbf{A}_3$ , with integer coefficients  $T_{1,2,3} = \dots, -2, -1, 0, 1, 2, \dots$

We define the “PBC-distance” between two points  $\mathbf{r}$  and  $\mathbf{r}'$  as the  $\min |\mathbf{r} - (\mathbf{r}' + \mathbf{T})|_{\mathbf{T}}$ . In practice, we only need to search for the minimum for  $T_{1,2,3}$  in a limited range  $\pm 2$  or  $\pm 3$  is sufficient in almost every real-world case. One can see that what we are doing is to construct a Wigner-Seitz cell of the super-lattice around  $\mathbf{r}$  and take the  $\mathbf{r}'$  which is inside it. It may happen (very often in practice) that  $\mathbf{r}'$  falls exactly on a surface, edge or corner of the WS cell, in this case there are several choices which give the same distance; we will need to keep this in mind later. We will say that two atoms at position  $\mathbf{r}$  and  $\mathbf{r}'$  are “nearby” if they are inside the super-WS cell centered on each other, or equivalently if their regular distance is equal to their PBC-distance, and that they are “distant” otherwise. If there are several possible choices for the PBC-distance we will call them “equivalent copies”, and their number will be  $N_e$

The task is to construct the best approximation of the infinite FCs ( $F^\infty$ ) from the periodic FCs ( $F^{PBC}$ ). Again, we can assume that the second  $\mathbf{R}$  is zero, without loss of generality. The rule is:

$$F^\infty(\alpha, i, \mathbf{R}; \beta, i', \mathbf{0}) = \begin{cases} 0 & \text{if } \mathbf{r} + \mathbf{R} \text{ is distant from } \mathbf{r}' \\ \frac{1}{N_e} F^{PBC}(\alpha, i, \mathbf{R}; \beta, i', \mathbf{0}) & \text{if } \mathbf{r} + \mathbf{R} \text{ is close to } \mathbf{r}' \\ & \text{(and they have } N_e \text{ equivalent copies)} \end{cases} \quad (\text{A.12})$$

Considering all the equivalent copies is not strictly necessary. In the mathematical ideal case, and as long as we are only interested in interpolating the dynamical matrix it makes no difference. In the real world case, where finite precision is used, it helps preserving the correct symmetry that may cause degenerate lines in the phonon dispersion to have slightly different values. Also, if using  $F^\infty$  to compute harmonic forces, as we will do in sec. A.6, not including all equivalent copies would break the crystal symmetry.

It is important to note that using  $F^\infty$  and  $F^{PBC}$  to compute  $D(\mathbf{q})$  at a  $\mathbf{q}$  from the initial  $n \times n \times n$  grid, via eq. A.9, must give the exact same result (to numerical precision!). If the FC came from the inverse Fourier transform of dynamical matrices, then exactly the initial value must be recovered.

Observations: (1) If the initial list of  $F^{PBC}$  contains elements from exactly  $n \times n \times n$  unit cells, now we can have more because the PBC-distance for a couple of atoms in the same cell, may be found for a different  $\mathbf{T}$  than for another couple in the same cell. (2) This centering operation is done in a peculiar way in the q2r/matdyn code, using the wsinit and wsweight subroutines, the first constructs a list of vectors  $\tilde{\mathbf{R}}$  that defines the WS cell of the lattice given in input, the second one checks if  $\mathbf{v} \cdot \tilde{\mathbf{R}} < |\tilde{\mathbf{R}}|/2$ , which ensures that  $\mathbf{v}$  is inside the WS cell. (3) A simplified centering which takes just  $\mathbf{R}$  inside the Wigner-Seitz cell of the super-lattice is not equivalent, and not optimal, but will work for a sufficiently fine grid. Even just ensuring that  $R_{1,2,3}$  is between  $-n/2$  and  $n/2$  will work decently for sufficiently fine grids. (4) In a numerical implementation the terms which are zero are not actually stored, the code will just construct a list of the non-zero terms and only sum over them.

## A.6 Computing forces from force constants

Let's say that we have computed from *ab initio* the first and second derivatives of the total energy with respect to displacement, i.e. the one-body and two-body force constants:

$$F(\alpha, i, \mathbf{R}) = -\frac{\partial E}{\partial \mathbf{v}_{\alpha, i, \mathbf{R}}} \quad (\text{A.13})$$

$$F(\alpha, i, \mathbf{R}; \beta, i', \mathbf{R}') = \frac{\partial^2 E}{\partial \mathbf{v}_{\alpha, i, \mathbf{R}} \partial \mathbf{v}_{\beta, i', \mathbf{R}'}} \quad (\text{A.14})$$

We have put a minus sign for the linear term in eq. A.13 as it is customary. We may assume that  $F(i, \mathbf{R})$  are all zero, i.e. that we are at the equilibrium atomic positions, but this is not necessary. We want to compute the force acting on a specific atom ( $i, \mathbf{R}$ ) when we slightly move all the atoms by a set of arbitrary displacements  $\mathbf{u}_{i, \mathbf{R}}$ , itself included. In other words, we want to compute the first derivative of the energy at the displaced coordinates. First of all, let's express the energy as a Taylor's expansion at coordinates  $\mathbf{r} + \mathbf{u}$

$$E(\mathbf{r} + \mathbf{u}) = E(\mathbf{r}) - \sum_{\alpha, i, \mathbf{R}} F(\alpha, i, \mathbf{R}) u_{\alpha, i, \mathbf{R}} + \frac{1}{2} \sum_{\alpha, i, \mathbf{R}; \beta, i', \mathbf{R}'} F(\alpha, i, \mathbf{R}; \beta, i', \mathbf{R}') u_{\alpha, i, \mathbf{R}} u_{\beta, i', \mathbf{R}'} \quad (\text{A.15})$$

Now imagine we move an atom ( $i, \mathbf{R}$ ) by an additional amount  $\epsilon$  along direction  $\alpha$ . We simply differentiate w.r.t.  $\epsilon$  (and change sign, because it is a force), note that we get a factor 2 because the terms ( $i, \mathbf{R}; i', \mathbf{R}$ ) and ( $i', \mathbf{R}'; i, \mathbf{R}$ ) are equal.

$$F(\mathbf{r} + \mathbf{u})_{\alpha, i, \mathbf{R}} = F_{\alpha, i, \mathbf{R}} - \sum_{\beta, i', \mathbf{R}'} FC(\alpha, i, \mathbf{R}; \beta, i', \mathbf{R}') u_{\beta, i', \mathbf{R}'} \quad (\text{A.16})$$

It is important to note that the largest element of  $F(\alpha, i, \mathbf{R}; \beta, i', \mathbf{R}')$  is typically  $F(\alpha, i, \mathbf{R}; \alpha, i, \mathbf{R})$ , i.e. that the strongest effect that each atom feels depends on its own movement. Atoms that do not move, will still feel an effect from all the ones that do.

We can use either  $F^\infty$  or  $F^{PBC}$  in eq. A.16, but the meaning of the two operations is different, and the correct one depends on what we are trying to do. If we want to compare to an *ab initio* calculation done in a supercell of the same size as the one used to compute the FCs, then  $F^{PBC}$  should give the best results. If we want to apply to a cell which is larger, than the range of the computed FCs, than  $F^\infty$  are the correct choice as they don't introduce spurious interactions between distant atoms and preserve symmetry. For a smaller cell, they would give the same result, but  $F^{PBC}$  is numerically cheaper.

It is straightforward to extend this equation to include higher order terms. Now suppose you run *ab initio molecular dynamics simulations* (aimd) using a supercell with a size that is commensurate with the size of the grid used in generating the FCs (i.e.  $n_q \times n_q \times n_q$ ). At each time step,  $t$ , the displacement of an atom from equilibrium will be

$$\mathbf{u}_{\beta,i,\mathbf{R}}(t) = \mathbf{r}_{\beta,i,\mathbf{R}}(0) - \mathbf{r}_{\beta,i,\mathbf{R}}(t) \quad (\text{A.17})$$

where  $\mathbf{r}_{\beta,i,\mathbf{R}}(0)$  is the equilibrium position of atom  $i$ , in cell  $\mathbf{R}$ , along direction  $\beta$ , and  $\mathbf{r}_{\beta,i,\mathbf{R}}(t)$  is the time dependent position. There will be  $N$  configurations for  $n$ -steps molecular dynamics. At each step, we can express the harmonic force from Eq. A.16 as

$$F(t)_{\alpha,i,\mathbf{R}} = F_{\alpha,i,\mathbf{R}} - \sum_{\beta,i',\mathbf{R}'} \Phi(\alpha,i,\mathbf{R};\beta,i',\mathbf{R}') u(t)_{\beta,i',\mathbf{R}'} \quad (\text{A.18})$$

where  $\Phi_{\alpha\beta}$  is the harmonic force constant from DFPT

## A.7 Translational invariance

For convenience, we want to store  $F(i,\mathbf{R},i',\mathbf{0})$ , which is all we need to do the Fourier interpolation. However, at times we will need the general  $F(i,\mathbf{R},i',\mathbf{R}')$ . The force constants in principle could be recentered or periodic; here we start with the periodic case, which is easier.

One simple way is to pass by reciprocal space, i.e. compute the dynamical matrices on the original grid (which we know is an exact operation) and then use Eq. A.11 in the general form with two  $\mathbf{R}$  indexes, i.e.:

$$F(\alpha,i,\mathbf{R};\beta,i',\mathbf{R}') = 1/n_q \sum_{\mathbf{q}} e^{-2\pi\mathbf{q}\cdot(\mathbf{R}-\mathbf{R}')} D_{\mathbf{q}}(\alpha,i;\beta,j) \quad (\text{A.19})$$

This is not the most efficient way, if we have to do it over and over we use a map that tells us which  $\mathbf{R}''$  solves  $\mathbf{R}'' = \mathbf{R} - \mathbf{R}' + \mathbf{T}$ , given  $\mathbf{R}$  and  $\mathbf{R}'$  with  $\mathbf{T}$  a vector of the super-lattice. Then we know that  $F(\alpha,i,\mathbf{R};\beta,i',\mathbf{R}') = F(\alpha,i,\mathbf{R}'';\beta,i',\mathbf{0})$ , thanks to translational invariance and periodic boundary conditions. This can be done by an exhaustive search, using the fact that in crystalline/fractionary coordinates the lattice vectors are integer-valued.

If we are dealing with recentered force constants, periodic boundary conditions do not hold. In this case, if  $\mathbf{R}''$  is not in the list of non-zero force constants, it means that  $F(\alpha,i,\mathbf{R};\beta,i',\mathbf{R}')$  is also zero. One has to be careful, because this condition may depend on  $i$  and  $j$ . The tricky part, is to construct a list of  $\mathbf{R}$ , for each  $\mathbf{R}'$ , that (1) point to all the non-zero force constant elements and (2) only point to a small, and possibly zero, number of vanishing force constants, in order to be efficient.

## A.8 Acoustic sum rule

We want that the 2-body contribution to the force is zero if all the displacements are the same. We simply take Eq. A.16 simplify all  $u_{\beta,i',\mathbf{R}'}$  as they should be identical and find any residual:

$$\frac{1}{2} \sum_{i,\mathbf{R}} F(\alpha,i,\mathbf{R};\beta,j,\mathbf{0}) = \theta_{j,\alpha,\beta} \quad (\text{A.20})$$

We expect  $\theta_{j,\alpha,\beta}$  to vanish for any  $i$ ,  $\alpha$  and  $\beta$ . What happens in practice, is that because of finite precision of *ab initio* calculations, we will get a non-zero residual. We will then proceed to enforce the condition, by removing the residual from FC. There are several recipes to do this, the simplest one takes it away from the on-site term, i.e  $F(\alpha,i,\mathbf{0};\beta,i',\mathbf{0}') \rightarrow F(\alpha,j,\mathbf{0};\beta,j,\mathbf{0}') - \theta_{j,\alpha,\beta}$ .

Applying the sum rule and recentering the force constants are compatible operations. I.e. one can enforce the sum rule on  $F^{PBC}$ , then apply the recentering operation and get some  $F^\infty$  which are still respecting sum rules. This is not true for higher order force constants, which require more complicated mechanisms to apply the sum rules.

## Appendix B

# Basis of symmetric dynamical matrices

### B.1 symmetries of a crystal

A crystal has up to 48 symmetry operations. Each operation is a rotation, which can be expressed as a matrix  $3 \times 3$ . To rotate a vector  $\mathbf{v}$ , one simply does " $S \mathbf{v}$ ". For a standard matrix  $M$ , one has to do  $SMST^T$ .

The lattice respects a certain symmetry operation  $S$  if for all three basis vectors  $S\mathbf{a}_i = \mathbf{a}_j$  for every  $i$ . Notably,  $i$  and  $j$  do not have to be the same. Because lattices that can periodically fill the space are in limited number and need to have some regularity (at least, opposite faces need to be parallel) the possible symmetry operations are also limited. Without going in too much detail, what we need to know is that it is possible to find a set of "elementary" symmetry operation for a lattice, i.e. a group, which has some special properties. In particular, if you combine two symmetry operation from a group, you get a third one which is still in the group. All groups contain the identity, and the identity alone is a group.

When we add a basis, i.e. more than one atom in the lattice, it becomes more complicated. When we rotate the lattice, also the atoms rotate. Let's say the basis is  $\tau_i^J$  where  $J$  denote equivalent atomic type (same element, same oxidation state, same spin) and  $i$  is the index of atoms of that type. The crystal has symmetry operation  $S$  if  $S\tau_i^J = \tau_{i'}^{J'} + \mathbf{f} + \mathbf{R}_i^J$  for every  $i, J$ , where  $\mathbf{f}$  is called a fractional translation and has to be the same for every  $i, J$ , while  $\mathbf{R}_i^J$  is  $\mathbf{q}$ lattice vector, and can be different for different  $i, J$ . In other words, the symmetry operation  $S$  has to send every atom to itself or another atom of the same type, minus a global fractional translation and periodic boundary conditions.

### B.2 Irreducible wedge of the Brillouin Zone

We say that a point  $\mathbf{q}$  is invariant under symmetry operation  $S$  if  $S\mathbf{q} = \mathbf{q} + \mathbf{G}$ , i.e. if rotating  $\mathbf{q}$  with  $S$  sends it to itself, minus periodic boundary conditions. The set of symmetry operations that leave  $\mathbf{q}$  unchanged are called the "small group" of  $\mathbf{q}$ . They are a sub-set of the symmetry operations of the crystal, and they form a group. One special case is the  $\Gamma$  point (aka  $(0, 0, 0)$ ) which has all the symmetries.

A useful feature is that, in a regular  $n \times n \times n$  grid of  $\mathbf{q}$ -points, some points will be equivalent. I.e. given a point  $\mathbf{q}$  in the grid and a symmetry operation  $S$  of the crystal, it exist a point  $\mathbf{q}'$  in the grid and a vector  $\mathbf{G}$  of the reciprocal lattice such that

$$\mathbf{q}' = S\mathbf{q} + \mathbf{G} \tag{B.1}$$

In other words, points  $\mathbf{q}$  and  $\mathbf{q}'$  are linked to each other by symmetry operation  $S$ . We can also define the "star" of a  $\mathbf{q}$ -point  $\mathbf{q}$ , as the set of points  $\mathbf{q}'$  for which the condition of eq. B.1 is verified for at least one symmetry operation of the crystal. It is possible to show that the number of  $\mathbf{q}$ -points in the star  $\mathbf{q}$  times the number of symmetry operation in the small group of the same  $\mathbf{q}$  is equal to the total number of symmetries of the crystal.

When doing a DFPT calculation, we can exploit this symmetry to reduce the number of points to compute. I.e. we can detect the points in the grid that form a star and only compute one of them. We do however, need to find a way to obtain the dynamical matrix  $D(\mathbf{q})$  from that of  $D(\mathbf{q}')$  as they are not equal. We will see how to "symmetrize" the dynamical matrix in the next section.

### B.3 Applying symmetry to dynamical matrices

Symmetrizing a dynamical matrix is not as simple as rotating it like a matrix, i.e. we cannot just do  $SDS^T$  which only applies to  $3 \times 3$  matrices, like the matrices of direct and reciprocal lattice vectors. On the other hand, the dynamical matrix itself, can be decomposed in  $N_a \times N_a$  minors, each one pertaining to atoms  $i$  and  $j$  which can be rotated as a matrix. However, after the rotation the minor will not be pertaining to atoms  $i$  and  $j$ , but to atoms  $i'$  and  $j'$  such that  $\tau_{i'} = S\tau_i + \mathbf{R}$  and of course  $\tau_{j'} = S\tau_j + \mathbf{R}$ .

$$D_{i',j'}(S\mathbf{q}) = SD_{i,j}(\mathbf{q})S^T \quad (\text{B.2})$$

For shorthand, we may refer to this operation as  $SDS^T$ , but it is important to keep in mind that is quite more complex. One can show, that if we loop this expression over all  $i, j$  we will obtain all  $i'$  and  $j'$ . Equation B.2 can be used for two very useful tasks: (1) to symmetrize and (2) to reconstruct the star from a single  $\mathbf{q}$ point.

Let's see symmetrization first. If the small group of  $\mathbf{q}$  contains  $N_s(\mathbf{q})$  symmetry operations, when we rotate  $D$  with any of these, it shall remain unchanged the same result. However, the dynamical matrix is obtained as a sum over k-points: we can reduce the grid of electronic k-points with the symmetry operations of the small group of  $\mathbf{q}$  and apply symmetry after the sum. In this way, we can save a lot of CPU time. In order to symmetrize  $D(\mathbf{q})$  we rotate it with all  $N_s(\mathbf{q})$  symmetries and average the result.

$$D(\mathbf{q}) \frac{1}{N_s(\mathbf{q})} \sum_{k=1, N_s(\mathbf{q})} S_k D^{\text{rdx}}(\mathbf{q}) S_k^T \quad (\text{B.3})$$

Where  $D^{\text{rdx}}(\mathbf{q})$  is the "reduced" dynamical matrix obtained by doing a partial sum over the reduced k-points grid.

Second: recovering the star. In this case, after having computed  $D(\mathbf{q})$  *ab initio*, and symmetrized it if necessary, we can rotate it to obtain  $D(\mathbf{q}')$  for all  $\mathbf{q}'$  in the star of  $\mathbf{q}$ . In principle, using any one of the symmetry operations that do  $\mathbf{q} \rightarrow \mathbf{q}' + \mathbf{G}$  is sufficient. In practice, we use all the appropriate ones and average the result, to better preserve symmetry.

If among the symmetries of the crystal there is one that send  $\mathbf{q}$  into  $-\mathbf{q}$ , i.e.  $S\mathbf{q} + \mathbf{G} = -\mathbf{q}$ , we can use this fact to reduce the number of k-points for the electronic calculation. We can exploit it in a similar way, but it will require adding a complex conjugate operation in order to convert  $D(\mathbf{q})$  to  $D(-\mathbf{q})$ .

### B.4 Defining a matrix-matrix scalar product

Dynamical matrices are hermitian, i.e. they have the property  $M^T = M^*$  (the transpose matrix is equal to its complex conjugate). As a consequence, all their eigenvalues are real numbers. When defining a scalar product  $A \cdot B$  between two hermitian matrices  $A$  and  $B$  we want it to have these properties: (1) If  $A, B$  and  $C$  are hermitian matrices and  $s = A \cdot B$ , then also  $sC$  must be a hermitian matrix. This mean in practice that  $s$  must be a real number. (2) If  $s = A \cdot A$  then  $s$  is positive definite. A simple way to define a scalar product that respect these rules is

$$A \cdot B = \text{Tr}[AB] \quad (\text{B.4})$$

Where  $\text{Tr}$  is the trace operation. It is easy to show that this definition respects the conditions above. It is also easy to show that this definition is exactly equivalent to computing

$$A \cdot B = \sum_{i,j} A_{ij}^* B_{ij} \quad (\text{B.5})$$

Which has the advantage of being computationally much faster ( $O(n^2)$  instead of  $O(n^3)$  where  $n$  is the number of atoms), and easily extended to higher-order tensors.

With a scalar product defined, we can construct a basis of orthonormal matrices for any matrix space using the modified Gram-Schmidt (or any other similar) procedure.

## B.5 The space of symmetric dynamical matrices

The generic  $3N_a \times 3N_a$  Hermitian matrix has  $(3N_a)^2$  real-valued degrees of freedom (real number in the diagonal and complex but pairwise conjugate numbers in the upper and lower triangles). However, as we know that the crystal geometry and the  $\mathbf{q}$ -point are sufficient to determine the small-group of symmetry operations, we can wonder if the space of symmetry-compatible dynamical matrices is actually smaller. The more straightforward way to see it, is to construct a basis of orthonormal matrices for this space. The procedure is as follows:

1. Start with an initial guess of  $(3N_a)^2$  hermitian matrices (see later on possible guesses)
2. Symmetrize all of them
3. Throw away all matrices that are zero, normalize the others
4. Apply the Gram-Schmidt algorithm
5. Throw away all the matrices which are zero

We are left with a set of  $N_{\mathbf{q}}$  symmetry-compatible matrices, any dynamical matrix for this  $\mathbf{q}$ , obtained from real simulation of the crystal, must be exactly decomposable on this basis:

$$D(\mathbf{q}) = \sum_{k=1, N_{\mathbf{q}}} (D(\mathbf{q}) \cdot M_k^{\mathbf{q}}) M_k^{\mathbf{q}} \quad (\text{B.6})$$

Where  $M_k^{\mathbf{q}}$  is the symmetrized basis.

In practice,  $N_{\mathbf{q}}$  can be dramatically smaller than  $(3N_a)^2$ , i.e. as small as 1 for the  $\Gamma$  point of highly symmetric material, as typically between 5 and 10 for  $\mathbf{q}$  points in a regular grid of two-atoms crystals.

Steps 4 and 5 are better done together, i.e. some care must be taken during the GS orthonormalization to detect and immediately throw away the matrices that become zero, or the subsequent iterations may break.

The choice of the initial guess is quite important, as it can make this procedure more or less robust. It is especially important that the initial guess spans all the possible  $(3N_a)^2$  dimensions, or we may lose some fraction of the space.

A possible choice is to take matrices that are all zero except for

- $3N_a$  different matrices with an 1 along the diagonal
- $3N_a(3N_a - 1)/2$  with  $1/\sqrt{2}$  at  $i, j$  and  $j, i$  for every couple  $i \neq j$
- $3N_a(3N_a - 1)/2$  with  $i/\sqrt{2}$  at  $i > j$  and  $-i/\sqrt{2}$  at  $j < i$  for every couple  $i \neq j$

Using random matrices should also work, and is a good test to check the resilience of the algorithm to numerical noise.

Another possibility is to start from a trial "real" dynamical matrix for a certain system with the desired symmetry and build the initial trial matrices as  $|e_i \rangle \langle e_j|$ , or in matrix notation  $\mathbf{e}_i^{\dagger} \times \mathbf{e}_i$ , where  $\mathbf{e}_i$  are the eigenvectors of the trial dynamical matrix. In this case, we can decide to exclude the eigenvectors that correspond to zero eigenvalues, which will construct a basis that cannot break acoustic sum rules.

## B.6 Extension to third order matrices

A  $D_3(\mathbf{q}, \mathbf{q}', \mathbf{q}'')$  calculation is fundamentally similar to a  $D_2$  one, the  $\mathbf{q}$  point is generalized to a triplet of points  $(\mathbf{q}, \mathbf{q}', \mathbf{q}'')$ . The small-group is the set of operations that leave all three  $\mathbf{q}$  points unchanged, i.e. the intersection of the small-groups of the three  $\mathbf{q}$ 's. The number of symmetries that we can use is often normally small. The star of  $\mathbf{q}$  is generalized to a tri-star of the  $\mathbf{q}$ 's. As in the 2nd order case, we

can use time-reversal symmetry to obtain the matrix at opposite  $\mathbf{q}$ 's by taking the complex-conjugate of its elements. Furthermore, and specifically to the 3rd order, we can obtain the third-order matrix of permuted  $\mathbf{q}$  vectors simply by applying the same permutation to its indexes. The triplets that are linked by a combination of a symmetry operation, permutation and time-reversal form a generalized-triple-star (G3S). We do not check explicitly if a certain symmetry operation may send each  $\mathbf{q}$  of the triplet into another, but because we do permutation invariance we are not

In the practical case, some of these operations can be redundant, e.g. a certain rotation could be equivalent to a permutation, or to time-reversal. To identify the G3S we take all the possible triplets  $\mathbf{q} + \mathbf{q}' + \mathbf{q}'' = 0$  on a regular grid; for each triplet we generate its G3S and check if it is equivalent to that on any previous triplets: if an equivalent triplet is found, the new triplet is discarded, otherwise it is retained. This procedure allows for a spectacular reduction in the number of triplets; in the graphene case 4096 possible candidates are reduced to only 88 independent triplets.

The  $D_3$  matrix are symmetrized averaging over the symmetry operations inside the G3S. If two of the  $\mathbf{q}$  vectors are identical (opposite) we enforce the permutation (permutation combined with reversal) symmetry on  $D_3$ . In this treatment we have non included the possibility of a symmetry operation that combines a rotation with an index permutation; e.g. one of these two cases. As this kind of operations are complex to implement for a limited benefit; we decided to not include them our code.

As we use symmetry to perform the DFPT calculation only on a reduced number of  $\mathbf{q}$  points, these points are in the irreducible Brillouin zone (IBZ). However, the third-order calculation depends on 3 points: if we can still limit the first one to the IBZ the second has to span the entire BZ. The third point is  $\mathbf{q}_3 = -(\mathbf{q}_1 + \mathbf{q}_2)$  can even be outside the BZ. Instead of extending the initial phonon calculation to all these points, we use crystal symmetry and translational symmetry to reconstruct  $\partial n(\mathbf{r})/\partial u_{\mathbf{q}}$  on the entire regular grid, and apply the translation operator (a phase factor  $e^{i\mathbf{G}\cdot\mathbf{r}}$ ) to transform  $\partial n(\mathbf{r})/\partial u_{\mathbf{q}}$  from  $\mathbf{q}$  to  $\mathbf{q} + \mathbf{G}$ .

We do not have a neat and simple definition of scalar product as in eq. B.4, an immediate generalization of eq. B.5 with one more index produces a real number when computing the square norm, in order to ensure that the product of two generic  $D^3$  tensors is real, we can add all possible permutation of the indeces with a complex conjugate operation depending on the sign of the permutation, i.e. :

$$A_3 \cdot B_3 = \frac{1}{6} \sum_{i,j,k} A_{ijk}^* B_{ijk} + A_{kij}^* B_{kij} + A_{jki}^* B_{jki} + A_{ikj} B_{ikj}^* + A_{jik} B_{jik}^* + A_{kji} B_{kji}^* \quad (\text{B.7})$$

which allows us to apply all the techniques used for the dynamical matrices to the third order matrices.

# Appendix C

## Implementation of 2n+1 theorem

This chapter is adapted from Ref. 25, minus a lot typographical errors in the expressions, which have been fixed.

### C.1 Third order calculation

Here we describe the method used to calculate the third order anharmonic scattering coefficients.

#### C.1.1 Kohn-Sham equations

Within DFT the total energy a system can be determined from the ground state electronic charge density  $n$ . In turn,  $n$  can be obtained by solving the self-consistently the Kohn Sham (KS) equations[163], which, in a periodic crystal are:

$$[T^{\text{kin}} + V^{\text{KS}}]|\psi_{\mathbf{k},i}\rangle = \epsilon_{\mathbf{k},i} |\psi_{\mathbf{k},i}\rangle \quad (\text{C.1})$$

$$V^{\text{KS}}(\mathbf{r}) = v^{\text{ion}}(\mathbf{r}) + \frac{\delta E_{\text{I}}[n]}{\delta n(\mathbf{r})} \quad (\text{C.2})$$

$$n(\mathbf{r}) = \sum_{\mathbf{k},i} \tilde{\theta}_{\mathbf{k},i} |\langle \psi_{\mathbf{k},i} | \mathbf{r} \rangle|^2 \quad (\text{C.3})$$

In Eq. C.1,  $T^{\text{kin}}$  is the single-particle kinetic energy operator,  $V^{\text{KS}}$  is the KS potential,  $|\psi_{\mathbf{k},i}\rangle$  are the Bloch eigenstates with wavevector  $\mathbf{k}$ , band index  $i$ , and energy  $\epsilon_{\mathbf{k},i}$ .  $\langle \mathbf{r} + \mathbf{R} | \psi_{\mathbf{k},i} \rangle = e^{i\mathbf{k}\cdot\mathbf{R}} \langle \mathbf{r} | \psi_{\mathbf{k},i} \rangle$ , being  $\mathbf{r}$  the position and  $\mathbf{R}$  a lattice vector.  $v^{\text{ion}}$  is the external potential due to the ions,  $E_{\text{I}}[n]$  is the interaction functional (Hartree energy plus exchange-correlation contribution). The sum in Eq. C.3 is done on a sufficiently fine grid of  $\mathbf{k}$ -points.

$\tilde{\theta}_{\mathbf{k},i}$  is the occupation of an electronic state:  $\tilde{\theta}_{\mathbf{k},i} = 1$  for valence band electrons and  $\tilde{\theta}_{\mathbf{k},i} = 0$  for conduction ones. The total energy of the system is:

$$\mathcal{E}^{\text{tot}} = E^{\text{ion}} + \sum_{\mathbf{k},i} \epsilon_{\mathbf{k},i} \tilde{\theta}_{\mathbf{k},i} + E_{\text{I}}[n] - \int \frac{\delta E_{\text{I}}[n]}{\delta n(\mathbf{r})} n(\mathbf{r}) d\mathbf{r}, \quad (\text{C.4})$$

where  $E^{\text{ion}}$  is the ionic contribution.

As they are written, the KS equations are suitable when the electronic gap is different from zero (semiconductor or insulator case). When the electronic gap is zero (metallic case) it is customary [121] to introduce smearing function  $\theta_{\sigma}(x)$ , which is characterized by a smearing width  $\sigma$ , and which becomes the step function in the limit  $\sigma \rightarrow 0$ . The KS equation are still written as in Eqs. C.1-C.3, but now  $\tilde{\theta}_{\mathbf{k},i} = \theta_{\sigma}(\epsilon_F - \epsilon_{\mathbf{k},i})$ , where the Fermi energy  $\epsilon_F$  has to be determined self consistently from the condition

$$\sum_{\mathbf{k},i} \tilde{\theta}_{\mathbf{k},i} = N^{\text{el}}, \quad (\text{C.5})$$

where  $N^{\text{el}}$  is the total number of valence electrons. In the metallic case, a proper definition of the energy  $\mathcal{E}^{\text{tot}}$  requires [164] to add to Eq C.4 the term

$$\sum_{\mathbf{k},i} \int_{-\infty}^{\epsilon_F - \epsilon_{\mathbf{k},i}} x \delta_{\sigma}(x) dx, \quad (\text{C.6})$$

where  $\delta_{\sigma}(x) = \partial\theta_{\sigma}(x)/(\partial x)$ .

### C.1.2 Linear response

The derivative of the electronic charge distribution with respect to the  $\mathbf{q}$  periodic displacement  $u_{\mathbf{q}}$  defined in Eq. 2.2 (for simplicity from now on we will drop the indexes  $\alpha$  and  $s$ ) can be determined from first order perturbation theory [116]. For the metallic case, linear response can be implemented following Ref. 164 or the equivalent approach of Ref. 103.

Let us consider a uniform grid of electronic  $\mathbf{k}$  points and a phonon wavevector  $\mathbf{q}$  which belongs to this grid. First, one has to solve the KS equations and obtain the ground state charge density  $n$  and the corresponding KS wavefunctions  $|\psi_{\mathbf{k},i}\rangle$ . Then, one has to define a ‘‘cutoff’’ energy  $\bar{E}$  which separates the electronic states which are completely empty from those which are occupied or partially occupied. In the semiconductor/insulator case,  $\bar{E}$  is any energy within the gap, in the metallic case one can choose any  $\bar{E} \geq \epsilon_F + 3\sigma$ . We define  $P_c$  as the projector on the manifold spanned by the empty states and  $P_v = 1 - P_c$  as the projector on the occupied or partially occupied states.

The derivative of the charge  $\partial n/\partial u_{\mathbf{q}}$  and the derivative of the KS wavefunctions projected on the conduction bands  $|\phi_{\mathbf{k},i}^{\mathbf{q}}\rangle = P_c |\partial\psi_{\mathbf{k},i}/\partial u_{\mathbf{q}}\rangle$  can be obtained by solving self-consistently the equations:

$$[T^{\text{kin}} + V^{\text{KS}} + \alpha P_v - \epsilon_{\mathbf{k},i}] |\phi_{\mathbf{k},i}^{\mathbf{q}}\rangle = -P_c \frac{\partial V_{\text{KS}}}{\partial u_{\mathbf{q}}} |\psi_{\mathbf{k},i}\rangle \quad (\text{C.7})$$

$$\frac{\partial V^{\text{KS}}(\mathbf{r})}{\partial u_{\mathbf{q}}} = \frac{\partial v^{\text{ion}}(\mathbf{r})}{\partial u_{\mathbf{q}}} + \int \frac{\delta^2 E_{\text{I}}[n]}{\delta n(\mathbf{r})\delta n(\mathbf{r}')} \frac{\partial n(\mathbf{r}')}{\partial u_{\mathbf{q}}} d\mathbf{r}' \quad (\text{C.8})$$

$$\begin{aligned} \frac{\partial n(\mathbf{r})}{\partial u_{\mathbf{q}}} = & \sum_{\mathbf{k}} \langle \mathbf{r} | \left\{ \sum_i \tilde{\delta}_{\mathbf{k},i} \epsilon_F^{\mathbf{q}} |\psi_{\mathbf{k},i}\rangle \langle \psi_{\mathbf{k},i}| + \sum_{i,j}^v \frac{\tilde{\theta}_{\mathbf{k},i} - \tilde{\theta}_{\mathbf{k}+\mathbf{q},j}}{\epsilon_{\mathbf{k},i} - \epsilon_{\mathbf{k}+\mathbf{q},j}} |\psi_{\mathbf{k}+\mathbf{q},j}\rangle \langle \psi_{\mathbf{k}+\mathbf{q},j}| V^{\mathbf{q}} |\psi_{\mathbf{k},i}\rangle \langle \psi_{\mathbf{k},i}| + \right. \\ & \left. \sum_i \tilde{\theta}_{\mathbf{k},i} [|\phi_{\mathbf{k},i}^{\mathbf{q}}\rangle \langle \psi_{\mathbf{k},i}| + |\psi_{\mathbf{k},i}\rangle \langle \phi_{\mathbf{k},i}^{-\mathbf{q}}|] \right\} | \mathbf{r} \rangle \end{aligned} \quad (\text{C.9})$$

$\alpha$  is a constant which is chosen in such a way that the linear system of Eq. C.7 is not singular.  $\sum^v$  indicates that the sum is to be performed only on the partially occupied states.  $\tilde{\delta}_{\mathbf{k},i} = \delta_{\sigma}(\epsilon_F - \epsilon_{\mathbf{k},i})$

The first two terms in the right hand side of Eq. C.9 are different from zero only in the metallic case and are written using the notation  $\epsilon^{\mathbf{q}} = \partial\epsilon_F/\partial u_{\mathbf{q}}$  and  $V^{\mathbf{q}} = \partial V_{\text{KS}}/\partial u_{\mathbf{q}}$ .  $\epsilon^{\mathbf{q}} = 0$  for  $\mathbf{q} \neq \mathbf{0}$  and it has to be determined self consistently from

$$\epsilon_F^{\mathbf{q}} = \frac{\sum_{\mathbf{k},i} \langle \psi_{\mathbf{k},i} | V^{\mathbf{q}} | \psi_{\mathbf{k},i} \rangle}{\sum_{\mathbf{k},i} \tilde{\delta}_{\mathbf{k},i}}. \quad (\text{C.10})$$

In the second line of Eq. C.9 we have used the compact notation which reads: when the denominator is equal to zero one has to substitute that expression with the corresponding limit. The same substitution can be used when the denominator is very small in order to gain stability. Thus, when  $\epsilon_{\mathbf{k},i} \sim \epsilon_{\mathbf{k}+\mathbf{q},j}$  one can substitute  $(\tilde{\theta}_{\mathbf{k},i} - \tilde{\theta}_{\mathbf{k}+\mathbf{q},j})/(\epsilon_{\mathbf{k},i} - \epsilon_{\mathbf{k}+\mathbf{q},j})$  with  $-\tilde{\delta}_{\mathbf{k},i}$ . We, finally, remark that the present approach is different from the one described in 164 and that the  $|\phi\rangle$  wavefunctions presently defined are different from the  $|\phi\rangle$  of 164.

### C.1.3 Third order

Let us consider the three phonon displacements  $u_{\mathbf{q}}, u_{\mathbf{q}'}, u_{\mathbf{q}''}$  associated with the wavevectors such that  $\mathbf{q} + \mathbf{q}' + \mathbf{q}'' = \mathbf{0}$ . By solving the linear response equations one can obtain  $\partial n/\partial u_{\mathbf{q}}$  and the  $\{|\phi_{\mathbf{k},i}^{\mathbf{q}}\rangle\}$

corresponding to the three phonons. The third derivative of the energy can then be obtained from

$$\frac{\partial^3 \mathcal{E}^{\text{tot}}}{\partial u_{\mathbf{q}} \partial u_{\mathbf{q}'} \partial u_{\mathbf{q}''}} = \frac{1}{6} \left[ \tilde{E}^{\mathbf{q}, \mathbf{q}', \mathbf{q}''} + \tilde{E}^{\mathbf{q}'', \mathbf{q}, \mathbf{q}'} + \tilde{E}^{\mathbf{q}', \mathbf{q}'', \mathbf{q}} + \tilde{E}^{\mathbf{q}, \mathbf{q}'', \mathbf{q}'} + \tilde{E}^{\mathbf{q}'', \mathbf{q}', \mathbf{q}} + \tilde{E}^{\mathbf{q}', \mathbf{q}, \mathbf{q}''} \right] \quad (\text{C.11})$$

$$\begin{aligned} \tilde{E}^{\mathbf{q}, \mathbf{q}', \mathbf{q}''} &= Z^{\mathbf{q}, \mathbf{q}', \mathbf{q}''} + \frac{\partial^3 E^{\text{ion}}}{\partial u_{\mathbf{q}} \partial u_{\mathbf{q}'} \partial u_{\mathbf{q}''}} + \int \frac{\partial^3 v^{\text{ion}}(\mathbf{r})}{\partial u_{\mathbf{q}} \partial u_{\mathbf{q}'} \partial u_{\mathbf{q}''}} n(\mathbf{r}) d\mathbf{r} + \\ &3 \int \frac{\partial^2 v^{\text{ion}}(\mathbf{r})}{\partial u_{\mathbf{q}} \partial u_{\mathbf{q}'}} \frac{\partial n(\mathbf{r})}{\partial u_{\mathbf{q}''}} d\mathbf{r} + \iiint \frac{\delta^3 E_1[n]}{\delta n(\mathbf{r}) \delta n(\mathbf{r}') \delta n(\mathbf{r}'')} \frac{\partial n(\mathbf{r})}{\partial u_{\mathbf{q}}} \frac{\partial n(\mathbf{r}')}{\partial u_{\mathbf{q}'}} \frac{\partial n(\mathbf{r}'')}{\partial u_{\mathbf{q}''}} d\mathbf{r} d\mathbf{r}' d\mathbf{r}'' \end{aligned} \quad (\text{C.12})$$

Following 102, for the semiconductor/insulator case, we can write:

$$Z^{\mathbf{q}, \mathbf{q}', \mathbf{q}''} = 6 \sum_{\mathbf{k}} \left[ \sum_i \tilde{\theta}_{\mathbf{k}i} \langle \phi_{\mathbf{k}i}^{-\mathbf{q}} | V^{\mathbf{q}'} | \phi_{\mathbf{k}i}^{\mathbf{q}''} \rangle - \sum_{i,j}^v \tilde{\theta}_{\mathbf{k}i} \langle \phi_{\mathbf{k}+\mathbf{q},i}^{-\mathbf{q}} | \phi_{\mathbf{k}-\mathbf{q}',j}^{\mathbf{q}'} \rangle \langle \psi_{\mathbf{k}-\mathbf{q}',j} | V^{\mathbf{q}''} | \psi_{\mathbf{k}+\mathbf{q},i} \rangle \right] \quad (\text{C.13})$$

Following 103, for the metallic case:

$$\begin{aligned} Z^{\mathbf{q}, \mathbf{q}', \mathbf{q}''} &= \sum_{\mathbf{k}} \left\{ 6 \sum_i \tilde{\theta}_{\mathbf{k}i} \langle \phi_{\mathbf{k}i}^{-\mathbf{q}} | V^{\mathbf{q}'} | \phi_{\mathbf{k}i}^{\mathbf{q}''} \rangle + \right. \\ &6 \sum_{i,j}^v \frac{\left[ \tilde{\theta}_{\mathbf{k}+\mathbf{q},i} \langle \phi_{\mathbf{k}+\mathbf{q},i}^{-\mathbf{q}} | V^{\mathbf{q}'} | \psi_{\mathbf{k}-\mathbf{q}',j} \rangle - \tilde{\theta}_{\mathbf{k}+\mathbf{q}',j} \langle \psi_{\mathbf{k}+\mathbf{q},i} | V^{\mathbf{q}} | \phi_{\mathbf{k}-\mathbf{q}',j}^{\mathbf{q}'} \rangle \right] \langle \psi_{\mathbf{k}-\mathbf{q}',j} | V^{\mathbf{q}''} | \psi_{\mathbf{k}+\mathbf{q},i} \rangle}{\epsilon_{\mathbf{k}+\mathbf{q},i} - \epsilon_{\mathbf{k}-\mathbf{q}',j}} + \\ &2 \sum_{i,j,l}^v \left[ \langle \psi_{\mathbf{k},i} | V^{\mathbf{q}} | \psi_{\mathbf{k}-\mathbf{q},j} \rangle \langle \psi_{\mathbf{k}-\mathbf{q},j} | V^{\mathbf{q}'} | \psi_{\mathbf{k}+\mathbf{q}'',l} \rangle \langle \psi_{\mathbf{k}+\mathbf{q}'',l} | V^{\mathbf{q}''} | \psi_{\mathbf{k},i} \rangle \times \right. \\ &\quad \left. \frac{\tilde{\theta}_{\mathbf{k},i} (\epsilon_{\mathbf{k}-\mathbf{q},j} - \epsilon_{\mathbf{k}+\mathbf{q}'',l}) + \tilde{\theta}_{\mathbf{k}-\mathbf{q},j} (\epsilon_{\mathbf{k}+\mathbf{q}'',l} - \epsilon_{\mathbf{k},i}) + \tilde{\theta}_{\mathbf{k}+\mathbf{q}'',l} (\epsilon_{\mathbf{k},i} - \epsilon_{\mathbf{k}-\mathbf{q},j})}{(\epsilon_{\mathbf{k},i} - \epsilon_{\mathbf{k}-\mathbf{q},j}) (\epsilon_{\mathbf{k}-\mathbf{q},j} - \epsilon_{\mathbf{k}+\mathbf{q}'',l}) (\epsilon_{\mathbf{k}+\mathbf{q}'',l} - \epsilon_{\mathbf{k},i})} \right] + \\ &3\epsilon_F^{\mathbf{q}} \left[ \sum_{i,j}^v \frac{\tilde{\delta}_{\mathbf{k},i} - \tilde{\delta}_{\mathbf{k}+\mathbf{q}'',j}}{\epsilon_{\mathbf{k},i} - \epsilon_{\mathbf{k}+\mathbf{q}'',j}} \langle \psi_{\mathbf{k},i} | V^{\mathbf{q}'} | \psi_{\mathbf{k}+\mathbf{q}'',j} \rangle \langle \psi_{\mathbf{k}+\mathbf{q}'',j} | V^{\mathbf{q}''} | \psi_{\mathbf{k},i} \rangle + 2 \sum_i \tilde{\delta}_{\mathbf{k},i} \langle \psi_{\mathbf{k},i} | V^{\mathbf{q}'} | \phi_{\mathbf{k},i}^{\mathbf{q}''} \rangle \right] + \\ &3\epsilon_F^{\mathbf{q}} \epsilon_F^{\mathbf{q}'} \left( \sum_i \tilde{\delta}_{\mathbf{k},i}^{(1)} \langle \psi_{\mathbf{k},i} | V^{\mathbf{q}''} | \psi_{\mathbf{k},i} \rangle \right) - \epsilon_F^{\mathbf{q}} \epsilon_F^{\mathbf{q}'} \epsilon_F^{\mathbf{q}''} \left( \sum_i \tilde{\delta}_{\mathbf{k},i}^{(1)} \right) \left. \right\}, \quad (\text{C.14}) \end{aligned}$$

where  $\tilde{\delta}_{\mathbf{k},i}^{(1)} = \partial \delta_{\sigma}(x) / (\partial x)|_{x=\epsilon_F - \epsilon_{\mathbf{k},i}}$ . Eq. C.14 is written with a compact notation, which reads: when one of the denominators in Eq. C.14 is zero one has to substitute to the corresponding term with the limit obtained for that denominator going to zero. In particular, when  $\epsilon_{\mathbf{k}+\mathbf{q},i} \sim \epsilon_{\mathbf{k}-\mathbf{q}',j}$  in the second line of Eq. C.14, the argument of the sum can be written as

$$- \left[ \tilde{\theta}_{\mathbf{k}+\mathbf{q},i} \langle \phi_{\mathbf{k}+\mathbf{q},i}^{-\mathbf{q}} | \phi_{\mathbf{k}-\mathbf{q}',j}^{\mathbf{q}'} \rangle + \tilde{\delta}_{\mathbf{k}+\mathbf{q},i} \langle \psi_{\mathbf{k}+\mathbf{q},i} | V^{\mathbf{q}} | \phi_{\mathbf{k}-\mathbf{q}',j}^{\mathbf{q}'} \rangle \right] \langle \psi_{\mathbf{k}-\mathbf{q}',j} | V^{\mathbf{q}''} | \psi_{\mathbf{k}+\mathbf{q},i} \rangle.$$

The limits of the factor in the fourth line of Eq. C.14 are

$$\begin{aligned} \text{for } \epsilon_{\mathbf{k},i} \sim \epsilon_{\mathbf{k}-\mathbf{q},j} \neq \epsilon_{\mathbf{k}+\mathbf{q}'',l} : & \frac{\left[ \tilde{\theta}_{\mathbf{k},i} - \tilde{\theta}_{\mathbf{k}+\mathbf{q}'',l} + \tilde{\delta}_{\mathbf{k},i} \right]}{\left[ \epsilon_{\mathbf{k},i} - \epsilon_{\mathbf{k}+\mathbf{q}'',l} + \tilde{\delta}_{\mathbf{k},i} \right]} \frac{1}{\epsilon_{\mathbf{k}+\mathbf{q}'',l} - \epsilon_{\mathbf{k},i}} \\ \text{for } \epsilon_{\mathbf{k}-\mathbf{q},j} \sim \epsilon_{\mathbf{k}+\mathbf{q}'',l} \neq \epsilon_{\mathbf{k},i} : & \frac{\left[ \tilde{\theta}_{\mathbf{k}-\mathbf{q},j} - \tilde{\theta}_{\mathbf{k},i} + \tilde{\delta}_{\mathbf{k}-\mathbf{q},j} \right]}{\left[ \epsilon_{\mathbf{k}-\mathbf{q},j} - \epsilon_{\mathbf{k},i} + \tilde{\delta}_{\mathbf{k}-\mathbf{q},j} \right]} \frac{1}{\epsilon_{\mathbf{k},i} - \epsilon_{\mathbf{k}-\mathbf{q},j}} \\ \text{for } \epsilon_{\mathbf{k}+\mathbf{q}'',l} \sim \epsilon_{\mathbf{k},i} \neq \epsilon_{\mathbf{k}-\mathbf{q},j} : & \frac{\left[ \tilde{\theta}_{\mathbf{k}+\mathbf{q}'',l} - \tilde{\theta}_{\mathbf{k}-\mathbf{q},j} + \tilde{\delta}_{\mathbf{k}+\mathbf{q}'',l} \right]}{\left[ \epsilon_{\mathbf{k}+\mathbf{q}'',l} - \epsilon_{\mathbf{k}-\mathbf{q},j} + \tilde{\delta}_{\mathbf{k}+\mathbf{q}'',l} \right]} \frac{1}{\epsilon_{\mathbf{k}-\mathbf{q},j} - \epsilon_{\mathbf{k}+\mathbf{q}'',l}} \\ \text{for } \epsilon_{\mathbf{k},i} \sim \epsilon_{\mathbf{k}-\mathbf{q},j} \sim \epsilon_{\mathbf{k}+\mathbf{q}'',l} : & -\frac{1}{2} \tilde{\delta}_{\mathbf{k},i}^{(1)}. \end{aligned} \quad (\text{C.15})$$

When  $\epsilon_{\mathbf{k}i} \sim \epsilon_{\mathbf{k}+\mathbf{q}'',j}$  one can substitute  $(\tilde{\delta}_{\mathbf{k}i} - \tilde{\delta}_{\mathbf{k}+\mathbf{q}'',j})/(\epsilon_{\mathbf{k}i} - \epsilon_{\mathbf{k}+\mathbf{q}'',j})$  with  $-\tilde{\delta}_{\mathbf{k},i}^{(1)}$ .

Finally, once the the derivative in Eq. C.11 has been determined, one can obtain the phonon scattering coefficients by combining Eq. 2.7 and Eq. 2.8. We also remark that

$$\frac{\partial^3 \mathcal{E}^{\text{tot}}}{\partial u_{\mathbf{q}+\mathbf{G}} \partial u_{\mathbf{q}'} \partial u_{\mathbf{q}''}} = \frac{\partial^3 \mathcal{E}^{\text{tot}}}{\partial u_{\mathbf{q}} \partial u_{\mathbf{q}'} \partial u_{\mathbf{q}''}}$$

being  $\mathbf{G}$  a vector of the reciprocal lattice. Thus, we have not lost of generality by imposing  $\mathbf{q}+\mathbf{q}'+\mathbf{q}'' = \mathbf{0}$  at the beginning of the present section.

### C.1.4 Ionic contribution

The second term in the r.h.s of Eq. C.12 is the third derivative of the ion-ion contribution to the total energy, which is computed, as usual, using the Ewald sum technique [165]. The third derivative is

$$\begin{aligned} \frac{\partial^3 E^{\text{ion}}}{\partial u_{\mathbf{q},s,\alpha} \partial u_{\mathbf{q}',s',\beta} \partial u_{\mathbf{q}'',s'',\gamma}} = & \\ & \delta_{s',s''} Z_{s'} Z_s F_{\alpha,\beta,\gamma}(\mathbf{q}, \mathbf{t}_{s'} - \mathbf{t}_s) + \\ & \delta_{s'',s} Z_{s''} Z_{s'} F_{\alpha,\beta,\gamma}(\mathbf{q}', \mathbf{t}_{s''} - \mathbf{t}_{s'}) + \\ & \delta_{s,s'} Z_s Z_{s''} F_{\alpha,\beta,\gamma}(\mathbf{q}'', \mathbf{t}_s - \mathbf{t}_{s''}) - \\ & \delta_{s,s',s''} Z_s \sum_{\bar{s}} Z_{\bar{s}} F_{\alpha,\beta,\gamma}(\mathbf{0}, \mathbf{t}_s - \mathbf{t}_{\bar{s}}). \end{aligned} \quad (\text{C.16})$$

In Eq. C.16, we have written explicitly the dependence on the atomic ( $s,s',s''$ ) and Cartesian ( $\alpha,\beta,\gamma$ ) indexes of the phonon patterns  $u_{\mathbf{q}}$  (which are defined in Eq. 2.2). In Eq. C.16,  $Z_s$  is the ionic charge and  $\mathbf{t}_s$  is the position of the atom  $s$ . The sum is performed on all the atoms of the unit cell. The function  $F$  is

$$\begin{aligned} F_{\alpha,\beta,\gamma}(\mathbf{q}, \mathbf{t}) = & -\frac{4\pi}{\Omega} \sum_{\mathbf{G}} \left[ \frac{e^{-(\mathbf{G}+\mathbf{q})^2/(4\eta^2)}}{(\mathbf{G}+\mathbf{q})^2} e^{i(\mathbf{G}+\mathbf{q})\cdot\mathbf{t}} \times \right. \\ & \left. i^3 (\mathbf{G}+\mathbf{q})_{\alpha} (\mathbf{G}+\mathbf{q})_{\beta} (\mathbf{G}+\mathbf{q})_{\gamma} \right] + \\ & - \sum_{\mathbf{R}} e^{i\mathbf{q}\cdot\mathbf{R}} \left. \frac{d^3 f}{dx_{\alpha} dx_{\beta} dx_{\gamma}} \right|_{\mathbf{x}=\mathbf{t}-\mathbf{R}}. \end{aligned} \quad (\text{C.17})$$

Here,  $\Omega$  is the unit-cell volume, the sums are performed on the ensemble of the reciprocal lattice vectors  $\mathbf{G}$  and of the real space lattice vectors  $\mathbf{R}$ .  $\eta$  is the cutoff for the real space summation within the Ewald method [165] and  $f(\mathbf{x}) = \text{erfc}(\eta x)/x$ , being  $x = |\mathbf{x}|$ .  $\text{erfc}$  is the error function and

$$\begin{aligned} \frac{d^3 f(\mathbf{x})}{dx_{\alpha} dx_{\beta} dx_{\gamma}} = & (\delta_{\alpha\beta} x_{\gamma} + \delta_{\alpha\gamma} x_{\beta} + \delta_{\beta\gamma} x_{\alpha}) f_1(x) \\ & + x_{\alpha} x_{\beta} x_{\gamma} f_3(x) a(\eta x) \end{aligned} \quad (\text{C.18})$$

with

$$f_1(x) = \frac{3\text{erfc}(\eta x) + a(\eta x)(3 + 2x^2\eta^2)}{x^5}, \quad (\text{C.19})$$

$$f_3(x) = -\frac{15\text{erfc}(\eta x) + a(\eta x)(15 + 10\eta^2 x^2 + 4\eta^4 x^4)}{x^7}, \quad (\text{C.20})$$

$$a(\xi) = \frac{2\xi}{\sqrt{\pi}} e^{-\xi^2}. \quad (\text{C.21})$$

### C.1.5 Gradient corrected functionals

The last term of eq. C.12 has to be generalized in the case of gradient-corrected functionals to include the partial derivative with respect to the norm of the charge density gradient  $|\nabla_{\mathbf{r}} n(\mathbf{r})|$ . The explicit expression for this derivative is several pages long, it is reported in Ref. 166.

## C.1.6 Derivatives of the external potential

### C.1.6.1 Third derivative

The third right-hand term of Equation C.12 involves the third derivative of the external potential integrated with the unperturbed ground-state charge. For the local part we only give the final expression, as computed in reciprocal space on the basis of Cartesian displacements:

$$V_{\text{local}}^{(3)} \begin{pmatrix} \mathbf{q} & \mathbf{q}' & \mathbf{q}'' \\ I & J & K \\ \alpha & \beta & \gamma \end{pmatrix} = \delta_{I,J} \delta_{I,K} \times \Omega \left( \frac{2\pi}{a} \right)^3 \sum_{\mathbf{G}} n_{\mathbf{G}} i e^{i2\pi \mathbf{G} \cdot \boldsymbol{\tau}_I} G_{\alpha} G_{\beta} G_{\gamma} v_{ext}^{\mathbf{G}} \quad (\text{C.22})$$

Where the  $I$ th ion is at position  $\boldsymbol{\tau}$ . We recall that the external potential is a superposition of ion-centered ionic potentials.

As we are using non-local pseudopotentials, we have an additional term which comes from applying the pseudopotential projectors to the wavefunctions. We start from the expression of the non-local contribution to total energy[167]:

$$E_{\text{non-local}} = \sum_{\nu, \mu} \tilde{D}^{\nu, \mu} \sum_{i, \mathbf{k}} W_{\mathbf{k}} \tilde{\theta}(\varepsilon_{\mathbf{k}}^i) \langle \psi_{\mathbf{k}}^i | p_{\nu} \rangle \langle p_{\mu} | \psi_{\mathbf{k}}^i \rangle \quad (\text{C.23})$$

where  $|p_n\rangle$  is the  $n$ -th non-local projector, and  $\tilde{\theta}(\varepsilon)$  the smearing function in the metallic case.  $\tilde{D}^{\nu, \mu}$  are the non-local energy terms coming from projectors  $\nu$  and  $\mu$ ; these indexes are global, but in practice  $\tilde{D}^{\nu, \mu}$  is non-zero only when projectors  $\nu$  and  $\mu$  are centered on the same ion.

Its third order derivative can be computed directly; we found convenient to implement it numerically in reciprocal space. We define 4 integral terms, as computed in  $\mathbf{G}$ -space:

$$A_{\nu, i, \mathbf{k}}^{(3)\alpha\beta\gamma} = \langle \psi_{\mathbf{k}}^i | p_{\nu}^{\alpha\beta\gamma} \rangle = \left( \frac{2\pi}{a} \right)^3 \sum_{\mathbf{G}} G_{\alpha} G_{\beta} G_{\gamma} (p_{\nu})_{\mathbf{G}} (\psi_{\mathbf{k}}^i)_{\mathbf{G}}, \quad (\text{C.24})$$

$$A_{\nu, i, \mathbf{k}}^{(2)\alpha\beta} = \langle \psi_{\mathbf{k}}^i | p_{\nu}^{\alpha\beta} \rangle = \left( \frac{2\pi}{a} \right)^2 \sum_{\mathbf{G}} G_{\alpha} G_{\beta} (p_{\nu})_{\mathbf{G}} (\psi_{\mathbf{k}}^i)_{\mathbf{G}}, \quad (\text{C.25})$$

$$A_{\nu, i, \mathbf{k}}^{(1)\alpha} = \langle \psi_{\mathbf{k}}^i | p_{\nu}^{\alpha} \rangle = \frac{2\pi}{a} \sum_{\mathbf{G}} G_{\alpha} (p_{\nu})_{\mathbf{G}} (\psi_{\mathbf{k}}^i)_{\mathbf{G}}, \quad (\text{C.26})$$

$$A_{\nu, i, \mathbf{k}}^{(0)} = \langle \psi_{\mathbf{k}}^i | p_{\nu} \rangle = \sum_{\mathbf{G}} (p_{\nu})_{\mathbf{G}} (\psi_{\mathbf{k}}^i)_{\mathbf{G}}. \quad (\text{C.27})$$

Where  $|p^{\alpha}\rangle$  is the derivative of the Kleinman-Bylander (KB) projectors[167] along Cartesian direction  $\alpha$ ; multiple indexes indicate multiple derivatives. We have employed the notation  $(\psi)_{\mathbf{G}}$  to underline that function  $\psi$  is represented in Fourier space;  $(q)_{\alpha}$  indicates the Cartesian component  $\alpha = x, y, z$  of vector  $\mathbf{q}$ . With these definitions we have the contribution on the Cartesian basis:

$$V_{\text{non-local}}^{(3)} = -2 \sum_{\mathbf{k}} W_{\mathbf{k}} \sum_i \tilde{\theta}(\varepsilon_{\mathbf{k}}^i) \sum_{\nu, \mu} \tilde{D}^{\nu, \mu} \times \left( A_{\nu, i, \mathbf{k}}^{(3)\alpha\beta\gamma} A_{\mu, i, \mathbf{k}}^{(0)} + A_{\nu, i, \mathbf{k}}^{(1)\alpha} A_{\mu, i, \mathbf{k}}^{(2)\beta\gamma} + A_{\nu, i, \mathbf{k}}^{(1)\beta} A_{\mu, i, \mathbf{k}}^{(2)\gamma\alpha} + A_{\nu, i, \mathbf{k}}^{(1)\gamma} A_{\mu, i, \mathbf{k}}^{(2)\alpha\beta} \right) \quad (\text{C.28})$$

The dependence on the ion is implicit in the indexes  $\nu$  and  $\mu$ .

### C.1.7 Second derivative

This term is composed of a local and non-local part, similarly to the one treated in the previous section. For the local part we only give the final expression, as computed in reciprocal space on the basis of

Cartesian displacements:

$$V_{\text{local}}^{(3)} \begin{pmatrix} \mathbf{q} & \mathbf{q}' & \mathbf{q}'' \\ I & J & K \\ \alpha & \beta & \gamma \end{pmatrix} = -\frac{1}{2} \left( \frac{2\pi}{a} \right)^2 \sum_{\mathbf{G}} \delta_{I,J} \delta_{I,K} \left( n_{\mathbf{q},I,\alpha}^{(1)} \right)_{\mathbf{G}} \times e^{i2\pi(\mathbf{q}+\mathbf{G}) \cdot \boldsymbol{\tau}_J} (G+\mathbf{q})_{\beta} (G+\mathbf{q})_{\gamma} v_{ext}^{\mathbf{G}}. \quad (\text{C.29})$$

It's interesting to note that  $\mathbf{q}'$  and  $\mathbf{q}''$  never appears explicitly, but only summed together, this sum has been replaced with  $-\mathbf{q}$ .

We will also reuse the  $A^{(0)}$  term from the previous section, and define these additional terms:

$$d^{\mathbf{q}} A_{\nu,i,\mathbf{k}}^{(0)} = \sum_{\mathbf{G}} (p_{\nu})_{\mathbf{G}} (d^{\mathbf{q}} \psi_{\mathbf{k}}^i)_{\mathbf{G}} \quad (\text{C.30})$$

$$B_{\nu,i,\mathbf{k}}^{(2)\alpha\beta} = \left( \frac{2\pi}{a} \right)^2 \sum_{\mathbf{G}} (k+G)_{\alpha} (k+G)_{\beta} (p_{\nu})_{\mathbf{G}} (\psi_{\mathbf{k}}^i)_{\mathbf{G}}, \quad (\text{C.31})$$

$$B_{\nu,i,\mathbf{k}}^{(1)\alpha} = \frac{2\pi}{a} \sum_{\mathbf{G}} (k+G)_{\alpha} (p_{\nu})_{\mathbf{G}} (\psi_{\mathbf{k}}^i)_{\mathbf{G}}, \quad (\text{C.32})$$

$$d^{\mathbf{q}} B_{\nu,i,\mathbf{k}}^{(2)\alpha\beta} = \left( \frac{2\pi}{a} \right)^2 \sum_{\mathbf{G}} (k+q+G)_{\alpha} (k+q+G)_{\beta} \times (p_{\nu})_{\mathbf{G}} (d^{\mathbf{q}} \psi_{\mathbf{k}}^i)_{\mathbf{G}}, \quad (\text{C.33})$$

$$d^{\mathbf{q}} B_{\nu,i,\mathbf{k}}^{(1)\alpha} = \frac{2\pi}{a} \sum_{\mathbf{G}} (k+q+G)_{\alpha} (p_{\nu})_{\mathbf{G}} (d^{\mathbf{q}} \psi_{\mathbf{k}}^i)_{\mathbf{G}}, \quad (\text{C.34})$$

$$(\text{C.35})$$

With this notation the non-local contribution is:

$$V_{\text{non-local}}^{(3)} = 2 \sum_{\mathbf{k}} W_{\mathbf{k}} \sum_i \tilde{\theta}(\varepsilon_{\mathbf{k}\mathbf{k}}^i) \sum_{\nu,\mu} \tilde{D}^{\nu,\mu} \times \left( B_{\nu,i,\mathbf{k}}^{(1)\beta} d^{\mathbf{q}} B_{\mu,i,\mathbf{k}}^{(1)\gamma} + B_{\nu,i,\mathbf{k}}^{(1)\gamma} d^{\mathbf{q}} B_{\mu,i,\mathbf{k}}^{(1)\beta} + B_{\nu,i,\mathbf{k}}^{(2)\beta\gamma} d^{\mathbf{q}} A_{\mu,i,\mathbf{k}}^{(2)} + A_{\nu,i,\mathbf{k}}^{(0)} d^{\mathbf{q}} B_{\mu,i,\mathbf{k}}^{(2)\beta\gamma} \right) \quad (\text{C.36})$$

Where the first perturbation is implicit in  $d^{\mathbf{q}}\psi$ , and the ionic indexes are implicit in  $\mu$  and  $\nu$ .

### C.1.8 Non-linear core correction

$n_c(\mathbf{r})$  is the core charge. We consider  $n_t(\mathbf{r}) = n(\mathbf{r}) + n_c(\mathbf{r})$ , where  $n$  is the valence charge. First, in the last term in the right hand side of Eq. C.12, one has to replace the three  $\partial n / \partial u_{\mathbf{q}}$  with the corresponding  $\partial n_t / \partial u_{\mathbf{q}}$ . Second, one has to add in the right hand side of Eq. C.12 the two terms

$$\int \frac{\delta E_1[n]}{\delta n(\mathbf{r})} \frac{\partial^3 n_c(\mathbf{r})}{\partial u_{\mathbf{q}} \partial u_{\mathbf{q}'} \partial u_{\mathbf{q}''}} d\mathbf{r} + 3 \int \frac{\delta^2 E_1[n]}{\delta n(\mathbf{r}) \delta n(\mathbf{r}')} \frac{\partial^2 n_c(\mathbf{r})}{\partial u_{\mathbf{q}} \partial u_{\mathbf{q}'}} \frac{\partial^2 n_t(\mathbf{r}')}{\partial u_{\mathbf{q}''}} d\mathbf{r} d\mathbf{r}' \quad (\text{C.37})$$

### C.1.9 Variation of wavefunctions

In order to compute all the terms of equations C.12, C.13 and C.14 we need up to 12 distinct wavefunction variation terms:

$$\begin{aligned} & |\phi_{\mathbf{k}>,i}^{\mathbf{q}_1}\rangle, & |\phi_{\mathbf{k}-\mathbf{q}_1>,i}^{\mathbf{q}_1}\rangle, & |\phi_{\mathbf{k}+\mathbf{q}_1>,i}^{-\mathbf{q}_1}\rangle, & |\phi_{\mathbf{k}>,i}^{-\mathbf{q}_1}\rangle \\ & |\phi_{\mathbf{k}>,i}^{\mathbf{q}_2}\rangle, & |\phi_{\mathbf{k}-\mathbf{q}_2>,i}^{\mathbf{q}_2}\rangle, & |\phi_{\mathbf{k}+\mathbf{q}_2>,i}^{-\mathbf{q}_2}\rangle, & |\phi_{\mathbf{k}>,i}^{-\mathbf{q}_2}\rangle \\ & |\phi_{\mathbf{k}>,i}^{\mathbf{q}_3}\rangle, & |\phi_{\mathbf{k}-\mathbf{q}_3>,i}^{\mathbf{q}_3}\rangle, & |\phi_{\mathbf{k}+\mathbf{q}_3>,i}^{-\mathbf{q}_3}\rangle, & |\phi_{\mathbf{k}>,i}^{-\mathbf{q}_3}\rangle \end{aligned} \quad (\text{C.38})$$

Note that the first 2 and last 2 terms on each line are the same derivative, but they are computed on two different grids of electronic  $\mathbf{k}$  points. All of these wavefunction derivatives can be computed non-self consistently for the corresponding variation of the ground state charge  $\partial n/\partial \mathbf{u}(\mathbf{q})$ ; this is done in the code solving eq. C.7 with a conjugate-gradient (CG) algorithm. The symmetry operations in the G3S can be used to reduce the number of electronic  $\mathbf{k}$  points to be used for the BZ integration.

As a by-product of the CG algorithm we compute the following terms:

$$\langle \psi_{\mathbf{k}-\mathbf{q},i} | d^{\mathbf{q}} H | \psi_{\mathbf{k},j} \rangle \quad (\text{C.39})$$

$$\langle \psi_{\mathbf{k},i} | d^{\mathbf{q}} H | \psi_{\mathbf{k}-\mathbf{q},j} \rangle, \quad (\text{C.40})$$

for every  $\mathbf{q}$ : they are stored to be used later. We also compute additionally the terms of the form:

$$\langle \psi_{\mathbf{k}-\mathbf{q}_3,i} | d^{\mathbf{q}_2} H | \psi_{\mathbf{k}+\mathbf{q}_1,j} \rangle, \quad (\text{C.41})$$

for all the 6 permutations of the  $\mathbf{q}$ -vectors, as they are used in eq. C.13 and C.14.

In the metal case, we precompute some terms which are only used for eq. C.14:

$$\langle \phi_{\mathbf{k}-\mathbf{q}_a,i}^{\mathbf{q}_a} | d^{\mathbf{q}_b} H | \psi_{\mathbf{k}-\mathbf{q}_b,j} \rangle. \quad (\text{C.42})$$

Where  $\mathbf{q}_a$  and  $\mathbf{q}_b$  can be  $\mathbf{q}, \mathbf{q}', \mathbf{q}''$  or  $\mathbf{q}, \mathbf{q}', \mathbf{q}''$  and  $\mathbf{q}_a \neq \mathbf{q}_b, \mathbf{q}_a \neq -\mathbf{q}_b$ .

In order to save cpu time we employ every possible simplification in special cases. The first special case is trivially  $\mathbf{q} = \mathbf{q}' = \mathbf{q}'' = \Gamma$ , in this case only one wavefunction derivative is needed, only one unique term arises from eq. C.39.

The second special case is  $\mathbf{q} = \Gamma$  and  $\mathbf{q}' = -\mathbf{q}'' = \mathbf{p}$ ; in this case we need 3 derivatives, the first  $|\phi_{\mathbf{k}}^{\Gamma}\rangle$  comes from the first line of eq. C.38, the second  $|\phi_{\mathbf{k}}^{\mathbf{p}}\rangle$  and third  $|\phi_{\mathbf{k}-\mathbf{p}}^{\mathbf{p}}\rangle$  come from the first two terms of the second line. There are more unique terms from eq. C.38 that could be computed, but they are not needed to obtain  $D^3$ . Only in the specific case for metal when at least one of the 3 points is zero, we precompute one additional term:

$$\langle \phi_{\mathbf{k},i}^{\mathbf{p}} | d^{\mathbf{p}} H | \psi_{\mathbf{k},j} \rangle. \quad (\text{C.43})$$

In order obtain  $D^3$  using only three derivatives, we cannot compute all the 6 permutation of eq. C.11: only 3 of them are done explicitly, the other ones are obtained by index permutation and complex conjugate:

$$\tilde{E} \begin{pmatrix} \Gamma & \mathbf{p} & -\mathbf{p} \\ s & s' & s'' \end{pmatrix} = \left( \tilde{E} \begin{pmatrix} \Gamma & -\mathbf{p} & \mathbf{p} \\ s & s'' & s' \end{pmatrix} \right)^* \quad (\text{C.44})$$

And so on, pairwise, for the other terms. It is important to choose wisely the terms to compute and those to obtain by permutation in order to use only 3 derivatives; the choice depends on the specific details and internal conventions of the implementation but is evident in practice. Accordingly if the vanishing vector is  $\mathbf{q}'$  or  $\mathbf{q}''$ , the same technique can be applied with only minor changes.

The last special case is  $\mathbf{q} = 2\mathbf{p}$  and  $\mathbf{q}' = \mathbf{q}'' = -\mathbf{p}$ . In this case we can reduce the total number of wavefunction derivatives to 7. We omit the details, that are quite similar to the previous case.

## C.2 Third-order response calculation

A third order calculation in the “2n+1” method is performed of 4 consecutive stages.

1. a ground state self-consistent field calculation. Results: ground state density  $n(\mathbf{r})$  self consistent Kohn-Sham potential  $V^{\text{KS}}$ .
2. DFPT (phonon) calculation on a symmetry-reduced grid  $\mathbf{q}$  points. Results: first-order variation of the ground state density  $\partial n/\partial u_{\mathbf{q}}$  and of the potential  $V^{\mathbf{q}}$  for an irreducible set of bf  $\mathbf{q}$  points.
3. rotation of the charge density variation to a complete regular grid of  $\mathbf{q}$  points. Results:  $\partial n/\partial u_{\mathbf{q}}$  on the complete regular bf  $\mathbf{q}$ -space grid.

4. the third-order response calculation. Results: the third-order dynamical matrix  $D_{\mathbf{q},\mathbf{q}',\mathbf{q}''}^3$ , for every triplet  $\mathbf{q}, \mathbf{q}', \mathbf{q}''$ .

In step 4, the  $|\psi_{\mathbf{k}}\rangle$  are computed non-self consistently from the ground state charge density  $n$ , while  $|\phi_{\mathbf{k}}^{\mathbf{q}}\rangle$  are recomputed from  $n(\mathbf{r})$  and its perturbation  $\delta^{\mathbf{q}}n$ .

The main limits of the current implementation is that only norm-conserving pseudopotential can be used and that only the plain local-density approximation is supported for the functional. The second and third steps can either be performed in a single run or in two consecutive runs. The former is simpler and tidier to run, the latter allows for a better optimisation of memory usage: Step 2 is cpu intensive while step 3 is memory and input/output intensive. The last step is performed by our the new generalized 3rd order code.

### C.2.1 Parallelism and computational cost

Each  $\mathbf{q}$  vector of steps 2 and 3 can be computed independently, allowing for a very effective parallelisation: provided that an illimited number of CPUs are available the total wall time is just the wall time of the slower  $\mathbf{q}$  point. The same holds for step 4, if we consider  $\mathbf{q}$  point triplets instead of single points.

Apart from this trivial parallelisation, two more levels of parallelism are implemented in the code; they correspond to the *k-point pools* and *plane-wave* parallelisation of Quantum-ESPRESSO as described in detail in Ref. 105.

The computational cost of a single triplet calculation is of the same order of magnitude of a phonon calculation for a  $\mathbf{q}$  point of the same symmetry. However, the double-grid of triplets is contains many more points than single-grid of  $\mathbf{q}$  points, as we will see in detail in Section B.6. Consequently the amount of CPU time required to perform the third order calculation is much larger than for the phonon calculation. As an example, in the graphene case, The 2nd order calculation over the  $N_{\text{ph}} = 10$  irreducible  $\mathbf{q}$  points took about 15 h of CPU time to complete; the 3rd calculation includes  $N_{\text{d3}} = 88$  triplets that were computed in 1800 h. For the calculations performed in this work, the most CPU intensive part of the 3rd order calculation is then on-self consistent calculation of the wavefunction variations.

On the other hand, the cost of this response calculation is rarely a bottleneck, as the solution of the Boltzmann transport equation tends to be an order of magnitude more expensive.

# Appendix D

## Description of computer codes

The theory described in the previous chapters has been implemented over the course of a decade in a series of computer codes to perform the calculations. This appendix reprises the user manual to describes the use and parameters of the different codes and show their capabilities.

*This section is adapted from the documentation of the “anharmonic” code release. The codes and the full documentation are available at their official web page [168].*

### D.1 Electronic structure code

The `d3q.x` code computes the third derivative of the Density Functional Theory ground-state energy with respect to three harmonic perturbations, identified by their wavevectors  $q_1$ ,  $q_2$  and  $q_3 = -q_1 - q_2$ . The code can use a certain number of methods:

- Norm Conserving pseudopotentials
- Local Density Approximation (LDA) and Generalized Gradient Approximation (GGA) functionals.
- Insulators and Metals (i.e. partial occupation of the electronic bands)

On the other hand, the codes *does not* implements the following features:

- Ultrasoft pseudopotentials and PAW datasets
- Advanced functionals, e.g. meta-GGA, Grimme vdW corrections and non-local vdW functionals
- Hybrid functionals
- LDA+U, or self-interaction correction
- spin-polarized systems
- non-collinear spin and spin-orbit interaction

In most cases, we have have been able to obtain meaningful results despite these limitation, sometimes combining phonons computed with more advanced methods with 3rd order calculation computed on the same systems but with a simpler method, assuming that more advanced correction would not affect the 3rd order too much. If you want to take this approach we recommend that you validate the assumption on a simpler test, where the entire calculation can be performed with the methods available in `d3q.x`. Alternatively, you can use one of the compatible real-space codes.

The `d3q.x` code works in combination with the `ph.x` code from the Quantum ESPRESSO distribution, which in turn has to be run on top of a total energy calculation performed with the `pw.x` code. As it is impractical to store the wavefunctions and the wavefunction perturbations, the `d3q.x` code recomputes them from the ground-state charge density and its variation with respect to a harmonic phonon perturbation.

## D.2 Utilities

### **d3\_sqom.x**

This code reads a spectral weight file from `d3_1w.x` and manipulates it to simulate the effect of limited experimental resolution, from Inelastic Neutron Scattering or Inelastic X-ray Scattering.

It computes the convolution with a Lorentzian (INS) or Pseudo-voigt (IXS) function that has an energy-dependent (INS) or fixed (IXS) full-width-half maximum. This code can also sum and average the spectral function coming from several different files, to simulate the uncertainty of the neutron wavevectors.

### **d3\_q2r.x**

This code is analogous to the `q2r.x` code of QE, and it uses the same input, but produces a file of Force Constants (FCs) which has already been re-centered in the reciprocal space Wigner-Seitz cell to make Fourier Interpolation faster.

In addition to the standard `q2r` variables, you can specify “`nfar`” which is the distance from the origin, in unit cells, used to construct the first Brillouin zone. Setting `nfar` to a sufficiently large number (i.e. 2 or 3) produces “centered” force constants, useful for Fourier interpolation. Setting `nfar=0` produces standard “periodic” force constants that can be directly compared with the ones from Quantum ESPRESSO.

### **d3\_qq2rr.x**

Analogous to `q2r.x`, but operates on the 3rd order matrices. This code also applies the symmetry by permutation of the indices, which is not completely taken into account by the `d3q.x` code.

### **d3\_sparse.x**

This code converts a file of third order FCs from dense form to sparse form; it can optionally discard elements that are smaller than a custom threshold. It can also measure the speedup gained by using the sparse FCs instead of the dense ones.

### **d3\_asr3.x**

This code applies the acoustic sum rules (ASR) to the third order FCs. It can only work on dense FCs, not on the sparse ones. As the sum is applied iteratively, it will automatically stop after 10,000 iterations, or when the residual violation of the ASR is less than  $10^{-12}$ .

### **d3\_recenter.x**

Reads force constants from `mat3R.input`, interpolate them on a grid of  $NQX \times NQY \times NQZ$  points, recenter them on a Wigner-Seitz cell constructed up to `NFAR` unit cells and save the result.

Uses the properties of Fourier interpolation to convert the 3rd order force constants from a grid to another. If the new grid is different than the initial one, some interpolation will be done, if the grid is the same, you can use the `nfar` parameter to recalculate the Wigner-Seitz cell centering.

### **d3\_import\_shengbte.x**

Reads the 3-body force constants produced by Mingo & Carrete code `thirdorder.py` [21] and import them to internal format.

## D.3 Main codes

### D.3.1 **d3\_r2q.x**

This code reads the 2nd order FCs and computes a number of different quantities that only depend on the harmonic 2nd order force constants, it is currently evolving and should be quite easy to modify and extend according to your needs.

The type of calculation this code can perform are:

- “freq”: Compute the phonon frequencies.
- “jdos”: Compute the joint density of state as defined in Ref. 107.
- “rms” : Compute the root mean square displacement of the atoms around their equilibrium positions in the harmonic hamiltonian at a given temperature.
- “fh”: Compute the phonon free energy or, for  $T=0$ , the zero-point energy.

### D.3.2 d3\_qha.x

This code is an implementation of the well known Quasi Harmonic Approximation method to find crystals equilibrium volume at finite temperature, and thermal expansion.

It reads the 2nd order FCs for a series of volumes and computes the phonon free energy for a given list of temperature, optionally adding a pV (pressure  $\times$  volume) hydrostatic term. It then fits the total free energy with an equation of state to find the equilibrium volume at each temperature, and find the temperature/volume curve and the volumetric thermal expansion coefficient.

Optionally one can add an hydrostatic pressure, which will contribute a simple -pV term to the total energy.

Kind of equation of state to use:

1. Murnaghan
2. Birch 1st order
3. Birch 3rd order
4. Keane

Note that these EOS are empirically suitable for V-P (volume-pressure) curves, not for V-T. In practice they work remarkably well in all the cases we have tested.

### D.3.3 d3\_lw.x

This code can compute the intrinsic phonon-phonon interaction and the interaction of phonons with isotopic disorder and border scattering at any  $\mathbf{q}$ -point.

The quantities to compute that are currently implemented:

- “lw imag”: compute the imaginary part of the self-energy, i.e. the phonon linewidth. In this mode the code will enforce conservation of energy with a Diract delta function approximated with a Gaussian function of width delta, read from input.
- “lw full”: compute the entire self energy, the real part is the lineshift and the imaginary part is the linewidth. In this case the value of delta will be used as a regularization for the self-energy.
- “spf full”: compute the spectra function, also known as  $\sigma(\omega)$ , for a list of energies and of q-points.
- “spf imag”: as “spf full”, but only the imaginary part of the self-energy will be used, i.e. the spectra function will be centered around the non-shifted phonon energy. This is often in better agreement with experiments than “spf full”, unless you also include somehow the 4-phonons self-energy contribution, because the real part of the 3-phonon term and the 4-phonon terms tend to cancel each other out.
- “spf simple”: simulate the spectral function as a superposition of Lorentzian functions centered around the phonon frequencies and appropriate width. This is a good approximation to “spf full” when the anharmonicity is very weak.
- “final”: decompose the contribution to the linewidth at a specific energy and q-point (specified in input) over the energy of the final states involved in the scattering process or over the final q, or both.

This code can also take into account scattering from isotopic disorder. A table of natural occuring isotopes is included in the code, or can be specified by hand. It is also possible to include scattering with boundary, treated with the Casimir formula. Isotopes and Casimir scattering is only applied to linewidth calculation, it has no effect on spectral function and final state calculations.

### D.3.4 d3\_tk.x

The `d3_tk.x` code can compute the thermal conductivity coefficient in the SMA or by exact diagonalization of the BTE. It uses the same routines for computing the phonon lifetime as the `d3_lw.x` code and has the same capabilities for including extrinsic effects (isotopes, boundaries).

The “cgp” algorithm will also output the SMA thermal conductivity at its first iteration, but computed in a slightly different way which is slower but guarantees the phonon-phonon scattering matrix to be well defined and the functional to be minimized to be positive definite.

When doing a “sma” calculation, the phonon lifetime has to be computed, for each  $\mathbf{k}$ -point in a. Each lifetime calculation is itself an integral over a

inner  $\mathbf{k}$ -points grid. In principle, there is no reason for the two grids to be identical, as one quantity could be harder to converge than the other. When doing a CGP calculation, the inner and outer grids must be identical, as the algorithm diagonalizes a matrix  $A$  which contains the scattering probability of every phonon with any other, this contributes to the increased computational cost of the CGP method.

### D.3.5 d3\_tdph.x

This code implements the TDEP method. It reads a set of initial dynamical matrices for a given system and optimizes the harmonic force constants over a series of images that can be the output of a molecular dynamics calculation performed with Quantum ESPRESSO, or of a Langevin Dynamics calculation from the PIOUD code. The code will expect that the simulation supercell is the same for the force constants and the dynamics simulations.

When building the basis of symmetric dynamical matrices, use one of these initial guesses:

- “simple” orthogonal matrices hermitean matrices with a single diagonal or two non-diagonal non-zero elements
- “mu” from the eigenvectors of the original dynamical matrices, from file `_mat2`, discard the acoustic modes at  $q = 0$ .
- “random” start from random matrices (rarely works because of accidental degeneracies)

When minimizing the phonon parameters, use one of these methods:

- “ph” only minimize the phonon degrees of freedom
- “ph+zstar” first minimize the phonons, then the effective charges degrees of freedom. It gives rarely any improvement over “ph” because the effective charges do not depend strongly on temperature.
- “global” minimize all degrees of freedom simultaneously, this method can (and often does) produce unphysical solution if the supercell is not huge.

## D.4 Experimental codes:

### d3\_db.x

Uses the ansatz of Ref. 169 to apply the anharmonic correction directly to the dynamical matrix (instead of perturbing just the phonon energy). Can be used to obtain 3rd-order corrected matrices that can be interpolated using standard techniques.

# Bibliography

- [1] P. Hohenberg and W. Kohn. “Inhomogeneous Electron Gas”. In: *Phys. Rev.* 136 (3B Nov. 1964), B864–B871 (page 1).
- [2] W. Kohn and L. J. Sham. “Self-Consistent Equations Including Exchange and Correlation Effects”. In: *Phys. Rev.* 140 (4A Nov. 1965), A1133–A1138 (page 1).
- [3] J. P. Perdew and A. Zunger. “Self-interaction correction to density-functional approximations for many-electron systems”. In: *Phys. Rev. B* 23 (1981), p. 5048 (page 1).
- [4] J.P. Perdew, K. Burke, and M. Ernzerhof. “Generalized Gradient Approximation Made Simple”. In: *Phys. Rev. Lett.* 77 (1996), p. 3865 (page 1).
- [5] P.G. Klemens. Ed. by F. Seitz and D. Turnbull. *Solid State Physics*. Academic Press, New York, 1958 (page 1).
- [6] R Berman, F. E. Simon, and J. S. Ziman. “The thermal conductivity of diamond at low temperatures”. In: *Proceedings of the Royal Society of London A: Mathematical, Physical and Engineering Sciences* 220.1141 (1953), pp. 171–183 (pages 1, 31).
- [7] Max Born and K. Huang. *Dynamical Theory of Crystal Lattices*. Oxford: Oxford University Press, 1954 (page 1).
- [8] P. D. De Cicco and F. A. Johnson. In: *Proc. R. Soc. London Ser. A* 310 (1969) (page 1).
- [9] Robert M. Pick, Morrel H. Cohen, and Richard M. Martin. “Microscopic Theory of Force Constants in the Adiabatic Approximation”. In: *Phys. Rev. B* 1 (2 Jan. 1970), pp. 910–920 (page 1).
- [10] Stefano Baroni, Paolo Giannozzi, and Andrea Testa. “Green’s-function approach to linear response in solids”. In: *Phys. Rev. Lett.* 58 (18 May 1987), pp. 1861–1864 (page 1).
- [11] Stefano Baroni, Paolo Giannozzi, and Andrea Testa. “Elastic Constants of Crystals from Linear-Response Theory”. In: *Phys. Rev. Lett.* 59 (23 Dec. 1987), pp. 2662–2665 (page 1).
- [12] P. Debye. “Zur Theorie der spezifischen Wärmen”. In: *Annalen der Physik* 344.14 (1912), pp. 789–839 (page 1).
- [13] R. Peierls. In: *Annals of Physics* 3 (1929), p. 1066 (page 1).
- [14] C. A. Ratsifaritana and P. G. Klemens. “Scattering of phonons by vacancies”. In: *International Journal of Thermophysics* 8.6 (Nov. 1987), pp. 737–750 (pages 1, 32, 36).
- [15] A. Sparavigna. “Influence of isotope scattering on the thermal conductivity of diamond”. In: *Phys. Rev. B* 65 (6 Jan. 2002), p. 064305 (pages 1, 31).
- [16] M Omini and A Sparavigna. “An iterative approach to the phonon Boltzmann equation in the theory of thermal conductivity”. In: *Physica B: Condensed Matter* 212.2 (1995), pp. 101–112 (pages 1, 31, 32).
- [17] Xavier Gonze and J-P Vigneron. “Density-functional approach to nonlinear-response coefficients of solids”. In: *Physical Review B* 39.18 (1989), p. 13120 (page 2).
- [18] Alberto Debernardi, Stefano Baroni, and Elisa Molinari. “Anharmonic Phonon Lifetimes in Semiconductors from Density-Functional Perturbation Theory”. In: *Phys. Rev. Lett.* 75 (9 Aug. 1995), pp. 1819–1822 (page 2).
- [19] G. Deinzer, G. Birner, and D. Strauch. “*Ab initio* calculation of the linewidth of various phonon modes in germanium and silicon”. In: *Phys. Rev. B* 67 (14 Apr. 2003), p. 144304 (page 2).

- [20] D. A. Broido, M. Malorny, G. Birner, Natalio Mingo, and D.A. Stewart. “Intrinsic lattice thermal conductivity of semiconductors from first principles”. In: *Applied Physics Letters* 91.23 (2007), pp. 231922–231922–3 (page 2).
- [21] Wu Li, Jesús Carrete, Nebil A. Katcho, and Natalio Mingo. “ShengBTE: a solver of the Boltzmann transport equation for phonons”. In: *Comp. Phys. Commun.* 185 (2014), pp. 1747–1758 (pages 2, 62).
- [22] Atsushi Togo and Isao Tanaka. “First principles phonon calculations in materials science”. In: *Scripta Materialia* 108 (2015), pp. 1–5 (page 2).
- [23] Jivtesh Garg, Nicola Bonini, Boris Kozinsky, and Nicola Marzari. “Role of Disorder and Anharmonicity in the Thermal Conductivity of Silicon-Germanium Alloys: A First-Principles Study”. In: *Phys. Rev. Lett.* 106 (4 Jan. 2011), p. 045901 (pages 2, 5, 17).
- [24] Nicola Bonini, Jivtesh Garg, and Nicola Marzari. “Acoustic Phonon Lifetimes and Thermal Transport in Free-Standing and Strained Graphene”. In: *Nano Letters* 12.6 (2012). PMID: 22591411, pp. 2673–2678 (pages 2, 20, 22, 27).
- [25] Lorenzo Paulatto, Francesco Mauri, and Michele Lazzeri. “Anharmonic properties from a generalized third-order ab initio approach: Theory and applications to graphite and graphene”. In: *Phys. Rev. B* 87 (21 June 2013), p. 214303 (pages 2, 7, 16, 31, 32, 53).
- [26] M. Omini and A. Sparavigna. “Heat transport in dielectric solids with diamond structure”. In: *Il Nuovo Cimento D* 19.10 (1997), p. 1537 (page 3).
- [27] M. Omini and A. Sparavigna. “Beyond the isotropic-model approximation in the theory of thermal conductivity”. In: *Phys. Rev. B* 53 (14 Apr. 1996), pp. 9064–9073 (page 3).
- [28] A. Sparavigna. “Lattice thermal conductivity in cubic silicon carbide”. In: *Phys. Rev. B* 66 (17 Nov. 2002), p. 174301 (page 3).
- [29] G. Fugallo, M. Lazzeri, L. Paulatto, and F. Mauri. “Ab initio variational solution for lattice thermal conductivity in diamond”. In: *Arxiv preprint cond-mat.mtrl-sci, submitted PRB* (2013) (pages 3, 7).
- [30] Andrea Cepellotti, Giorgia Fugallo, Lorenzo Paulatto, Michele Lazzeri, Francesco Mauri, and Nicola Marzari. “Phonon hydrodynamics in two-dimensional materials”. In: *Nature Communications* 6 (Mar. 2015). Article, p. 6400 (pages 3, 7, 8).
- [31] Andrea Cepellotti and Nicola Marzari. “Thermal Transport in Crystals as a Kinetic Theory of Relaxons”. In: *Phys. Rev. X* 6 (4 Oct. 2016), p. 041013 (page 3).
- [32] Michele Simoncelli, Nicola Marzari, and Francesco Mauri. “Unified theory of thermal transport in crystals and glasses”. In: *Nature Physics* 15.8 (May 2019), pp. 809–813 (pages 3, 31).
- [33] Alan JH McGaughey and Jason M Larkin. “Predicting phonon properties from equilibrium molecular dynamics simulations”. In: *Annual review of heat transfer* 17 (2014) (pages 3, 39).
- [34] T Gaskell. “Velocity autocorrelation function and diffusion coefficient in a liquid”. In: *Journal of Physics C: Solid State Physics* 4.12 (Aug. 1971), pp. 1466–1478 (pages 3, 39).
- [35] Nico de Koker. “Thermal conductivity of MgO periclase from equilibrium first principles molecular dynamics”. In: *Physical Review Letters* 103.12 (2009), p. 125902 (pages 3, 39).
- [36] Dong-Bo Zhang, Tao Sun, and Renata M Wentzcovitch. “Phonon quasiparticles and anharmonic free energy in complex systems”. In: *Physical review letters* 112.5 (2014), p. 058501 (page 3).
- [37] Tommaso Morresi, Lorenzo Paulatto, Rodolphe Vuilleumier, and Michele Casula. “Probing anharmonic phonons by quantum correlators: A path integral approach”. In: *The Journal of Chemical Physics* 154.22 (2021), p. 224108 (pages 3, 4, 6, 39, 42, 43).
- [38] Lorenzo Monacelli, Michele Casula, Kosuke Nakano, Sandro Sorella, and Francesco Mauri. *Quantum phase diagram of high-pressure hydrogen*. 2022 (pages 3, 39).

- [39] Ambroise van Roekeghem, Jesús Carrete, and Natalio Mingo. “Anomalous thermal conductivity and suppression of negative thermal expansion in ScF 3”. In: *Physical Review B* 94.2 (2016), p. 020303 (pages 3, 40).
- [40] Ambroise van Roekeghem, Jesús Carrete, and Natalio Mingo. “Quantum self-consistent ab-initio lattice dynamics”. In: *Computer Physics Communications* 263 (2021), p. 107945 (pages 3, 40).
- [41] Ion Errea, Matteo Calandra, and Francesco Mauri. “Anharmonic free energies and phonon dispersions from the stochastic self-consistent harmonic approximation: Application to platinum and palladium hydrides”. In: *Physical Review B* 89.6 (2014), p. 064302 (pages 3, 4, 40).
- [42] Terumasa Tadano and Shinji Tsuneyuki. “Self-consistent phonon calculations of lattice dynamical properties in cubic SrTiO<sub>3</sub> with first-principles anharmonic force constants”. In: *Phys. Rev. B* 92 (5 Aug. 2015), p. 054301 (pages 3, 39, 40).
- [43] Keivan Esfarjani and Harold T Stokes. “Method to extract anharmonic force constants from first principles calculations”. In: *Physical Review B* 77.14 (2008), p. 144112 (pages 3, 40).
- [44] Olle Hellman, IA Abrikosov, and SI Simak. “Lattice dynamics of anharmonic solids from first principles”. In: *Physical Review B* 84.18 (2011), p. 180301 (pages 3, 4, 40).
- [45] Olle Hellman, Peter Steneteg, Igor A Abrikosov, and Sergei I Simak. “Temperature dependent effective potential method for accurate free energy calculations of solids”. In: *Physical Review B* 87.10 (2013), p. 104111 (pages 3, 40).
- [46] Ibrahim Buba Garba, Michele Casula, and Lorenzo Paulatto. “Comparison of phonon renormalization methods.” In: *prep.* (2023) (pages 4, 42).
- [47] Michele Ceriotti, Michele Parrinello, Thomas E Markland, and David E Manolopoulos. “Efficient stochastic thermostatting of path integral molecular dynamics”. In: *The Journal of chemical physics* 133.12 (2010), p. 124104 (pages 4, 5, 42).
- [48] Lorenzo Paulatto, Ion Errea, Matteo Calandra, and Francesco Mauri. “First-principles calculations of phonon frequencies, lifetimes, and spectral functions from weak to strong anharmonicity: The example of palladium hydrides”. In: *Phys. Rev. B* 91 (5 Feb. 2015), p. 054304 (pages 4, 8, 16, 27).
- [49] Paola Giura, Lorenzo Paulatto, Fei He, Ricardo P. S. M. Lobo, Alexei Bosak, Eugenio Calandrini, Luigi Paolasini, and Daniele Antonangeli. “Multiphonon anharmonicity of MgO”. In: *Phys. Rev. B* 99 (22 June 2019), p. 220304 (pages 4, 9, 10, 43).
- [50] Saadi Chabane, Lorenzo Paulatto, Daniele Antonangeli, and Paola Giura. “Study of competing anharmonic processes in MgO at Earth crust conditions.” In: *prep.* (2023) (pages 4, 10).
- [51] Raffaele Resta. “Macroscopic polarization in crystalline dielectrics: the geometric phase approach”. In: *Rev. Mod. Phys.* 66 (3 July 1994), pp. 899–915 (page 4).
- [52] Aris Marcolongo, Paolo Umari, and Stefano Baroni. “Microscopic theory and quantum simulation of atomic heat transport”. In: *Nature Physics* 12.1 (Oct. 2015), pp. 80–84 (pages 4, 43).
- [53] Christian Carbogno, Rampi Ramprasad, and Matthias Scheffler. “Ab Initio Green-Kubo Approach for the Thermal Conductivity of Solids”. In: *Phys. Rev. Lett.* 118 (17 Apr. 2017), p. 175901 (page 4).
- [54] Alessandro Laio and Michele Parrinello. “Escaping free-energy minima”. In: *Proceedings of the National Academy of Sciences* 99.20 (2002), pp. 12562–12566 (page 4).
- [55] Antoine Dewandre, Olle Hellman, Sandip Bhattacharya, Aldo H. Romero, Georg K. H. Madsen, and Matthieu J. Verstraete. “Two-Step Phase Transition in SnSe and the Origins of its High Power Factor from First Principles”. In: *Phys. Rev. Lett.* 117 (27 Dec. 2016), p. 276601 (page 4).

- [56] Unai Aseginolaza, Raffaello Bianco, Lorenzo Monacelli, Lorenzo Paulatto, Matteo Calandra, Francesco Mauri, Aitor Bergara, and Ion Errea. “Phonon Collapse and Second-Order Phase Transition in Thermoelectric SnSe”. In: *Phys. Rev. Lett.* 122 (7 Feb. 2019), p. 075901 (page 4).
- [57] Yong Lu, Fa-wei Zheng, Yu Yang, Ping Zhang, and Dong-Bo Zhang. “Phase stabilities of *Cmcm* and *Pnma* SnSe studied by phonon quasiparticle approach”. In: *Phys. Rev. B* 100 (5 Aug. 2019), p. 054304 (page 4).
- [58] R. Zwanzig. *Nonequilibrium Statistical Mechanics*. Oxford: Oxford University Press, 2001 (page 4).
- [59] Giovanni Bussi and Michele Parrinello. “Accurate sampling using Langevin dynamics”. In: *Phys. Rev. E* 75 (5 May 2007), p. 056707 (page 5).
- [60] Jianshu Cao and Gregory A. Voth. “The formulation of quantum statistical mechanics based on the Feynman path centroid density. I. Equilibrium properties”. In: *The Journal of Chemical Physics* 100.7 (1994), pp. 5093–5105 (page 5).
- [61] Ian R. Craig and David E. Manolopoulos. “Quantum statistics and classical mechanics: Real time correlation functions from ring polymer molecular dynamics”. In: *The Journal of Chemical Physics* 121.8 (2004), pp. 3368–3373 (page 5).
- [62] Michele Ceriotti, David E Manolopoulos, and Michele Parrinello. “Accelerating the convergence of path integral dynamics with a generalized Langevin equation”. In: *The Journal of chemical physics* 134.8 (2011), p. 084104 (pages 5, 42).
- [63] Davide Campi, Lorenzo Paulatto, Giorgia Fugallo, Francesco Mauri, and Marco Bernasconi. “First-principles calculation of lattice thermal conductivity in crystalline phase change materials: GeTe,  $\text{Sb}_2\text{Te}_3$ , and  $\text{Ge}_2\text{Sb}_2\text{Te}_5$ ”. In: *Phys. Rev. B* 95 (2 Jan. 2017), p. 024311 (pages 5, 13).
- [64] Thuy-Quynh Duong, Assil Bouzid, Carlo Massobrio, Guido Ori, Mauro Boero, and Evelyne Martin. “First-principles thermal transport in amorphous  $\text{Ge}_2\text{Sb}_2\text{Te}_5$  at the nanoscale”. In: *RSC Adv.* 11 (18 2021), pp. 10747–10752 (page 5).
- [65] L. Bellaiche and David Vanderbilt. “Virtual crystal approximation revisited: Application to dielectric and piezoelectric properties of perovskites”. In: *Phys. Rev. B* 61 (12 Mar. 2000), pp. 7877–7882 (page 5).
- [66] G Bouzerar, S Thébaud, S Pecorario, and Ch Adessi. “Drastic effects of vacancies on phonon lifetime and thermal conductivity in graphene”. In: *Journal of Physics: Condensed Matter* 32.29 (Apr. 2020), p. 295702 (page 5).
- [67] Evgeny Plekhanov, Zelong Zhao, Francesco Macheda, Yao Wei, Nicola Bonini, and Cedric Weber. “Computational materials discovery for lanthanide hydrides at high pressure for high temperature superconductivity”. In: *Phys. Rev. Research* 4 (1 Mar. 2022), p. 013248 (page 5).
- [68] Boeri Lilia, Richard Hennig, Peter Hirschfeld, Gianni Profeta, Antonio Sanna, Eva Zurek, Warren E Pickett, Maximilian Amsler, Ranga Dias, Mikhail I Erements, Christoph Heil, Russell J Hemley, Hanyu Liu, Yanming Ma, Carlo Pierleoni, Aleksey N Kolmogorov, Nikita Rybin, Dmitry Novoselov, Vladimir Anisimov, Artem R Oganov, Chris J Pickard, Tiange Bi, Ryotaro Arita, Ion Errea, Camilla Pellegrini, Ryan Requist, E K U Gross, Elena Roxana Margine, Stephen R Xie, Yundi Quan, Ajinkya Hire, Laura Fanfarillo, G R Stewart, J J Hamlin, Valentin Stanev, Renato S Gonnelli, Erik Piatti, Davide Romanin, Dario Daghero, and Roser Valenti. “The 2021 room-temperature superconductivity roadmap”. In: *Journal of Physics: Condensed Matter* 34.18 (Mar. 2022), p. 183002 (page 5).
- [69] Lorenzo Monacelli, Ion Errea, Matteo Calandra, and Francesco Mauri. “Pressure and stress tensor of complex anharmonic crystals within the stochastic self-consistent harmonic approximation”. In: *Phys. Rev. B* 98 (2 July 2018), p. 024106 (page 6).

- [70] M. Martinez, M.-P. Gageot, D. Borgis, and R. Vuilleumier. “Extracting effective normal modes from equilibrium dynamics at finite temperature”. In: *The Journal of Chemical Physics* 125.14 (2006), p. 144106 (page 6).
- [71] Bernard R. Brooks, Dušanka Janežič, and Martin Karplus. “Harmonic analysis of large systems. I. Methodology”. In: *Journal of Computational Chemistry* 16.12 (1995), pp. 1522–1542 (page 6).
- [72] A. A. Balandin, S. Ghosh, D. L. Nika, and E. P. Pokatilov. “Thermal Conduction in Suspended Graphene Layers”. In: *Fullerenes, Nanotubes and Carbon Nanostructures* 18.4-6 (2010), pp. 474–486 (page 7).
- [73] Alexander A. Balandin. “Thermal properties of graphene and nanostructured carbon materials”. In: *Nature Materials* 10 (8 Aug. 2011), pp. 569–581 (page 7).
- [74] Giorgia Fugallo, Andrea Cepellotti, Lorenzo Paulatto, Michele Lazzeri, Nicola Marzari, and Francesco Mauri. “Thermal Conductivity of Graphene and Graphite: Collective Excitations and Mean Free Paths”. In: *Nano Letters* 14.11 (2014). PMID: 25343716, pp. 6109–6114 (pages 7, 32).
- [75] S. Huberman, R. A. Duncan, K. Chen, B. Song, V. Chiloyan, Z. Ding, A. A. Maznev, G. Chen, and K. A. Nelson. “Observation of second sound in graphite at temperatures above 100 K”. In: *Science* 364.6438 (2019), pp. 375–379 (page 7).
- [76] Zhiwei Ding, Ke Chen, Bai Song, Jungwoo Shin, Alexei A. Maznev, Keith A. Nelson, and Gang Chen. “Observation of second sound in graphite over 200 K”. In: *Nature Communications* 13.1 (Jan. 2022) (page 7).
- [77] Maxime Markov, Jelena Sjakste, Giorgia Fugallo, Lorenzo Paulatto, Michele Lazzeri, Francesco Mauri, and Nathalie Vast. “Nanoscale mechanisms for the reduction of heat transport in bismuth”. In: *Phys. Rev. B* 93 (6 Feb. 2016), p. 064301 (page 7).
- [78] J. M. Rowe, J. J. Rush, J. E. Schirber, and J. M. Mintz. “Isotope Effects in the PdH System: Lattice Dynamics of PdT<sub>0.7</sub>”. In: *Phys. Rev. Lett.* 57.23 (Dec. 1986), pp. 2955–2958 (page 8).
- [79] Roger A Cowley. “Anharmonic crystals”. In: *Reports on Progress in Physics* 31.1 (1968), p. 123 (pages 8, 9, 27).
- [80] S. Baroni and R. Resta. “Ab initio calculation of the low-frequency Raman cross section in silicon”. In: *Phys. Rev. B* 33 (8 Apr. 1986), pp. 5969–5971 (page 7).
- [81] A. C. Ferrari, J. C. Meyer, V. Scardaci, C. Casiraghi, M. Lazzeri, F. Mauri, S. Piscanec, D. Jiang, K. S. Novoselov, S. Roth, and A. K. Geim. “Raman Spectrum of Graphene and Graphene Layers”. In: *Phys. Rev. Lett.* 97 (18 Oct. 2006), p. 187401 (page 7).
- [82] Eugenio Calandrini, Lorenzo Paulatto, Daniele Antonangeli, Fei He, Ricardo P. S. M. Lobo, Francesco Capitani, Jean-Blaise Brubach, Pascale Roy, Laetitia Vincent, and Paola Giura. “Limits of the quasiharmonic approximation in MgO: Volume dependence of optical modes investigated by infrared reflectivity and ab initio calculations”. In: *Phys. Rev. B* 103 (5 Feb. 2021), p. 054302 (page 10).
- [83] O. Delaire, J. Ma, K. Marty, A. F. May, M. A. McGuire, M-H. Du, D. J. Singh, A. Podlesnyak, G. Ehlers, M. D. Lumsden, and B. C. Sales. “Giant anharmonic phonon scattering in PbTe”. In: *Nature Materials* 10.8 (June 2011), pp. 614–619 (page 10).
- [84] William Cochran, Roger Arthur Cowley, G. Dolling, and M. M. Elcombe. “The crystal dynamics of lead telluride”. In: *Proceedings of the Royal Society of London. Series A. Mathematical and Physical Sciences* 293.1435 (1966), pp. 433–451 (page 10).
- [85] Guilherme A. S. Ribeiro, Lorenzo Paulatto, Raffaello Bianco, Ion Errea, Francesco Mauri, and Matteo Calandra. “Strong anharmonicity in the phonon spectra of PbTe and SnTe from first principles”. In: *Phys. Rev. B* 97 (1 Jan. 2018), p. 014306 (page 10).
- [86] Etienne Balan, Lorenzo Paulatto, Qianyu Deng, Keevin Béneut, Maxime Guillaumet, and Benoit Baptiste. “Molecular overtones and two-phonon combination bands in the

- near-infrared spectra of talc, brucite, and lizardite”. In: *European Journal of Mineralogy (submitted)* (2022) (page 11).
- [87] Nicola Marzari, David Vanderbilt, and M. C. Payne. “Ensemble Density-Functional Theory for Ab Initio Molecular Dynamics of Metals and Finite-Temperature Insulators”. In: *Phys. Rev. Lett.* 79 (7 Aug. 1997), pp. 1337–1340 (page 11).
- [88] Jun-Hyung Cho and Matthias Scheffler. “Surface Relaxation and Ferromagnetism of Rh(001)”. In: *Phys. Rev. Lett.* 78 (7 Feb. 1997), pp. 1299–1302 (page 11).
- [89] Stefano Baroni, Paolo Giannozzi, and Eyvaz Isaev. “Density-functional perturbation theory for quasi-harmonic calculations”. In: *Reviews in Mineralogy and Geochemistry* 71.1 (2010), pp. 39–57 (page 11).
- [90] Christophe Bellin, Amit Pawbake, Lorenzo Paulatto, Keevin Béneut, Johan Biscaras, Chandrabhas Narayana, Alain Polian, Dattatray J. Late, and Abhay Shukla. “Functional Monochalcogenides: Raman Evidence Linking Properties, Structure, and Metavalent Bonding”. In: *Phys. Rev. Lett.* 125 (14 Sept. 2020), p. 145301 (pages 11, 12).
- [91] Amit Pawbake, Christophe Bellin, Lorenzo Paulatto, Keevin Béneut, Johan Biscaras, Chandrabhas Narayana, Dattatray J. Late, and Abhay Shukla. “Pressure-Induced Phase Transitions in Germanium Telluride: Raman Signatures of Anharmonicity and Oxidation”. In: *Phys. Rev. Lett.* 122 (14 Apr. 2019), p. 145701 (page 11).
- [92] Renata M. Wentzcovitch, José Luís Martins, and G. D. Price. “Ab initio molecular dynamics with variable cell shape: Application to MgSiO<sub>3</sub>”. In: *Phys. Rev. Lett.* 70 (25 June 1993), pp. 3947–3950 (page 13).
- [93] Chris J Pickard and R J Needs. “Ab initio random structure searching”. In: *Journal of Physics: Condensed Matter* 23.5 (Jan. 2011), p. 053201 (page 13).
- [94] Sebastiaan P. Huber, Spyros Zoupanos, Martin Uhrin, Leopold Talirz, Leonid Kahle, Rico Häuselmann, Dominik Gresch, Tiziano Müller, Aliaksandr V. Yakutovich, Casper W. Andersen, Francisco F. Ramirez, Carl S. Adorf, Fernando Gargiulo, Snehal Kumbhar, Elsa Passaro, Conrad Johnston, Andrius Merkys, Andrea Cepellotti, Nicolas Mounet, Nicola Marzari, Boris Kozinsky, and Giovanni Pizzi. “AiiDA 1.0, a scalable computational infrastructure for automated reproducible workflows and data provenance”. In: *Scientific Data* 7.1 (Sept. 2020) (page 13).
- [95] S. Poncé, E.R. Margine, C. Verdi, and F. Giustino. “EPW: Electron–phonon coupling, transport and superconducting properties using maximally localized Wannier functions”. In: *Computer Physics Communications* 209 (2016), pp. 116–133 (page 13).
- [96] Damien Querlioz, Jérôme Saint-Martin, Arnaud Bournel, and Philippe Dollfus. “Wigner Monte Carlo simulation of phonon-induced electron decoherence in semiconductor nanodevices”. In: *Phys. Rev. B* 78 (16 Oct. 2008), p. 165306 (page 13).
- [97] In: *Private Communication* (2022) (page 13).
- [98] Stefano Poli and Marco G. Pala. “Channel-Length Dependence of Low-Field Mobility in Silicon-Nanowire FETs”. In: *IEEE Electron Device Letters* 30.11 (2009), pp. 1212–1214 (page 13).
- [99] Nadjib Izitounene, Ngoc Duc Le, Brice Davier, Philippe Dollfus, Lorenzo Paulatto, and Jérôme Saint-Martin. “Spectral Simulation of Heat Transfer Across Polytype Interfaces”. In: *Crystal Research and Technology* 57.9 (2022), p. 2200017 (pages 13, 43).
- [100] J Sjakste, K Tanimura, G Barbarino, L Perfetti, and N Vast. “Hot electron relaxation dynamics in semiconductors: assessing the strength of the electron–phonon coupling from the theoretical and experimental viewpoints”. In: *Journal of Physics: Condensed Matter* 30.35 (Aug. 2018), p. 353001 (page 13).
- [101] Shobhana Narasimhan and David Vanderbilt. “Anharmonic self-energies of phonons in silicon”. In: *Phys. Rev. B* 43 (5 Feb. 1991), pp. 4541–4544 (page 16).

- [102] Alberto Debernardi, Stefano Baroni, and Elisa Molinari. “Anharmonic Phonon Lifetimes in Semiconductors from Density-Functional Perturbation Theory”. In: *Phys. Rev. Lett.* 75 (9 Aug. 1995), pp. 1819–1822 (pages 16, 55).
- [103] Michele Lazzeri and Stefano de Gironcoli. “First-principles study of the thermal expansion of Be(1010)”. In: *Phys. Rev. B* 65 (24 May 2002), p. 245402 (pages 16, 18, 54, 55).
- [104] QUANTUM ESPRESSO is an open source distribution available at. <http://www.quantum-espresso.org> (page 16).
- [105] Paolo Giannozzi et al. “QUANTUM ESPRESSO: a modular and open-source software project for quantum simulations of materials”. In: *Journal of Physics: Condensed Matter* 21.39 (2009), p. 395502 (pages 16, 17, 60).
- [106] Matteo Calandra, Michele Lazzeri, and Francesco Mauri. “Anharmonic and non-adiabatic effects in MgB<sub>2</sub>: Implications for the isotope effect and interpretation of Raman spectra”. In: *Physica C: Superconductivity* 456.1 (2007). Recent Advances in MgB<sub>2</sub> Research, pp. 38–44 (page 16).
- [107] Maxime Markov, Jelena Sjakste, Nathalie Vast, Romain Legrand, Bernard Perrin, and Lorenzo Paulatto. “Breakdown of Herring’s processes in cubic semiconductors for sub-terahertz longitudinal acoustic phonons”. In: *Phys. Rev. B* 98 (24 Dec. 2018), p. 245201 (pages 16, 29, 30, 63).
- [108] Michele Lazzeri, Matteo Calandra, and Francesco Mauri. “Anharmonic phonon frequency shift in MgB<sub>2</sub>”. In: *Phys. Rev. B* 68 (22 Dec. 2003), p. 220509 (page 17).
- [109] J Ziman. *Electrons and Phonons: the theory of transport phenomena in solids*. Oxford University Press, USA, 2001 (page 17).
- [110] G. P. Srivastava. In: *Pramana* 3 (1974) (page 17).
- [111] M. Asen-Palmer, K. Bartkowski, E. Gmelin, M. Cardona, A. P. Zhernov, A. V. Inyushkin, A. Taldenkov, V. I. Ozhogin, K. M. Itoh, and E. E. Haller. “Thermal conductivity of germanium crystals with different isotopic compositions”. In: *Phys. Rev. B* 56 (15 Oct. 1997), pp. 9431–9447 (page 17).
- [112] J. X. Cao, X. H. Yan, Y. Xiao, and J. W. Ding. “Thermal conductivity of zigzag single-walled carbon nanotubes: Role of the umklapp process”. In: *Phys. Rev. B* 69 (7 Feb. 2004), p. 073407 (page 17).
- [113] A Khitun and L Wang. In: *Applied Physics Letters* 79.6 (2001), pp. 851–853 (page 17).
- [114] A. Ward, D. A. Broido, Derek A. Stewart, and G. Deinzer. “*Ab initio* theory of the lattice thermal conductivity in diamond”. In: *Phys. Rev. B* 80 (12 Sept. 2009), p. 125203 (page 17).
- [115] Navaneetha K. Ravichandran and David Broido. “Unified first-principles theory of thermal properties of insulators”. In: *Phys. Rev. B* 98 (8 Aug. 2018), p. 085205 (page 17).
- [116] Stefano Baroni, Stefano de Gironcoli, Andrea Dal Corso, and Paolo Giannozzi. “Phonons and related crystal properties from density-functional perturbation theory”. In: *Rev. Mod. Phys.* 73 (2 July 2001), pp. 515–562 (pages 17, 54).
- [117] J. Maultzsch, S. Reich, C. Thomsen, H. Requardt, and P. Ordejón. “Phonon Dispersion in Graphite”. In: *Phys. Rev. Lett.* 92 (7 Feb. 2004), p. 075501 (page 18).
- [118] M. Mohr, J. Maultzsch, E. Dobard ži ć, S. Reich, I. Milo ševi ć, M. Damnjanovi ć, A. Bosak, M. Krisch, and C. Thomsen. “Phonon dispersion of graphite by inelastic x-ray scattering”. In: *Phys. Rev. B* 76 (3 July 2007), p. 035439 (page 18).
- [119] S. Piscanec, M. Lazzeri, Francesco Mauri, A. C. Ferrari, and J. Robertson. “Kohn Anomalies and Electron-Phonon Interactions in Graphite”. In: *Phys. Rev. Lett.* 93 (18 Oct. 2004), p. 185503 (page 18).
- [120] Michele Lazzeri, Claudio Attaccalite, Ludger Wirtz, and Francesco Mauri. “Impact of the electron-electron correlation on phonon dispersion: Failure of LDA and GGA DFT functionals in graphene and graphite”. In: *Phys. Rev. B* 78 (8 Aug. 2008), p. 081406 (pages 18, 19).

- [121] M. Methfessel and A. T. Paxton. “High-precision sampling for Brillouin-zone integration in metals”. In: *Phys. Rev. B* 40 (6 Aug. 1989), pp. 3616–3621 (pages 19, 53).
- [122] Pedro Venezuela, Michele Lazzeri, and Francesco Mauri. “Theory of double-resonant Raman spectra in graphene: Intensity and line shape of defect-induced and two-phonon bands”. In: *Phys. Rev. B* 84 (3 July 2011), p. 035433 (page 19).
- [123] Nicolas Mounet and Nicola Marzari. “First-principles determination of the structural, vibrational and thermodynamic properties of diamond, graphite, and derivatives”. In: *Phys. Rev. B* 71 (20 May 2005), p. 205214 (page 20).
- [124] M. Balkanski, R. F. Wallis, and E. Haro. “Anharmonic effects in light scattering due to optical phonons in silicon”. In: *Phys. Rev. B* 28 (4 Aug. 1983), pp. 1928–1934 (page 23).
- [125] Xing He, Dipanshu Bansal, Barry Winn, Songxue Chi, Lynn Boatner, and Olivier Delaire. “Anharmonic eigenvectors and acoustic phonon disappearance in quantum paraelectric SrTiO<sub>3</sub>”. In: *Physical review letters* 124.14 (2020), p. 145901 (page 27).
- [126] C. W. Li, O. Hellman, J. Ma, A. F. May, H. B. Cao, X. Chen, A. D. Christianson, G. Ehlers, D. J. Singh, B. C. Sales, and O. Delaire. “Phonon Self-Energy and Origin of Anomalous Neutron Scattering Spectra in SnTe and PbTe Thermoelectrics”. In: *Phys. Rev. Lett.* 112 (17 Apr. 2014), p. 175501 (page 27).
- [127] E Roger Cowley. “Generalized sum rules for the moments of a one-phonon spectral function”. In: *Journal of Physics: Condensed Matter* 9.8 (1997), p. 1719 (page 29).
- [128] C. Herring. “Role of low-energy phonons in thermal conduction”. In: *Phys. Rev.* 95 (1954), p. 954 (page 29).
- [129] H. Maris. *Physical Acoustics*. Ed. by W. P. Mason. Vol. 8. New York: Academic Press, 1971, pp. 279–345 (page 29).
- [130] R. Legrand. “Acoustique - étude et utilisation de nouvelles sources et transducteurs aux longueurs d’onde nanométriques”. PhD thesis. Université Pierre et Marie CURIE Paris VI (France), 2014 (page 29).
- [131] R. Legrand, A. Huynh, B. Jusserand, B. Perrin, and A. Lemaitre. “Direct measurement of coherent subterahertz acoustic phonons mean free path in GaAs”. In: *Phys. Rev. B* 93 (2016), p. 184304 (pages 29, 30).
- [132] G. Fugallo, M. Lazzeri, L. Paulatto, and F. Mauri. “*Ab initio* variational approach for evaluating lattice thermal conductivity”. In: *Phys. Rev. B* 88 (2013), p. 045430 (pages 29, 31).
- [133] Lorenzo Paulatto, Danièle Fournier, Massimiliano Marangolo, Mahmoud Eddrief, Paola Atkinson, and Matteo Calandra. “Thermal conductivity of Bi<sub>2</sub>Se<sub>3</sub> from bulk to thin films: Theory and experiment”. In: *Phys. Rev. B* 101 (20 May 2020), p. 205419 (pages 31, 35, 38).
- [134] Rudolf Sir. Peierls. *Quantum theory of solids*. Oxford University Press, 1955 (page 31).
- [135] H.B.G. Casimir. “Note on the conduction of heat in crystals”. In: *Physica* 5.6 (1938), pp. 495–500 (page 31).
- [136] R Berman, E. L. Foster, and J. S. Ziman. “Thermal conduction in artificial sapphire crystals at low temperatures I. Nearly perfect crystals”. In: *Proceedings of the Royal Society of London A: Mathematical, Physical and Engineering Sciences* 231.1184 (1955), pp. 130–144 (pages 31, 32).
- [137] A. Alkurdi, S. Pailhès, and S. Merabia. “Critical angle for interfacial phonon scattering: Results from ab initio lattice dynamics calculations”. In: *Applied Physics Letters* 111.9 (2017), p. 093101 (page 32).
- [138] Mahmoud Eddrief, Paola Atkinson, Victor Etgens, and Bernard Jusserand. “Low-temperature Raman fingerprints for few-quintuple layer topological insulator Bi<sub>2</sub>Se<sub>3</sub> films epitaxied on GaAs”. In: *Nanotechnology* 25.24 (2014), p. 245701 (page 33).

- [139] F.-T. Huang, M.-W. Chu, H. H. Kung, W. L. Lee, R. Sankar, S.-C. Liou, K. K. Wu, Y. K. Kuo, and F. C. Chou. “Nonstoichiometric doping and Bi antisite defect in single crystal  $\text{Bi}_2\text{Se}_3$ ”. In: *Phys. Rev. B* 86 (8 Aug. 2012), p. 081104 (pages 33, 35).
- [140] C Y Ho, R W Powell, and P E Liley. “Journal of Physical and Chemical Reference Data – Thermal Conductivity of the Elements: A Comprehensive Review”. In: vol. 3, sup. 1. American Chemical Society, 1974, pp. I–164 (pages 34, 35).
- [141] L. Lindsay, D. A. Broido, and Natalio Mingo. “Flexural phonons and thermal transport in multilayer graphene and graphite”. In: *Phys. Rev. B* 83 (23 June 2011), p. 235428 (page 34).
- [142] L. Lindsay, D. A. Broido, and Natalio Mingo. “Flexural phonons and thermal transport in graphene”. In: *Phys. Rev. B* 82 (11 Sept. 2010), p. 115427 (page 34).
- [143] J. Navrátil, J. Horák, T. Plecháček, S. Kamba, P. Lošt’ák, J.S. Dyck, W. Chen, and C. Uher. “Conduction band splitting and transport properties of  $\text{Bi}_2\text{Se}_3$ ”. In: *Journal of Solid State Chemistry* 177.4 (2004), pp. 1704–1712 (pages 35–37).
- [144] Olle Hellman and David A. Broido. “Phonon thermal transport in  $\text{Bi}_2\text{Te}_3$  from first principles”. In: *Phys. Rev. B* 90 (13 Oct. 2014), p. 134309 (pages 37, 38).
- [145] Max Born and DJ Hooton. “Statistische dynamik mehrfach periodischer systeme”. In: *Zeitschrift für Physik* 142.2 (1955), pp. 201–218 (page 39).
- [146] DJ Hooton. “The use of a model in anharmonic lattice dynamics”. In: *Philosophical Magazine* 3.25 (1958), pp. 49–54 (page 39).
- [147] N Boccara and G Sarma. “Theorie microscopique des transitions s’ accompagnant d’une modification de la structure cristalline”. In: *Physics Physique Fizika* 1.4 (1965), p. 219 (page 39).
- [148] Thomas R Koehler. “Theory of the self-consistent harmonic approximation with application to solid neon”. In: *Physical Review Letters* 17.2 (1966), p. 89 (page 39).
- [149] JE Turney, ES Landry, AJH McGaughey, and CH Amon. “Predicting phonon properties and thermal conductivity from anharmonic lattice dynamics calculations and molecular dynamics simulations”. In: *Physical Review B* 79.6 (2009), p. 064301 (page 39).
- [150] Petros Souvatzis, Olle Eriksson, MI Katsnelson, and SP Rudin. “Entropy driven stabilization of energetically unstable crystal structures explained from first principles theory”. In: *Physical review letters* 100.9 (2008), p. 095901 (page 40).
- [151] Fei Zhou, Weston Nielson, Yi Xia, Vidvuds Ozoliņš, et al. “Compressive sensing lattice dynamics. I. General formalism”. In: *Physical Review B* 100.18 (2019), p. 184308 (page 40).
- [152] Keivan Esfarjani and Yuan Liang. “Thermodynamics of anharmonic lattices from first principles”. In: *Nanoscale Energy Transport*. 2053-2563. IOP Publishing, 2020, 7-1 to 7–35 (page 40).
- [153] Bin Wei, Qiyang Sun, Chen Li, and Jiawang Hong. “Phonon anharmonicity: a pertinent review of recent progress and perspective”. In: *Science China Physics, Mechanics & Astronomy* 64.11 (2021), pp. 1–34 (page 40).
- [154] Jorge More, Burt Garbow, and Ken Hillstrom. *LMDIF*. 1980 (page 41).
- [155] Charles Bouillaguet. *Parallel LMDIF*. 2022 (page 41).
- [156] Félix Mouhat, Sandro Sorella, Rodolphe Vuilleumier, Antonino Marco Saitta, and Michele Casula. “Fully quantum description of the Zundel ion: combining variational quantum Monte Carlo with path integral Langevin dynamics”. In: *Journal of chemical theory and computation* 13.6 (2017), pp. 2400–2417 (page 42).
- [157] Giovanni Bussi, Davide Donadio, and Michele Parrinello. “Canonical sampling through velocity rescaling”. In: *The Journal of chemical physics* 126.1 (2007), p. 014101 (page 42).
- [158] WG Stirling. “Neutron inelastic scattering study of the lattice dynamics of strontium titanate: harmonic models”. In: *Journal of Physics C: Solid State Physics* 5.19 (1972), p. 2711 (page 42).

- [159] RA Cowley, WJL Buyers, and G Dolling. “Relationship of normal modes of vibration of strontium titanate and its antiferroelectric phase transition at 110 K”. In: *Solid State Communications* 7.1 (1969), pp. 181–184 (page 42).
- [160] Alessandro Barducci, Massimiliano Bonomi, and Michele Parrinello. “Metadynamics”. In: *WIREs Computational Molecular Science* 1.5 (2011), pp. 826–843 (page 43).
- [161] Yangyu Guo, Christophe Adessi, Manuel Cobian, and Samy Merabia. “Atomistic simulation of phonon heat transport across metallic vacuum nanogaps”. In: *Phys. Rev. B* 106 (8 Aug. 2022), p. 085403 (page 43).
- [162] Florian Knoop, Thomas A. R. Purcell, Matthias Scheffler, and Christian Carbogno. “Anharmonicity measure for materials”. In: *Phys. Rev. Materials* 4 (8 Aug. 2020), p. 083809 (page 43).
- [163] Richard M Martin. *Electronic Structure*. Cambridge University Press, 2004 (page 53).
- [164] Stefano de Gironcoli. “Lattice dynamics of metals from density-functional perturbation theory”. In: *Phys. Rev. B* 51 (10 Mar. 1995), pp. 6773–6776 (page 54).
- [165] Paul Peter Ewald. “Die Berchnung optischer und elektrostatischer Gitterpotentiale”. In: *Ann. Phys.* 64 (1921), pp. 253–287 (page 56).
- [166] Francesco Mauri Tobias Wassmann. *PhD Thesis - Graphene Nanoribbons: toward carbon-based electronics*. Paris: Université Pierre et Marie Curie, 2013 (page 56).
- [167] Leonard Kleinman and D. M. Bylander. “Efficacious Form for Model Pseudopotentials”. In: *Phys. Rev. Lett.* 48 (20 May 1982), pp. 1425–1428 (page 57).
- [168] *Anharmonic*. <http://anharmonic.github.io/>. 2013-2022 (page 61).
- [169] Raffaello Bianco, Ion Errea, Lorenzo Paulatto, Matteo Calandra, and Francesco Mauri. “Second-order structural phase transitions, free energy curvature, and temperature-dependent anharmonic phonons in the self-consistent harmonic approximation: Theory and stochastic implementation”. In: *Phys. Rev. B* 96 (1 July 2017), p. 014111 (page 64).